The Impact of Subtropical to Tropical Oceanic Interactions on Tropical Pacific Decadal Variability

Mathias Zeller

Supervisor: Dr. Shayne McGregor
Co-supervisor: Dr. Dietmar Dommenget

A thesis submitted for the degree of
Doctor of Philosophy
at Monash University in September 2019

School of Earth, Atmosphere and Environment
Faculty of Science
Melbourne, Australia

Copyright notice

Declaration of originality

I hereby declare that this thesis contains no material which has been accepted for the award of any other degree or diploma at any university or equivalent institution and that, to the best of my knowledge and belief, this thesis contains no material previously published or written by another person, except where due reference is made in the text of the thesis.

This thesis includes 1 original paper published in peer reviewed journals. The core theme of the thesis is the oceanic role in driving tropical Pacific decadal variability. The ideas, development and writing up of all the papers in the thesis were the principal responsibility of myself, the student, working within the School of Earth, Atmosphere and Environment under the supervision of Dr Shayne McGregor.

The inclusion of co-authors reflects the fact that the work came from active collaboration between researchers and acknowledges input into team-based research.

In the case of Chapter 2 my contribution to the work involved the following:

Thesis Chapter	Publication Title	Status *(published, in press, accepted or returned for revision)*	Nature and % of student contribution	Co-author name(s) Nature and % of Co-author's contribution*	Co-author(s), Monash student Y/N*
2	Hemispheric asymmetry of the Pacific shallow meridional overturning circulation	In press	Methodology, analysis, and writing. 80%	1) Shayne McGregor Methodology and writing. 15% 2) Paul Spence Methodology and writing. 5%	No No

I have not changed the content of the original published paper. However, the text has been reformated in order to generate a consistent presentation within the thesis.

Student signature: **Date:** 10 Sept 2019

The undersigned hereby certify that the above declaration correctly reflects the nature and extent of the student's and co-authors' contributions to this work.

Main Supervisor signature: **Date:** 10 Sept 2019

Acknowledgements

This research was funded by the Monash Graduate Scholarship (MGS), the Monash International Postgraduate Research Scholarship (MIPRS), and the Australian Research Council's Centre of Excellence for Climate System Science (ARCCSS).

I would like to express my great appreciation to my supervisor Dr Shayne McGregor for his patient guidance and his valuable and constructive critiques during my entire research project. I am particularly grateful for his willingness to give his time so generously for helpful discussions throughout my candidature. I would also like to thank my co-supervisor Dr Dietmar Dommenget for his contribution to the project.

Thank you to my PhD project panel, Prof Dr Michael Reeder, Assoc Prof Dr Julie Arblaster and Prof Dr Steven Siems, for the advice and assistance in keeping my progress on schedule.

I would like to offer my thanks to Dr Paul Spence from the University of New South Wales for his technical support in setting up and performing the model experiments needed in Chapter 2. Thanks also for hosting me during a short visit in which I got to know the ARCCSS partner institute in Sydney. On that note, I would also like to thank Prof Dr Johanna Baehr from the University of Hamburg and her research group for hosting me during a 2 months stay and providing feedback on the project.

The very helpful comments and advice for the accomplishment of Chapter 3 provided by Assoc Prof Dr Erik van Sebille from the University of Utrecht and Dr Anonietta Capotondi from the University of Colorado are greatly appreciated. A special thank you to Erik for helping me out to get the Lagrangian particle simulator working.

I wish to acknowledge the much needed help provided by the ARCCSS Computational Modelling Support (CMS) team. Thanks for your generous assistance with managing my big data and also for helping me solve all those technical issues I was facing during my candidature when working with the supercomputer Raijin, provided by the National Computational Infrastructure (NCI). I specifically would like to thank Dr Aidan Heerdegen and Dr Holger Wolff here. Sorry for not always keeping the quota and computing time limits.

Special thanks go out to my office mates Casey Blundell and Sam Thiele for their great companionship during the last three and a half years. Thanks for letting me peep into the research field of geology and for setting proper Australian examples.

My special thanks are extended to the entire School of Earth, Atmosphere and Environment (EAE) family who guaranteed a welcoming and friendly environment in which it was fun to work. I specifically would like to mention Christian Stassen, David Hoffmann, Dawn Yang, Cass Rodgers, Sarah Perry, Matthias Retsch, and Chen Li (thanks also for the electric piano), but there are many more that are not listed here. I also greatly appreciate our EAE postgrads/staff football crew with its coming and going members who allowed for a welcome weekly diversion from my sometimes tedious studies.

Finally, I wish to express my deep gratitude to my partner Sonja for being there for me in times of need and during the last couple of weeks for being the one who prepared delicious dinners even though being heavily involved in her own PhD project (sorry in this regard for my deficiency during that time, I will make up for this soon). My grateful thanks also go out to my family for their continued encouragement and enthusiasm about my research through the years even though we have been separated by 16.124 km.

Abstract

Understanding mechanisms of tropical Pacific decadal variability (TPDV) is of high importance for differentiating between natural climate variability and human induced climate change. The shallow meridional overturning circulation, namely the subtropical cells (STCs), in the Pacific Ocean are proposed to be involved in different mechanisms generating TPDV. In the first part of the thesis, we use a high-resolution ocean general circulation model to investigate the volume transports associated with the STC branches along 5°N and 5°S. We find three prominent differences between the Southern hemisphere (SH) STC and the Northern hemisphere (NH) STC: i) the NH STC varies 26% stronger than the SH STC; ii) the NH STC leads the SH STC by 3 months which causes the NH and SH STCs to play different roles during the course of El Niño and La Niña events; iii) in spite of the relative symmetry of the wind stress trends the STCs have differing decadal trends, with the SH STC clearly dominating the changes in the post-1993 period. To investigate the mechanisms driving the STC variability we identify winds that are linearly and non-linearly related to the El Niño - Southern Oscillation (ENSO) to force the ocean model. Explaining the hemispheric difference in interannual variance as well as the phase difference between the STCs, our results suggest ENSO to be an important factor in modulating its own background state, with a prominent role for the winds that are non-linearly related to ENSO. In the second part of the thesis, we investigate the meridional advection of spiciness (density compensated temperature) anomalies as a potential contributor to TPDV. Spiciness anomalies are advected with the STCs towards the tropics where they upwell and interact with the atmosphere. Utilising the same ocean model along with a Lagrangian tracer simulator we backtrack spiciness anomalies from the equatorial region and show that for a positive spiciness peak at the equator, ∼90% of the spiciness anomalies are sourced from the Southern hemisphere. In contrast to previous studies, our results suggest that the majority of these positive spiciness anomalies travel via the interior pathway as opposed to via the western boundary current (WBC). When following negative spiciness anomalies, the major contributor to the negative peak at the equator is the NH WBC (48%). In the third part of the thesis, we quantify the contribution of spiciness anomalies to the equatorial Pacific mixed layer heat budget. We distinguish between locally and remotely generated spiciness anomalies. For consistency, we again utilise the same ocean model and show that spiciness anomalies account for 30-60% of the vertical heat advection, with the influence increasing as the region gets confined closer to the equator. The major impact originates from locally generated spiciness anomalies. However, remotely generated spiciness anomalies make up 14-23% of the variance, with decreasing impact towards the western equatorial Pacific. Our results further suggest that the impact of remotely generated spiciness anomalies is considerably larger during La Niña phases as opposed to El Niño phases.

Contents

List of Figures

List of Tables

List of Acronyms

ARCCSS Australian Research Council Centre of Excellence for Climate System Science

CCA canonical correlation analysis

CEOF complex empirical orthogonal function

CMS Computational Modelling Support

CORE Coordinated Ocean-ice Reference Experiments

CP central Pacific

EAE Earth, Atmosphere and Environment

ECMWF European Centre for medium-range weather forecast

ENSO El Niño - Southern Oscillation

EOF empirical orthogonal function

EP Eastern Pacific

EUC equatorial undercurrent

IPO Interdecadal Pacific Oscillation

ITF Indonesian throughflow

MGS Monash Graduate Scholarship

MIPRS Monash International Postgraduate Research Scholarship

MLD mixed layer depth

NCAR National Center for Atmospheric Research

NCEP National Centers for Environmental Prediction

NCI	National Computational Infrastructure
NH	Northern hemisphere
NPO	North Pacific oscillation
OGCM	ocean general circulation model
PDO	Pacific Decadal Oscillation
SFC	surface
SH	Southern hemisphere
SLP	sea level pressure
SSH	sea surface height
SST	sea surface temperature
STC	subtropical cell
STD	standard deviation
SUB	subsurface
SV	Sverdrup
TC	tropical cell
TPDV	tropical Pacific decadal variability
TPI	tripolar index
T/S	temperature/salinity
WBC	Western boundary current
WES	wind-evaporation-SST
WWV	warm water volume

Chapter 1

Introduction

In the present time with unprecedented rates of climate change, intense debates are being held in all parts of society, be it in the public, in politics, or in science, about the impact of humans on the global climate. Overwhelmingly, the climate research community has concluded that human behaviour significantly affects the Earth's climate. However, it is also known that natural climate variability on long time scales ($>$10 years) superimposed on this long-term trend acts to blur the effect of the anthropogenic forcing. It is therefore essential to better understand decadal climate variability in order to disentangle the anthropogenic from the natural signal and provide more accurate estimates of future climate change.

Sea surface temperature (SST) is a key variable used to determine and predict decadal climate variations. SST represents the state of the slowly varying ocean and also marks the boundary between ocean and atmosphere, facilitating mutual feedbacks between them. Over the past two decades, research attention has increasingly been focusing on natural SST variability in the three major ocean basins, the Atlantic Ocean, the Indian Ocean, and the Pacific Ocean. Particular attention has been paid to the Pacific Ocean (Figure 1.1) as it covers 35% of the Earth's surface - more than the total land surface of all continents combined. Moreover, the Pacific Ocean houses the El Niño - Southern Oscillation (ENSO), the strongest mode of natural climate variability on interannual time scales, which establishes teleconnections around the globe. Thus, the Pacific SST is assumed to have an important impact on decadal climate variability. The following sections will look closer at decadal modes of variability in the Pacific basin, with a particular emphasis on the tropical Pacific which is the focus of this thesis.

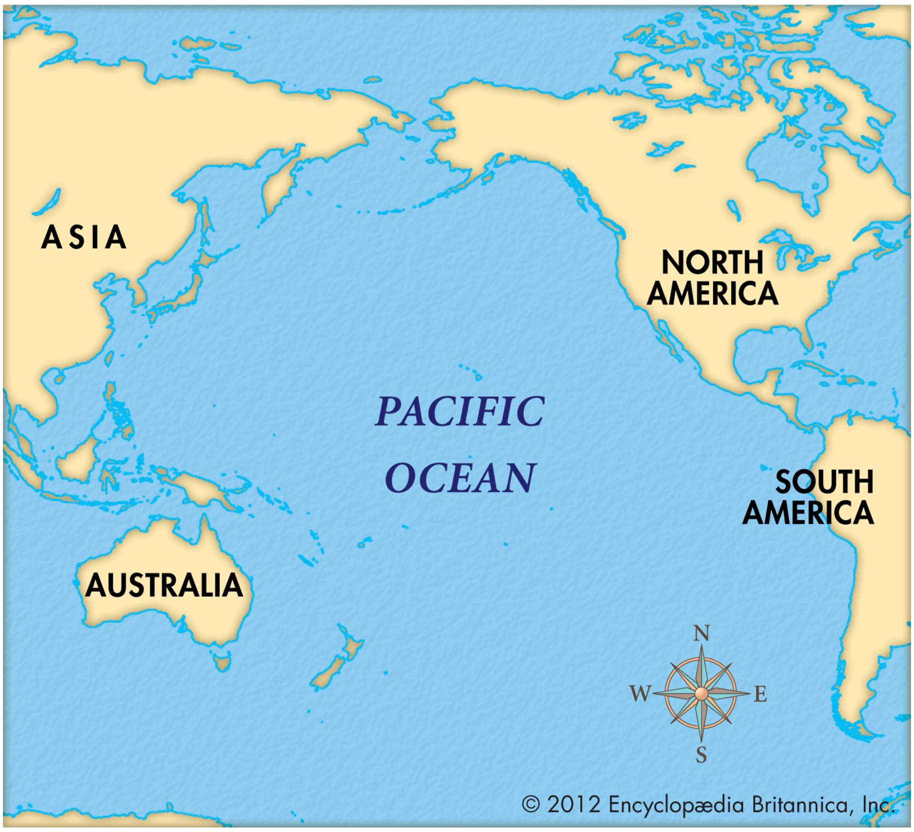

Figure 1.1: Pacific Ocean basin and adjacent continents (source: Encyclopaedia Britannica, Inc., 2012).

1.1 Pacific Decadal Oscillation

Throughout the second half of the last century, a long known imbalance in salmon production prevailed between the east coast and the west coast of the North Pacific Ocean. This imbalance seemed to reverse every one to two decades leading to economic prosperity or depression for the salmon fishers depending on their catchment area. Against this backdrop, Mantua et al. (1997) sought for possible connections between North Pacific climate variability and local ecosystems to investigate the causes for such shifts in salmon abundance.

Based on the analysis of empirical orthogonal functions (EOFs), Mantua et al. (1997) found a recurring pattern of sea surface temperature (SST) and sea level pressure (SLP) extending over a wide range of the Pacific basin (Figure 1.2a). They defined the leading EOF of monthly varying North Pacific (20°-70°N) SST anomalies (departures from the climatological annual cycle) as the Pacific Decadal Oscillation (PDO). Mantua et al. (1997) and the concurrent independent study by Minobe (1997) found a characteristic PDO recurrence interval of 50-70 years. Three phase changes have been reported by these two studies. A transition to the positive phase in 1925, followed by a transition to the negative phase in 1947 and another phase reversal in 1977. Two more phase changes have been reported after that, one around 1998 to the negative state and a recent one in 2015 back to the positive state. Regressing the global SST pattern on the PDO index results in the widely known PDO pattern with its strongest signal in the extratropical central North Pacific, a signal of opposite sign within the tropics and a weak Southern hemisphere signal of the same sign as the North Pacific signal (Figure 1.2).

Since its detection in 1997, the PDO has been the subject of a wide range of studies seeking to reveal the processes that drive the Pacific decadal changes. Suggested processes include stochastic atmospheric fluctuations in the Aleutian Low (Pierce 2001; Alexander 2010), teleconnections from the tropics via the "atmospheric bridge" (e.g., Zhang et al. 1997; Power et al. 1999; Alexander et al. 2002; Deser et al. 2004; Alexander 2010) and oceanic waves (e.g., Enfield and Allen 1980), mid latitude ocean dynamics and coupled variability, including the seasonal re-emergence of previously subducted temperature anomalies in the North Pacific (Alexander et al. 1999; Hanawa and Sugimoto 2004) as well as ocean gyre dynamics (e.g., Qiu 2003; Nakamura and Kazmin 2003).

In the scientific community, it is commonly agreed today that the PDO is not a sin-

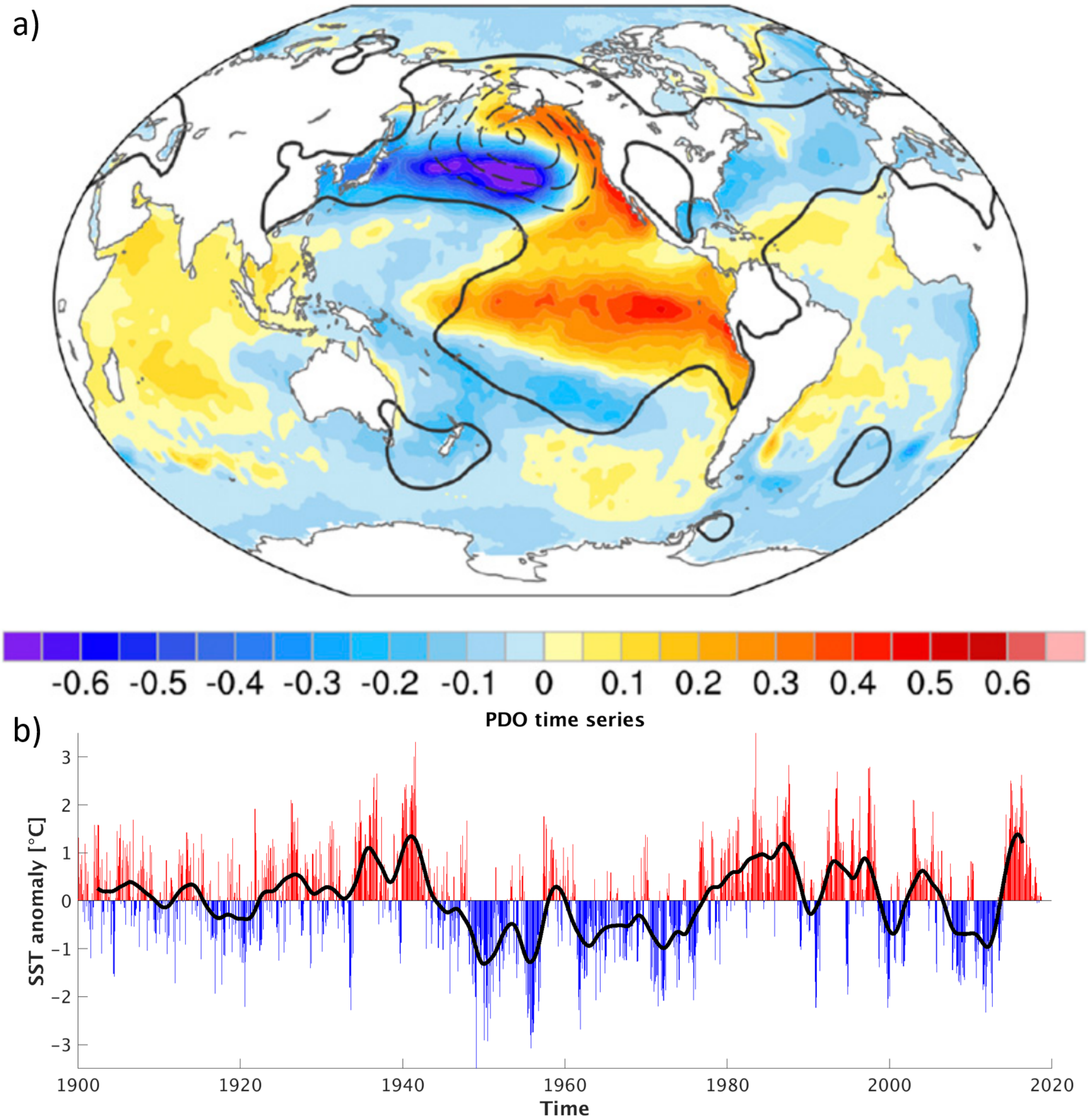

Figure 1.2: **a**) Regression of global monthly SST (shading; interval is 0.05 °C) and DJF SLP (contours; interval is 1 hPa) anomalies onto the PDO time series. Note that a positive PDO is associated with negative central North Pacific SST anomalies (source: Newman et al. 2016). **b**) PDO index derived as the leading PC of monthly SST anomalies in the North Pacific Ocean, poleward of 20°N. The monthly mean global average SST anomalies are removed to separate this pattern of variability from any "global warming" signal that may be present in the data. Positive (negative) values are drawn in red (blue). The thick black line shows the smoothed (5-yr low-pass filter) time series. The data is obtained from http://research.jisao.washington.edu/pdo/PDO.latest (01 Sep 2019). DJF: December/January/February

gle physical mode of its own but rather the result of the combined forcings outlined above (e.g., Schneider and Cornuelle 2005; Newman 2007; Alexander et al. 2008;

Newman 2013). An overview of the involved processes driving the PDO is given in Figure 1.3. A comprehensive review of the current state of knowledge of the PDO is provided by Newman et al. (2016).

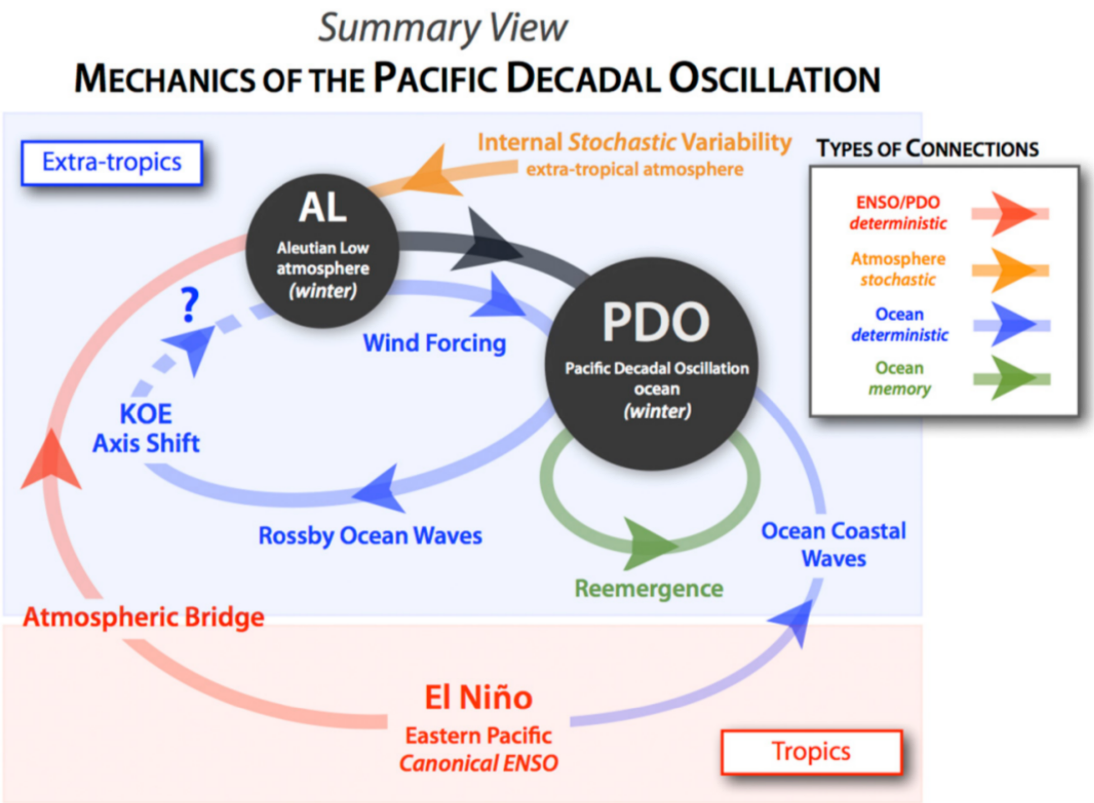

Figure 1.3: Summary figure of the basic processes involved in the PDO (source: Newman et al. 2016).

1.2 Interdecadal Pacific Oscillation

Only two years after the detection of the PDO, another mode of decadal climate variability in the Pacific Ocean was introduced by Power et al. (1999) when investigating the varying predictability of Australian rainfall. This mode is referred to as the interdecadal Pacific Oscillation (IPO) and it is commonly defined as the second EOF of low-pass filtered global SST (e.g., Power et al. 1999; Parker et al. 2007), while the first EOF represents the linear trend related to global warming. The

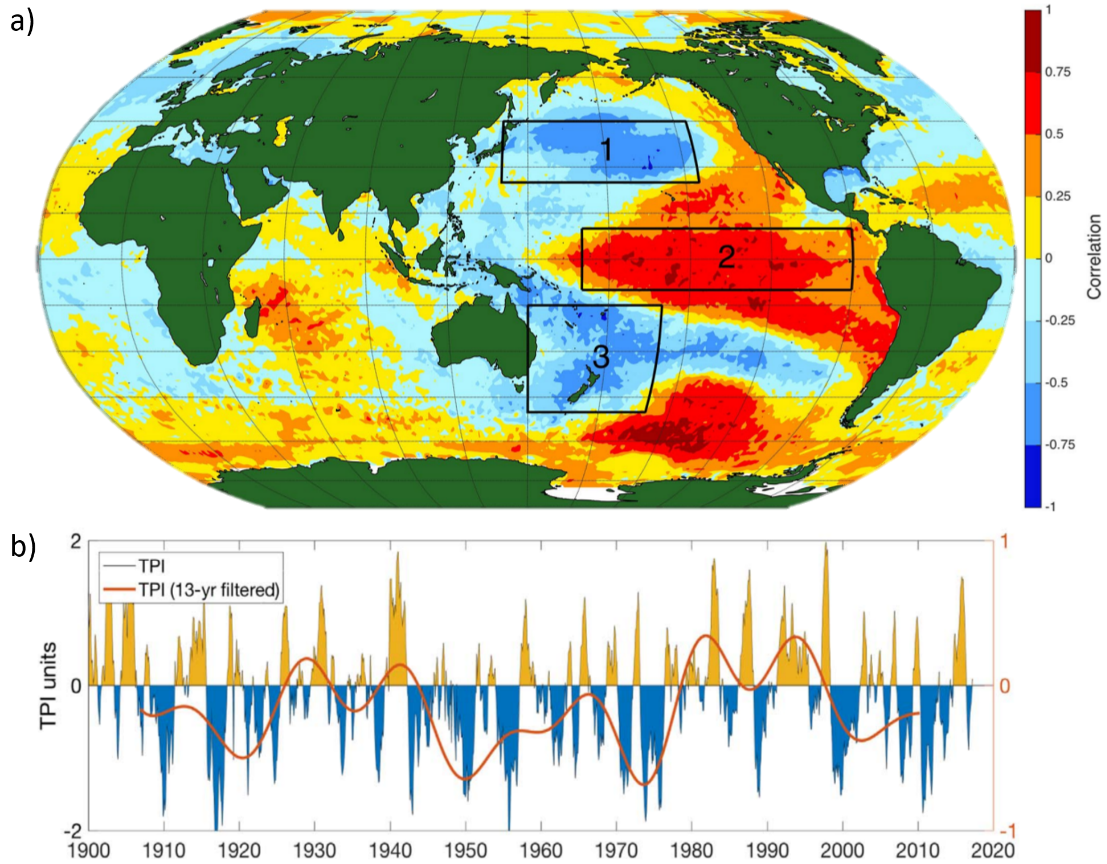

Figure 1.4: a) IPO pattern indicated as the correlation pattern between the IPO index and monthly global SST (source: Henley et al. 2015). **b**) IPO index derived from the tripolar index (TPI) as calculated by Henley et al. (2015). Positive (negative) values are drawn in orange (blue). The red line shows the smoothed (13-yr Chebyshev low-pass filter) time series (source: Henley 2017).

IPO describes basin-wide low frequency fluctuations of Pacific SST between warm and cold phases (Power et al. 1999; Folland et al. 2002; Parker et al. 2007; Henley et al. 2015; Henley 2017). The spatial pattern of the IPO has large similarities with the pattern of the interannual El Niño-Southern Oscillation, although the former is meridionally slightly broader (Figure 1.4). The decadal signal is therefore often referred to as decadal ENSO-like variability. Due to its spatial similarity to ENSO (Newman et al. 2016), the IPO can be thought of as a decadal manifestation of the interannual climate variability related to ENSO. The underlying mechanisms, however, are not known at this stage. In contrast to the PDO, the IPO signal is equally strong in the North and South Pacific (e.g., Henley et al. 2015). The difference between the IPO and the PDO arises from both the different methods in calculating each index by computing the EOF over different spatial extents as well as additional forcing of the PDO by internal processes in the North Pacific (Newman et al. 2016). The interest in a better understanding and predictability of the IPO lies in the enhanced predictability of associated climate phenomena like ENSO and the accompanying weather patterns around the globe (e.g., Alexander et al. 2002) that have severe socio-economic impacts.

1.3 Tropical Pacific Decadal Variability

A large scientific effort that has been put into the understanding of the Pacific decadal variability, both in terms of the PDO and IPO. The main focus of the studies dealing with Pacific decadal variability has been on the PDO and therefore on the extratropical North Pacific due to the proximity of the North American and European continents and the associated socio-economic interest. However, the tropical Pacific also exhibits a clear decadal signal, as shown in the PDO pattern (Figure 1.2) and the IPO pattern (Figure 1.4).

The tropical Pacific is climatically the most influential region on Earth (e.g., Alexander et al. 2002; Kosaka and Xie 2016). This is primarily due to its strong interannual variations (ENSO) and their numerous associated teleconnetions to the rest of the tropics (e.g., Latif and Barnett 1995; Chiang and Sobel 2002) and the entire globe (e.g., Horel and Wallace 1981; Grimm 2003; L'Heureux and Thompson 2006; Ineson and Scaife 2009; Deser et al. 2017). The tropical Pacific decadal variability (TPDV) sets the background state in which ENSO operates. Any changes in the tropical Pacific background state are proposed to lead to changes in ENSO frequency and intensity (e.g. Fedorov and Philander 2000; Collins et al. 2010; Stevenson et al. 2012; Zhao et al. 2016) and its teleconnetions (e.g., Power et al. 1999; Meehl and Teng 2007; Vecchi and Wittenberg 2010; Stevenson et al. 2012). Thus, changes in the decadal background state in the tropical Pacific can have an important effect on both the local and remote climate.

Another reason why a better understanding of TPDV is of great interest is to distinguish between natural climate variability and human induced climate change. Recent observations have shown that despite ongoing increases in atmospheric greenhouse gases, the Earth's global average surface air temperature remained more or less steady between 2001 and 2012 (Figure 1.5). Some studies, which sought to understand this discrepancy, indicated that a large portion of the recent hiatus in global surface warming at the beginning of the 21st century can be traced back to anomalously cool SSTs in the equatorial Pacific (e.g. Kosaka and Xie 2013). England et al. (2014) analysed the global mean surface air temperature of the past century and found a strong relationship with the phase of the IPO (Figure 1.5). Their study suggests that the cool SST anomalies responsible for the recent global warming hiatus are closely linked to a negative phase of the IPO. Consequently, natural climate variability may disguise the ongoing surface warming trend during some periods

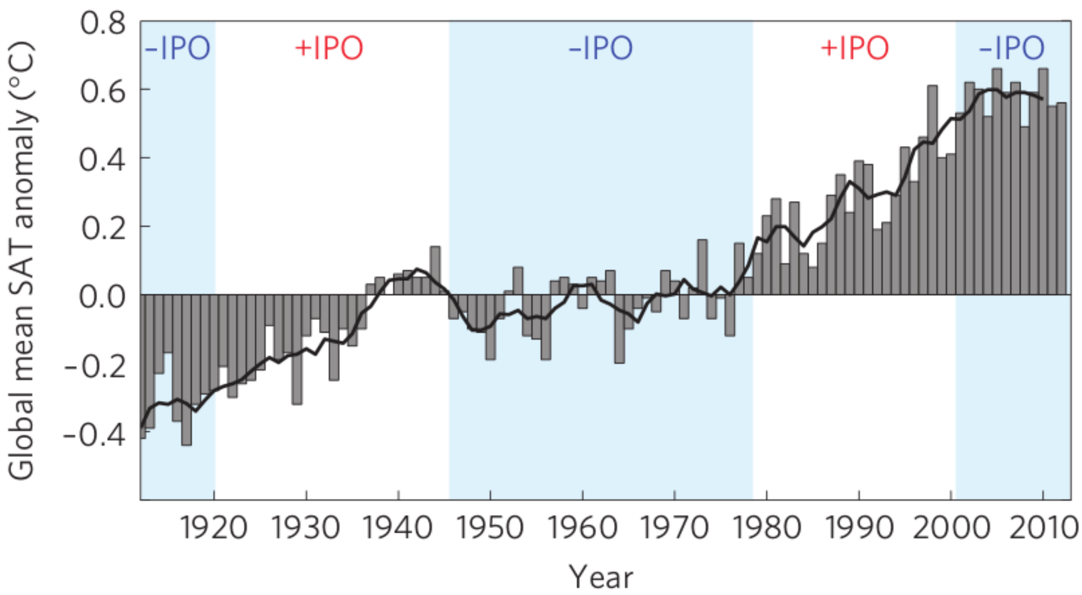

Figure 1.5: Global average surface air temperature anomalies over the past century. Temperature anomalies are shown as the annual mean relative to 1951–1980, with individual years shown as grey bars and a five-year running mean overlaid in bold. The sign of the low-pass filtered IPO index is indicated, with negative phases of the IPO shaded in blue (source: England et al. 2014).

while it may enhance the trend during other periods.

1.4 Potential drivers of TPDV

For decadal time scales, the observational record is relatively short and exhibits only a few phase changes. Accordingly, research is quite sporadic intermediately with renewed enthusiasm following every new phase change. This circumstance may help explain why despite the enormous impact of decadal changes in the tropical Pacific on global climate, the origin of TPDV remains unclear (Newman et al. 2016). Specifically, the relative contributions from coupled ocean-atmosphere processes acting on decadal time scales on the one hand, and an atmospheric noise driven residual of ENSO dynamics (Newman et al. 2011; Wittenberg et al. 2014) on the other hand, still have to be resolved. In the following sections, the individual processes in both the ocean and atmosphere that have been proposed to drive TPDV will be discussed in more detail.

1.4.1 Local drivers

The similarity between the SST patterns related to the interannual variability (ENSO) and the decadal variability (tropical expression of the IPO) in the tropical Pacific immediately suggests a relationship between the two modes of variability. In this sense, Vimont (2005) could reconstruct the spatial SST pattern of TPDV by linearly combining interannual SST patterns which they further related to the build-up, peak, and decay phases of ENSO (Figure 1.6). This suggests that to some degree TPDV can be considered the longer-term average of the ENSO cycle.

Rodgers et al. (2004) took a different approach to investigate the impact of the tropics on TPDV, which is based on the inherent nonlinearities of ENSO dynamics. These nonlinearities lead to a skewed distribution of equatorial SST anomalies whereby positive ENSO phases display higher amplitudes than negative ENSO

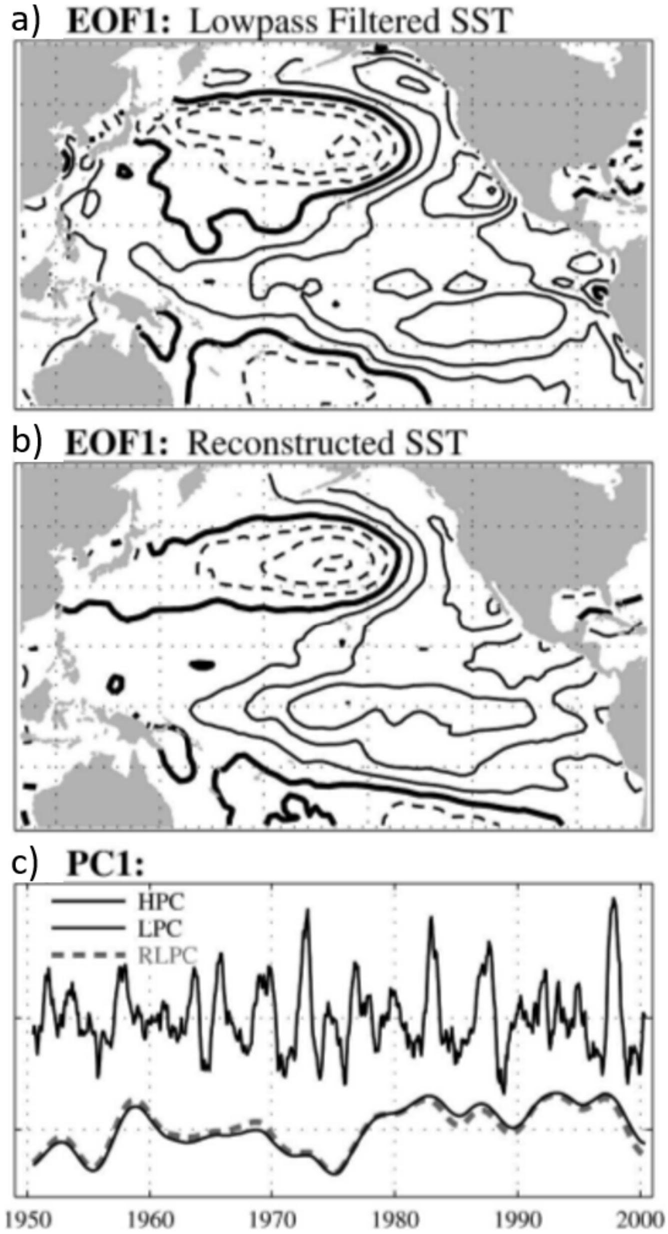

Figure 1.6: Leading EOF of **a**) low-pass filtered and **b**) reconstructed SST over the Pacific basin. **c**) The standardised PC time series for each of the spatial patterns in a) and b). For the spatial maps, solid contours denote positive anomalies, dashed contours denote negative anomalies, and the zero contour is thickened. The contour interval is 0.1°C std^{-1} (source: Vimont 2005).

phases. Using a 1,000-year integration of a coupled ocean-atmosphere model, Rodgers et al. (2004) showed that summing up El Niño and La Niña composites produces a residual signal in tropical SST anomalies (Figure 1.7). This residual signal comprises positive values in the east and negative values in the west. The authors further argue that during periods of enhanced ENSO activity the residual signal effectuates a change in the mean state.

There is a distinct difference between the two mentioned explanations. The explanation by Vimont (2005) is not dependent on nonlinearities of ENSO dynamics but is based on linear averages over periods with more El Niño events than La Niña events and vice versa. In contrast, the explanation by Rodgers et al. (2004) considers the differences in the SST patterns of both phases which becomes more dominant in periods of higher ENSO frequency and intensity. In reality, it is likely that both mechanisms play a role in explaining TPDV.

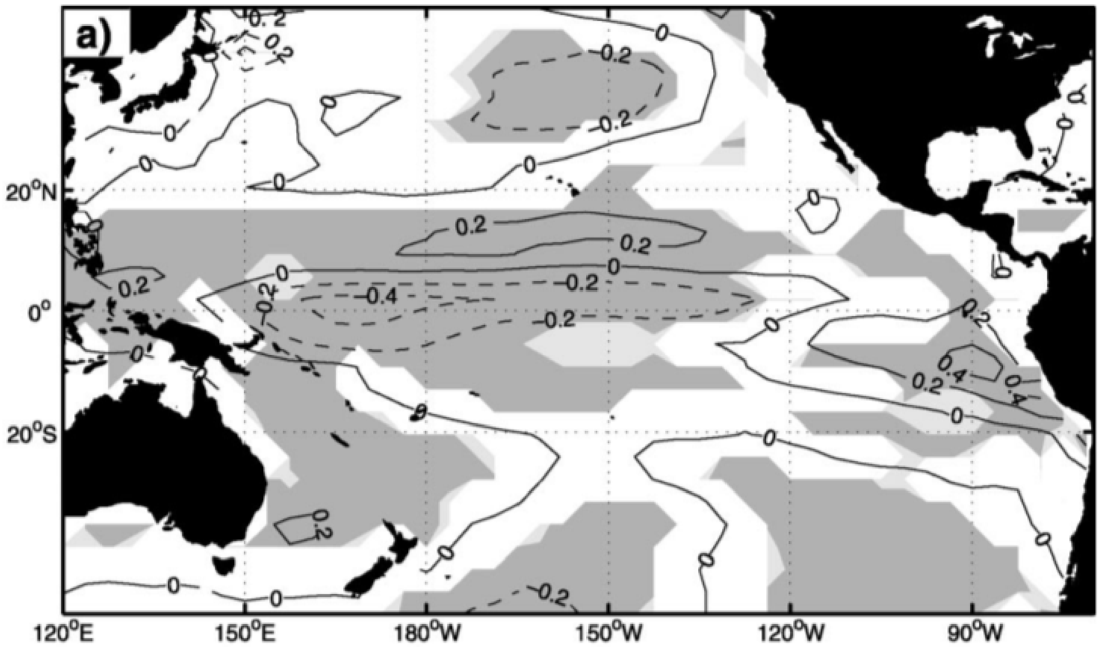

Figure 1.7: Asymmetry patterns in SST anomalies (°C). Significance levels of 90% and 95% are shown in gray (source: Rodgers et al. 2004).

1.4.2 Remote drivers

As opposed to the processes described in the previous section, TPDV can also be induced from remote regions, which is defined here as everywhere outside the tropical

Pacific. This involves genuine decadal signals in a distinct region of the world which propagate into the tropical Pacific. The transfer of the signal to the tropical Pacific occurs either via the atmosphere or via the ocean. The following sections will describe the mechanisms proposed to date in each of the two mediums that contribute to TPDV.

1.4.2.1 Atmospheric drivers

In the atmosphere, decadal signals are transported to the tropical Pacific either via interbasin teleconnections from the Atlantic or Indian Oceans, or through interactions between the subtropics and the tropics within the Pacific basin. We will first look at trans-basin teleconnections here, before considering Pacific basin subtropical to tropical interactions.

Interbasin teleconnections

Using a coupled ocean-atmosphere general circulation model, Chikamoto et al. (2012) simulated the observed strengthening of the Walker circulation in the 1990s. They could show that the simulations performed better when the ocean, including the Atlantic and Indian Oceans, is initialised with temperature and salinity anomalies than when the model is only externally forced. This suggests that the Atlantic and Indian Oceans potentially do have an impact on the Pacific climate.

In a further study, McGregor et al. (2014b) used an atmospheric general circulation model coupled to a slab ocean climatological mixed layer with partially prescribed SST trends in different regions. The authors found that the recent (1992-2012) intensification of the Walker circulation and the associated cooling in the eastern equatorial Pacific, were partly driven by a warming trend of Atlantic sea surface temperature. This Atlantic warming trend led to impacts in the Pacific as it caused a displacement of the atmospheric pressure centres and the related wind systems. As can be seen in Figure 1.8, the observed trend patterns for SST, SLP, precipitation and wind stress (Figure 1.8a and b), are all well simulated when only prescribing the Atlantic SST trend (Figure 1.8e and f) and this simulation explains much of the trends compared to the simulation with a globally prescribed SST trend (Figure 1.8c and d). Chikamoto et al. (2016) come to the same conclusion by assimilating observed three-dimensional Atlantic temperature and salinity anomalies into a coupled general circulation model. Similar results were also found by Ruprich-Robert et al. (2017).

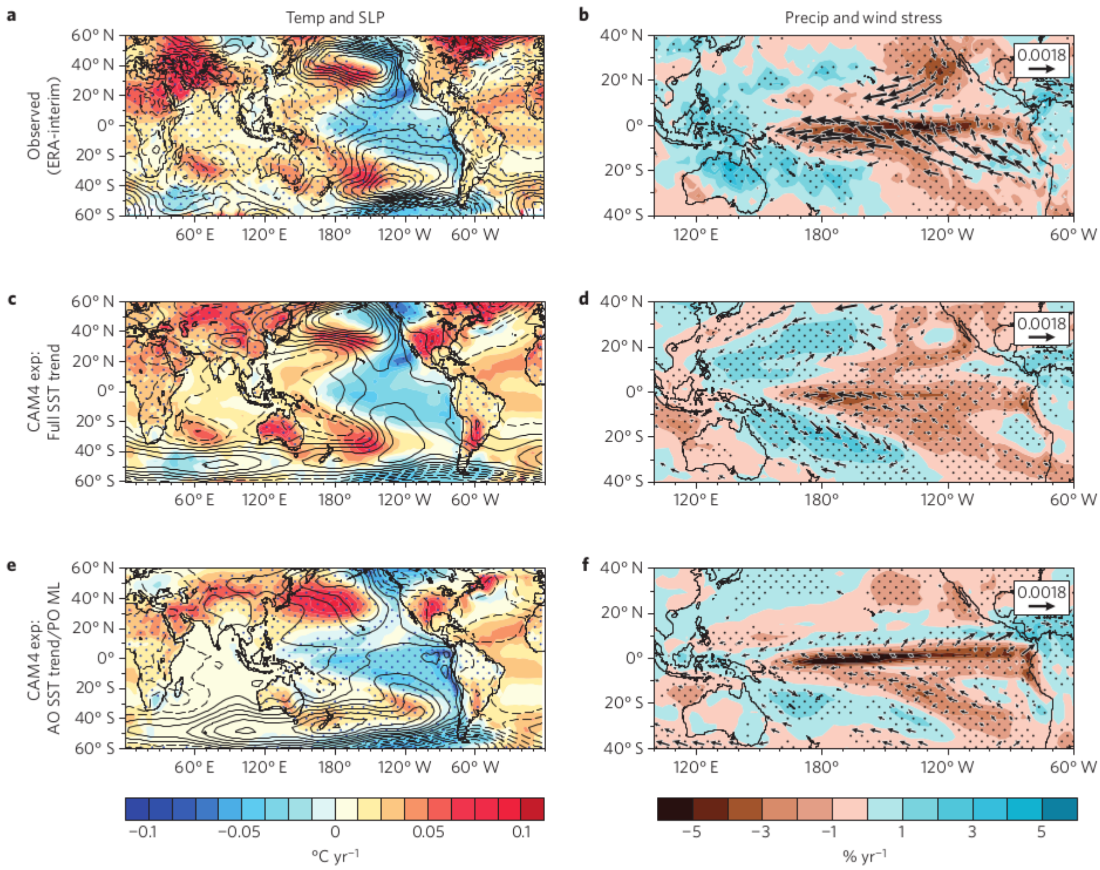

Figure 1.8: Trends (1992–2011) of SST, SLP, wind stress and relative precipitation. **a**) Observed surface temperature (shading; °C yr^{-1}) and SLP (contours; Pa yr^{-1}). SLP trend contours range from 14 Pa to 14 Pa with a contour increment of 4 Pa. Negative contours are dashed. **b**) Observed relative precipitation trends (shading; % yr^{-1}) and significant wind stress trends (vectors; N m^{-2} yr^{-1}) significant above the 95% level. In all panels stippling indicates that the changes in the underlying shaded plots are significant above the 95% level. **c**) and **d**) as in a) and b), but for the CAM4 experiment forced with the global observed SST trend (shading). **e**) and **f**) as in a) and b), but for the CAM4 experiment forced with the Atlantic SST trend and a Pacific mixed layer. (source: McGregor et al. 2014). CAM4: Community Atmospheric Model version 4

Extratropical to tropical interactions

In terms of meridional interactions connecting the mid-latitudes to the tropics within the Pacific basin, the focus of research in the early stages was on atmospheric processes (Barnett et al. 1999). In the atmosphere, the Hadley cells connect the subtropics to the tropics in each hemisphere and they constitute the primary atmospheric mechanism of transferring climate signals from the subtropics to the equator. The idea is that low-frequency changes in North Pacific winds extend as far south as into the tropics where they change the zonal wind stress which in turn feeds back with the ocean thermocline effecting a change in the equatorial mean state. In their study, (Barnett et al. 1999) applied a canonical correlation analysis (CCA) between Pacific SST and wind stress, to show that decadal changes in North Pacific SST not only induce wind stress changes in the North Pacific but also in the central and Western equatorial Pacific. This relationship was not only apparent in observations and a fully coupled model but also in an atmospheric model coupled to a slab ocean. Because of the missing ocean circulation in the slab ocean, the authors could exclude a coupling from the tropics to the mid-latitudes due to ENSO. A dominant role of the atmosphere was also found by Pierce et al. (2000) who investigated a 137-year long coupled AOGCM run. The authors suggest that mid-latitude SST anomalies drive changes in the trade winds which in turn modulate the slope of the equatorial thermocline, thereby affecting tropical Pacific climate.

A new null hypothesis for Pacific decadal climate variability has been put forward by Di Lorenzo et al. (2015) (Figure 1.9). This null hypothesis suggests that high frequency stochastic atmospheric forcing in the extratropics excites winds and anomalous SST which propagate towards the tropics via the wind-evaporation-SST (WES) feedback (Xie 1999). This set of processes is referred to as meridional modes and it acts as a red-noise process. This way, the meridional modes induce low frequency decadal variability in the tropics. The decadal signal is then enhanced by positive feedbacks related to ENSO dynamics within the tropics (zonal modes) and projected back to the extratropics via atmospheric teleconnections.

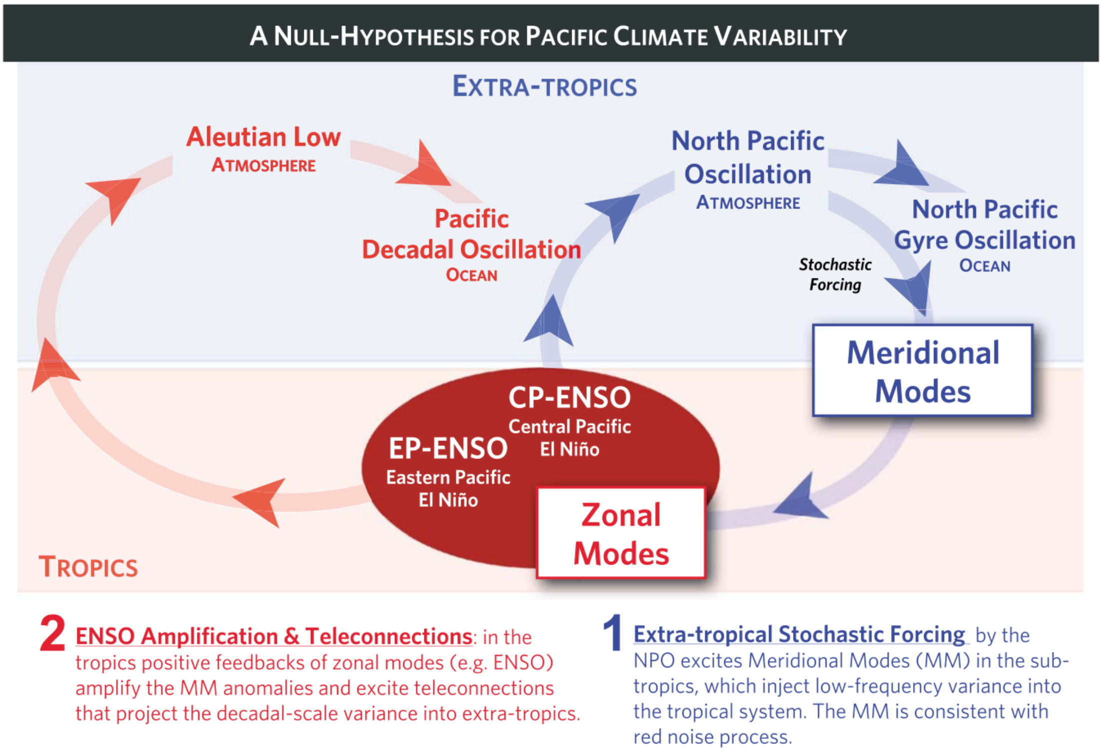

Figure 1.9: Diagram of the null hypothesis for Pacific climate variability. In this red noise model the stochastic variability of the North Pacific Oscillation (NPO) acts as the forcing, while the evolution of the ocean-atmosphere coupled system from extratropics to tropics and back to extratropics (1–2 years) provides the damping timescale. This progression and timescale provide the key memory for integrating the stochastic forcing of the atmosphere (e.g., NPO) into decadal-scale variance over the entire Pacific basin (source: Di Lorenzo et al. 2015). NPO: North Pacific oscillation

1.4.2.2 Oceanic drivers

While all of the above mentioned atmospheric processes have been shown to operate the relative importance for each of these is still unknown. Aside from the atmosphere, the ocean can also act as a means for transporting decadal signals between latitude bands. Being the focus of this work, the ocean's role as a driver of TPDV will be examined in greater detail in the remainder of the thesis. In this section, the focus will be on the proposed role of the ocean in carrying remotely generated low-frequency signals from the subtropics to the tropics.

Similar to the Hadley cells in the atmosphere, oceanic cells exist that connect the

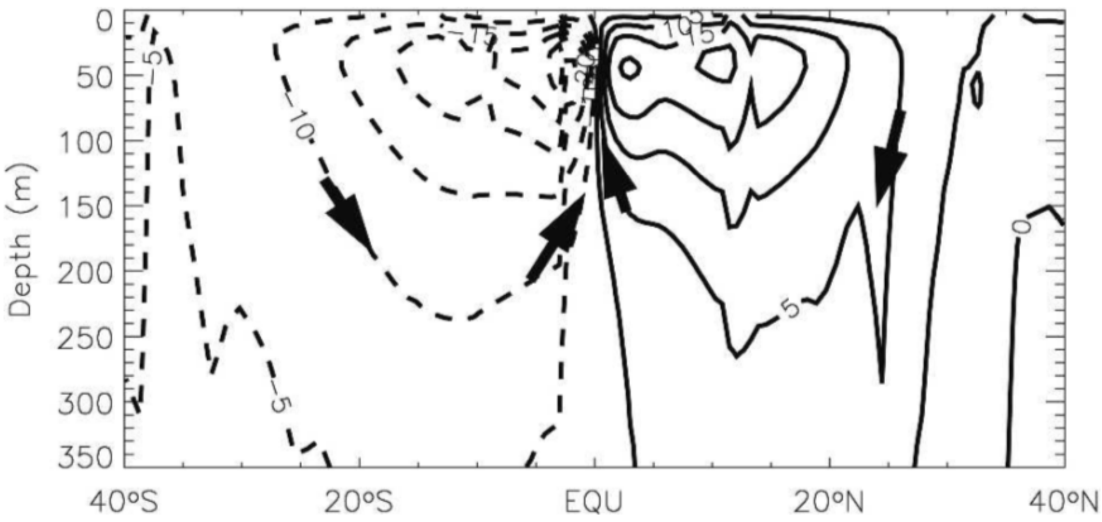

Figure 1.10: Meridional streamfunction computed from the NCAR OGCM. Contour interval is 5 Sv. Thick arrows indicate the direction of the zonally averaged circulation (source: Capotondi et al. 2005). NCAR: National Center for Atmospheric Research; OGCM: ocean general circulation model

subtropics with the tropics. These cells are commonly known as the subtropical cells (STCs). The STCs have been first defined and analytically described by McCreary Jr and Lu (1994) and they since have been the subject of numerous further studies (e.g., Liu et al. 1994; Lee and Fukumori 2003; Schott et al. 2004; Capotondi et al. 2005; Izumo 2005; Cheng et al. 2007; Lübbecke et al. 2008; Chen et al. 2015a). In the mean, the STC in each hemisphere extends vertically to about 200-300 m depth and meridionally to about 20° latitude. Each STC is comprised of four different branches (Figure 1.10): 1) subduction in the subtropical Pacific, 2) an equatorward flow along the mean pycnocline, 3) equatorial upwelling, and 4) a return flow at the surface back to the subtropics.

Typically, the equatorward subsurface transport of the subducted water occurs via two distinct pathways, namely the ocean interior and the low latitude western boundary current (WBC) (Johnson and McPhaden 1999; Izumo et al. 2002). The surface return flow of the upwelled water, which largely occurs in the ocean interior, is confined to the shallow Ekman layer in the top 50 m (Johnson 2001).

The STCs are often associated with the decadal variability of the tropical Pacific (e.g., Johnson and McPhaden 1999; Capotondi et al. 2005; Hong et al. 2014) as the extratropical North Pacific exhibits the strongest decadal signals in the Pacific basin (cf. Section 1.1). Thus, the STCs are viewed as a connective element that propagates the decadal variance from the subtropics to the tropics. Three distinct mechanisms have been proposed as to how the STCs can contribute to TPDV, which we will elucidate in more detail in the following.

Mean Advection of Anomalous Temperature (the $\overline{v}T'$ mechanism)

Following the prolonged persistence of anomalously warm tropical Pacific temperatures during the early 1990s, the first mechanism involving the STCs as a driver of TPDV was proposed by Gu and Philander (1997). In their study, the authors use a simple oceanic box model comprising a tropical and an extratropical box to demonstrate the possibility of temperature anomalies generated in the extratropics being advected with the mean circulation to the tropics. The temperature anomaly is subsequently upwelled and amplified by positive feedbacks with the overlying tropical atmosphere. At the same time, the warming (cooling) tropical ocean gives rise to a strengthening (weakening) extratropical westerlies that act to cool (warm) temperatures of the subjacent surface water due to anomalously strong (weak) evaporative cooling. The subduction and equatorward advection of these new temperature anomalies eventually leads to a phase change of the tropical conditions. As this mechanism is based on the mean meridional advection of anomalous temperature it is referred to as the $\overline{v}T'$ mechanism where the overline ($^{-}$) denotes the climatological mean and the prime ($'$) denotes anomalies to this mean.

Observations indeed confirm the subduction of thermal anomalies in the subtropical North Pacific (Schneider et al. 1999a). However, a further study of the same year argues that subducted temperature anomalies decay prior to reaching the tropics, leaving tropical decadal temperature anomalies to be largely driven by anomalies in local Ekman pumping (Schneider et al. 1999b). In line with Schneider et al. (1999b), but using observations and a primitive equation ocean model, Hazeleger et al. (2001b) conclude that North Pacific temperature anomalies can propagate

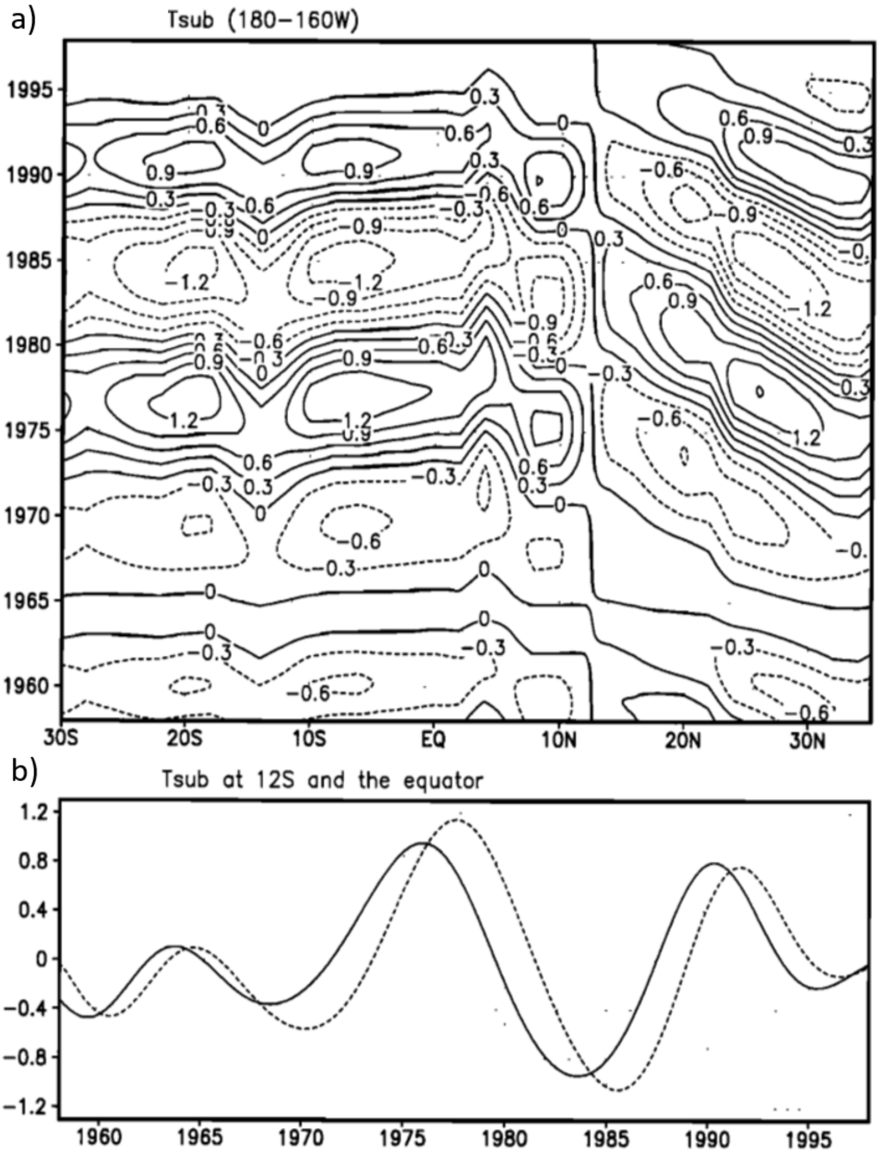

Figure 1.11: a) Decadal subsurface temperature variations averaged between 180-160°W from the first joint CEOF mode applied to subsurface temperature and SLP. **b**) As in Figure 1.11a, but for the subsurface temperature averaged between 14-10°S (solid line) and between 4°S-4°N (dashed line) (source: Luo and Yamagata 2001). CEOF: Complex Empirical Orthogonal Function

into the tropics but they do not arrive at the equator. Yet, both studies which refute the $\overline{v}T'$ mechanism only apply to the Northern hemisphere, which still leaves the meridional advection of temperature anomalies in the Southern hemisphere as a possible driver of TPDV. In fact, Luo and Yamagata (2001) report the advection of temperature anomalies from the Southern hemisphere extratropics to the tropics with a coherent subsurface temperature pattern that extends from 30°S to 5°N (Figure 1.11a). In their study, the Southern hemisphere subsurface temperature is highly correlated to the equatorial subsurface temperature when leading by 1-2 years (Figure 1.11b). It is also very obvious that Northern hemisphere subsurface temperatures do not arrive at the equator (Figure 1.11a). Giese et al. (2002) confirm the propagation of temperatures anomalies in the Southern hemisphere using an ocean general circulation model.

Anomalous Advection of Mean Temperature (the $v'\overline{T}$ mechanism)

A different STC based mechanism revolves around variations in the STC overturning rate. This mechanism suggests that an increase (decrease) in the rate of the STC acts to transport and upwell more (less) cold extratropical water into the tropics which eventually imprints on the surface temperature. As this mechanism represents the anomalous advection of mean temperatures, it is referred to as the $v'\overline{T}$ mechanism.

Using a coupled model with a $3\frac{1}{2}$-layer ocean component and a statistical atmosphere, Kleeman et al. (1999) were the firsts to propose that transport variations in the Northern hemisphere STC alter the eastern tropical Pacific cold tongue and thus modify tropical Pacific climate. Their findings were supported by Klinger et al. (2002) who perturbed the same intermediate ocean model with a prescribed wind stress anomaly and thus modified the equatorial upwelling branch as part of the STCs. Again using the same ocean model but a slightly more complicated atmosphere, Solomon et al. (2003) showed an oceanic coupling from the North Pacific extratropics to the equator via variations in STC transport.

Analysing the output of a comprehensive ocean general circulation model forced by observed wind stress, Nonaka et al. (2002) found that the decadal variability in the tropical Pacific is forced roughly equally by local equatorial winds and by off-equatorial winds. They further showed that the remotely driven part of the decadal variability is strongly related to the strength of the STCs in both hemispheres, in support of the $v'\overline{T}$ mechanism. In addition, McPhaden and Zhang (2004) calculated the subsurface geostrophic transport from hydrographic data and found that the long-term trends in transport convergence across 9°N and 9°S are anti-correlated with the trends in equatorial Pacific SST anomaly (Figure 1.12). While the exact importance of this mechanism is unknown, all of the studies mentioned in this section agree that this mechanism is valid in driving TPDV.

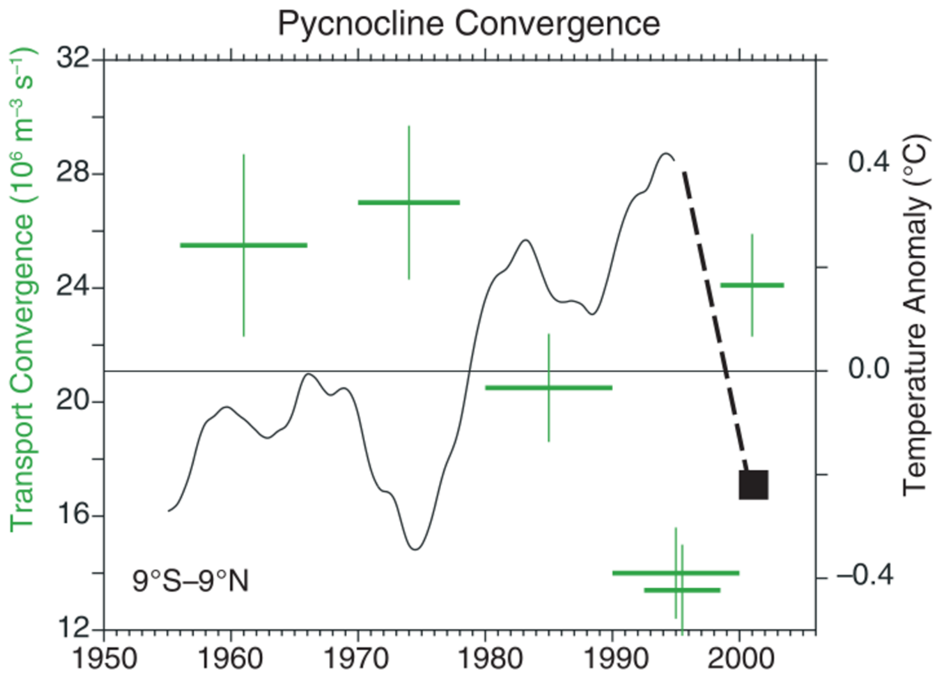

Figure 1.12: Meridional volume transport convergence in the pycnocline across 9°N and 9°S and equatorial sea surface temperature anomalies for 1950-2003. The period 1950-1999 is reproduced from McPhaden and Zhang (2002) with values for July 1998-June 2003 and July 1992-June 1998 superimposed. Also plotted are areally averaged sea surface temperature anomalies in the eastern and central equatorial Pacific (9°N-9°S, 90°W-180°W) encompassing the region where equatorial upwelling is most prevalent. The temperature time series from 1950-1999 is derived from monthly analyses of Reynolds et al. (2002) smoothed twice with a 5-year running mean to filter out the seasonal cycle and year-to-year oscillations associated with ENSO. The single 5-year average for July 1998 to June 2003 is connected to the smoothed time series with a dashed line. Anomalies are relative to 1950-1999 averages (source: McPhaden and Zhang 2004).

The Spiciness Mechanism

In the ocean, the vertical hydrographic structure can be perturbed in two different ways as depicted by Munk (1981). In the case of an internal wave passing through a stably stratified water column, surfaces of constant temperature (isotherms) and surfaces of constant salinity (isohalines) are deflected in the same direction such that the corresponding surfaces of constant density (isopycnals) are also deflected in that direction (Figure 1.13, left panel). Consequently, the vertical density profile is affected in this case. The change in density can also be perceived in a temperature/salinity (T/S) diagram (Figure 1.14, left panel). Here, the water parcels at the original vertical positions become colder and saltier and, hence, denser.

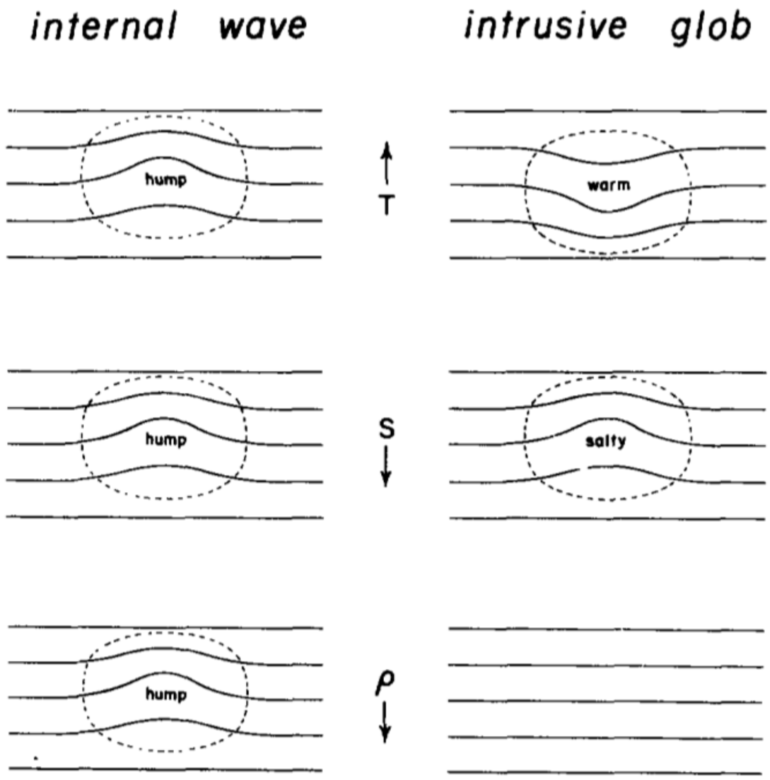

Figure 1.13: Contours of potential temperature, salinity and potential density in a vertical section (x,z) for an internal wave hump and a compensated warm and salty intrusive glob (source: Munk 1981).

On the other hand, in the case of an intrusion, the deflection of isotherms and isohalines can be such that their effect on density cancels (Figure 1.13, right panel).

In the corresponding T/S diagram, the water parcels at the original vertical positions become warmer and saltier while still remaining on the same density surface (Figure 1.14, middle panel). Hence, the vertical density profile is not affected in this case. On a surface of constant density, the warmer and saltier the water is the spicier it is. Thus, in a T/S diagram spiciness is represented by lines orthogonal to isopycnals (Figure 1.14, right panel). A measure of spiciness is temperature or salinity on isopycnals. However, for most applications, as is the case here, the interest is in temperature because this is the variable that interacts with the atmosphere and can lead to feedbacks that amplify the original temperature anomaly.

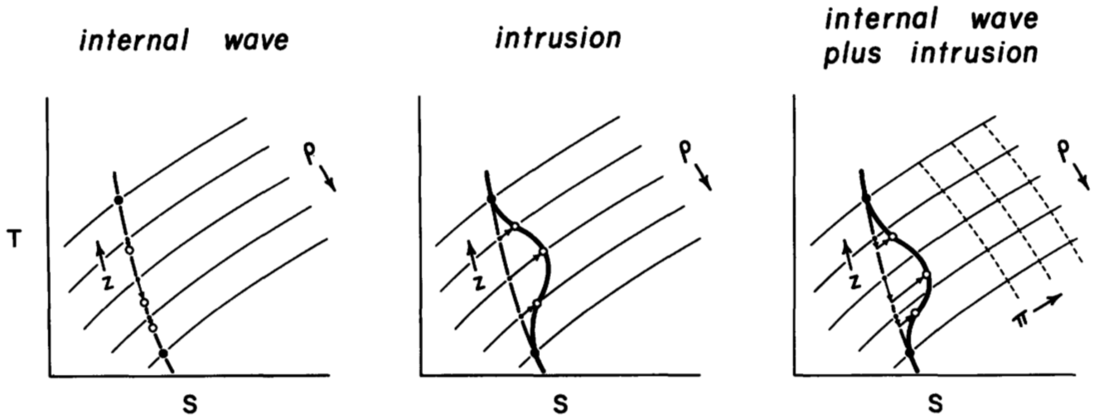

Figure 1.14: T-S diagrams for an internal wave hump and a compensated intrusive glob. The dots (●) correspond to the undisturbed positions of the five contours in Figure 1.13. The open circles (○) give the positions through the center of the disturbance. The "isospiceness" lines (constant π) are orthogonal to the isopycnals (constant ρ) (source: Munk 1981).

Spiciness anomalies, i.e. deviations of spiciness with respect to the climatology, are fundamentally different from other thermal anomalies, such as the ones created at the surface and subducted into the thermocline (e.g. Gu and Philander 1997; Schneider et al. 1999a). The density-compensating nature of spiciness anomalies allows them to behave like passive tracers that are not affected by dissipation as strongly as other thermal anomalies. For this reason, spiciness anomalies have been proposed as a third mechanism to drive tropical Pacific decadal variability (Schneider 2000). According to this idea, anomalously strong trade winds accelerate the North Equatorial current and Countercurrent which produces cold/fresh spiciness anomalies in the subtropics of the North and South Pacific through anomalous advection across mean spiciness gradients. These spiciness anomalies are advected with the mean STC circulation to the equator. Once at the equator, the spiciness anomalies are upwelled where they alter SST and cause a relaxation of the trade winds. This change in the trade winds leads to a weakening of the North Equatorial current and Countercurrent which results in the generation of warm/salty subtropical spiciness anomalies. These spiciness anomalies are advected to the equator and reverse the phase (Figure 1.15). Based on the average travel time of 5 years from the subtropics to the equator the entire cycle is suggested to have a period of 10 years (Figure 1.16).

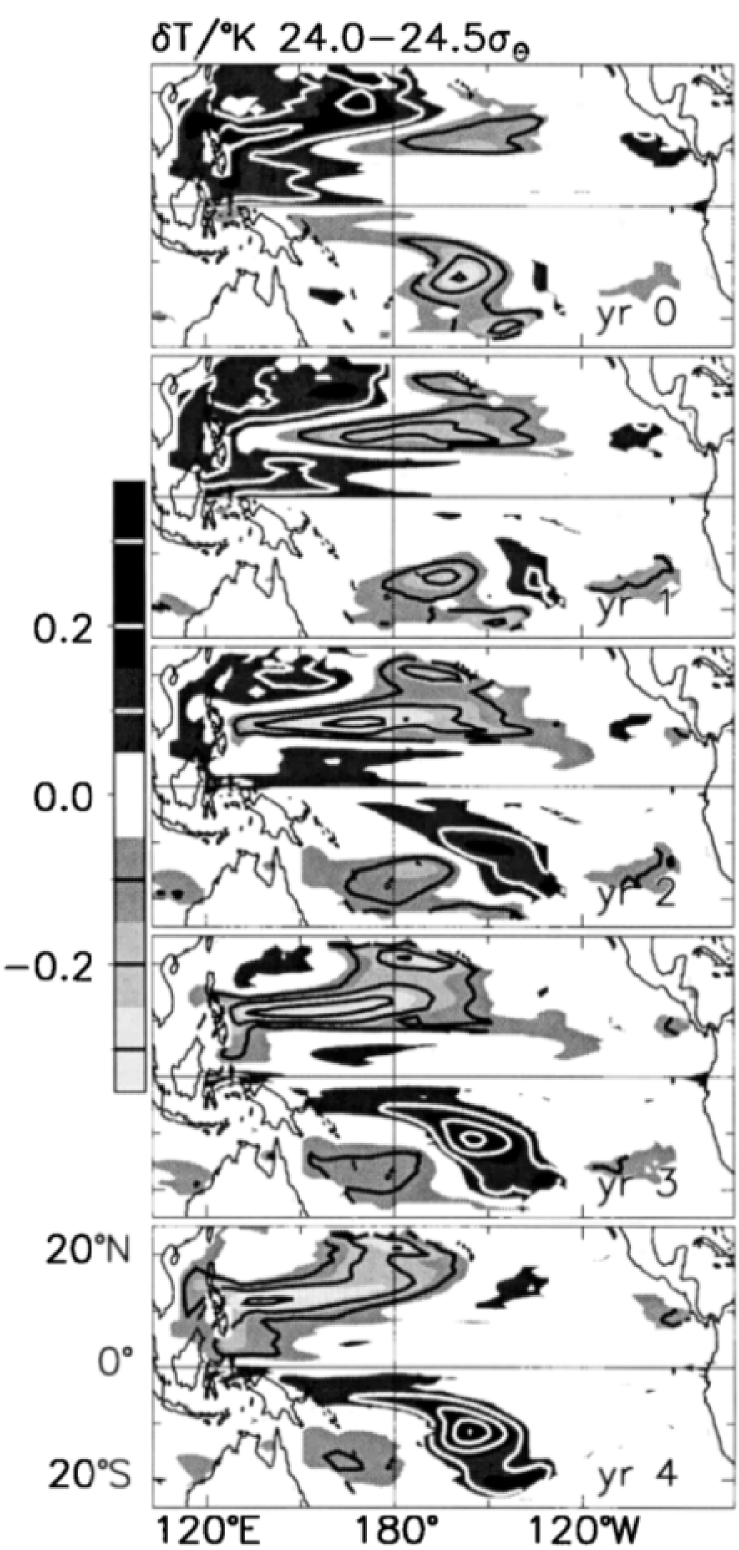

Figure 1.15: Reconstruction of the evolution of the spiciness mode during one half cycle as measured by temperature in the layer bounded by the 24.0 and 24.5 kg m^{-3} isopycnals. Contour interval is 0.1 °K and gray scale is given on left. The panels correspond to successive years (indicated in lower right corner), and the second half of the 10 year cycle is obtained by adding 5 years to the year counter and reversing the sign of anomalies. The reconstruction is obtained from the leading CEOF of the spiciness anomalies by multiplication of the spatial loading pattern with a constant, representative amplitude and linearly advancing phase corresponding to a typical period of 10 years. The leading CEOF explains 33% of the variance of the band passed filtered data in a 3 to 20 year period spectral window. Fitting an AR-1 process to this principle component yields a period of 9.9 years and a decay time of 24 years. Results are only contoured for those points where the CEOF explains more than 10% of the local variance (source: Schneider 2000). CEOF: Complex Empirical Orthogonal Function

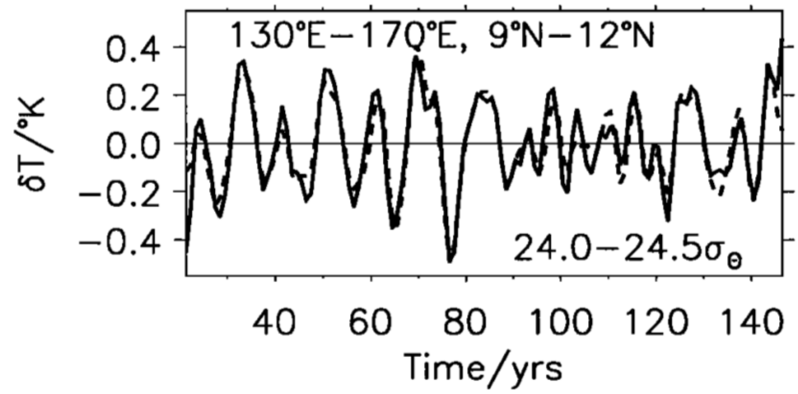

Figure 1.16: Evolution of spiciness in the western tropical Pacific as measured by temperature anomalies in °K on an isopycnal. The thick line shows anomalies between of the 24.0 and 24.5 kg m^{-3} isopycnals that are typical for the spiciness anomalies of the 22.0 to 26.0 kg m^{-3} surfaces. The reconstruction of the 24.0 to 24.5 kg m^{-3} spiciness anomalies from their leading CEOF is shown by a dashed line and explains over 90% of the local variance. All results have been band passed to allow variability with periods of 3 to 20 years only. Note the ten year time scale of spiciness on all isopycnals that is well represented by the leading CEOF (source: Schneider 2000). CEOF: Complex Empirical Orthogonal Function

1.5 Thesis Objectives and Structure

The main aim of this thesis is to advance our understanding of the ocean's role in driving tropical Pacific decadal variability. The research questions revolve around two major themes. First, we aim to reveal the drivers of the subtropical cells as they are known to actively contribute to TPDV. We specifically intend to determine the role of ENSO in driving the STCs and thereby influencing ENSO's own background state. Second, we aim to identify the impact of the "spiciness mechanism" on the tropical Pacific climate. To address these research questions, we conduct a range of model experiments using an ocean general circulation model and a Lagrangian particle simulator. We also compare and validate our results against observational records where available.

The following three Chapters (Chapter 2 to Chapter 4) are structured as individual manuscripts that have been or will be submitted for publication and as such, each Chapter includes a separate Introduction, Methods, Results and Discussion section.

For brevity, references from each of the individual Chapters are combined into a single bibliography included at the end of the thesis.

In Chapter 2, we investigate the volume transports related to the subtropical cells using a high resolution ocean general circulation model. We specifically analyse hemispheric differences in STC transports. We also utilise a set of experiments to investigate the mechanisms driving STC variability on both interannual and decadal time scales. We thereby intend to identify the role of interannual dynamics related to ENSO in modifying the mean climate in the tropical Pacific. This Chapter has been published as a research article in the *Journal of Geophysical Research: Oceans.*

In Chapter 3, we aim to answer the question whether spiciness anomalies generated in the subtropics can provide a means of inducing TPDV as has been proposed by previous studies. There still also is a scientific debate as to the preferred pathways spiciness anomalies take from the subtropics to the tropics which we aim to inform. We therefore carefully examine the relative importance of the different pathways of spiciness anomalies making use of a Lagrangian particle simulator. We also monitor the evolution of the magnitude of the spiciness anomaly to assess their potential impact on the tropical climate. This Chapter is to be submitted for publication in *Climate Dynamics.*

While spiciness anomalies have been suggested to contribute to TPDV, a quantitative assessment of their impact on the equatorial Pacific mixed layer heat budget is still lacking. In Chapter 4, we aim to close this gap by performing a heat budget analysis of this region and breaking down the advective term into the individual contributors, including spiciness as a separate contributor. A particular focus is made on the impact of remotely generated spiciness anomalies as they provide potential predictability of TPDV due to their travel time from the extratropics to the tropics. This Chapter is to be submitted for publication in *Geophysical Research Letters.*

In the final Chapter (Chapter 5), we discuss and conclude the main results of the individual studies that form part of the thesis. Also, an outlook to future research directions will be given in this Chapter.

Chapter 2

Hemispheric Asymmetry of the Pacific Shallow Meridional Overturning Circulation

This Chapter is based on the publication:

Zeller, M., McGregor, S., and Spcence, P. (2019), 'Hemispheric asymmetry of the Pacific shallow meridional overturning circulation', *Journal of Geophysical Research: Oceans*, doi: 10.1029/2018JC014840

Preface

The shallow subtropical cells (STCs) in the Pacific Ocean are thought to modulate the background state that the El Niño – Southern Oscillation (ENSO) operates in. This modulation is proposed to impact the frequency and intensity of ENSO events and their teleconnections. We use a high-resolution ocean model to investigate the volume transports associated with the STC branches along 5°N and 5°S. We find three prominent differences between the Southern hemisphere (SH) STC and the Northern hemisphere (NH) STC: i) the NH STC varies 26% stronger than the SH STC; ii) the NH STC appears to lead the SH STC by 3 months which causes the NH and SH STCs to play different roles during the course of El Niño and La Niña events; iii) in spite of the relative symmetry of the wind stress trends the STCs have differing decadal trends, with the SH STC clearly dominating the changes in the post-1993 period. To investigate the mechanisms driving the STC variability we identify winds that are linearly and non-linearly related to ENSO to force the ocean model. The hemispheric difference in interannual variance as well as the phase difference between the STCs can be explained with ENSO forcing. Our results suggest ENSO to be an important factor in modulating its own background state, with a prominent role for the winds that are non-linearly related to ENSO. The decadal trends and their interhemispheric disparity, however, cannot be reproduced by our targeted ENSO experiments.

2.1 Introduction

The tropical Pacific Ocean is the most influential region on climate patterns around the world (e.g., Alexander et al. 2002; Kosaka and Xie 2013, 2016). This region houses the Earth's most prominent interannual climate variation, the El Niño-Southern Oscillation (ENSO) (McPhaden et al. 2006). Besides the interannual variability of the coupled ocean-atmosphere system, the tropical Pacific Ocean also exhibits modulations on decadal time scales. The spatial pattern of these decadal modulations is captured by the Pacific decadal oscillation (PDO) or the Interdecadal Pacific Oscillation (IPO), both of which describe recurring patterns of sea surface temperature (SST) and associated atmospheric conditions over the Pacific domain (e.g., Mantua et al. 1997; Power et al. 1999).

The decadal variability can be thought of as the background state upon which ENSO operates (Fedorov and Philander 2001). Changes in this background state are thought to be closely linked to ENSO frequency and intensity (e.g., Zhao et al. 2016) as well as ENSO predictability by impacting the ocean dynamics that determine the lead-lag relationship between ENSO SST and its warm water volume precursor (e.g., Neske and McGregor 2018). Decadal changes in the tropical Pacific also serve as an explanation for the recent global warming hiatus (England et al. 2014). An enhanced understanding of the drivers of the decadal variability in this region is important for ENSO predictability and also for being able to distinguish between natural variability and human induced climate change.

Details of what drives the decadal variability of the tropical Pacific Ocean are currently still debated (Newman et al. 2016). Atmospheric teleconnections between the subtropics and the tropics (e.g., Barnett et al. 1999; Kwon et al. 2011) and between ocean basins (e.g., McGregor et al. 2014b; Chikamoto et al. 2016) may explain some portion of the decadal signal in the tropics. The focus of this study will be on the oceanic teleconnections between the subtropics and the tropics as important drivers of the tropical variability. We will investigate the oceanic teleconnections with emphasis on both the interannual and the decadal time scales as they both play a role in modulating the tropical Pacific climate.

Two complementary oceanic mechanisms connecting the tropical and subtropical Pacific Ocean can be distinguished. They are: i) the vertically integrated exchanges of upper ocean mass/heat that modulate the warm water volume (WWV) of the equatorial Pacific Ocean; and ii) the shallow ocean circulation cells, known as the Pacific subtropical cells (STCs), that extend from the tropics to the subtropics in both hemispheres and form part of the global ocean circulation system (McCreary Jr and Lu 1994; Liu et al. 1994; Lee and Fukumori 2003; Schott et al. 2004). WWV changes are normally utilised when discussing the dynamics of ENSO events (e.g., Jin 1997; Kug et al. 2003; McGregor et al. 2014a), while the Pacific STCs, which are the focus of this study, are generally used when discussing mechanisms of Pacific Decadal variability (e.g., Johnson and McPhaden 1999) which is strongly related to the volume and temperature of the water upwelled in the equatorial region. Each of the STCs is made up of different branches which can behave independently of each other (e.g., Capotondi et al. 2005). In the subtropics, cold water is subducted into the thermocline at depth from where it makes its way towards the tropics (Johnson and McPhaden 1999). Two distinct pathways for the subsurface limb have been explored, one along the western boundary as a western boundary current (WBC) and one through the ocean interior away from any boundaries (Liu et al. 1994; Izumo et al. 2002). At the equator, the water is upwelled along the equatorial undercurrent (EUC), before the overlying trade winds cause the upwelled water to diverge in poleward direction closing the loop (e.g., Johnson 2001). It should be noted that the two mechanisms are not entirely independent of each other. When the STC branches vary in phase the spin rate of the STCs increases or decreases impacting the rate of equatorial upwelling while having no effect on the mass balance which is the dominating factor in inducing changes in WWV. When the STC branches vary out of phase, however, the STCs contribute to upper ocean heat exchanges and therefore changes in WWV.

Most studies separate the equatorward STC transport into an ocean interior transport and a WBC transport (e.g., Lee and Fukumori 2003; Capotondi et al. 2005;

Izumo 2005; Cheng et al. 2007; Lübbecke et al. 2008; Hong et al. 2014). In all of these studies, the WBC opposes the interior transport at both interannual and decadal time scales. This leads to a partial compensation of the interior flow given that the WBC does not vary as much as the interior transports. A study by Ishida et al. (2008) identifies asymmetries in integrated upper ocean transport between the Northern hemisphere (NH) and the Southern hemisphere (SH) on ENSO time scales. Using a high resolution ocean model, the authors explain this asymmetry by indicating that the compensation between the interior and the WBC transports is higher in the SH than in the NH and that the limited compensation in the NH is underpinned by a phase lag between the WBC transports and the interior transports. However, Ishida et al. (2008) do not distinguish between surface and subsurface interior transports. The present study builds on the Ishida et al. (2008) study by looking at hemispheric asymmetries of the branches related to the STCs. The distinction of the vertical distribution of volume transport enables us to more accurately identify the reason for the hemispheric asymmetry in STC transports and relate the timing of the branches back to the forcing.

Hemispheric asymmetries of the STC transports can have a substantial climatic impact in the equatorial Pacific. Given the strong difference in mean pycnocline (σ_{24}-σ_{26}) temperatures (Figure 2.1) between the NH (roughly 17°C-22°C) and SH

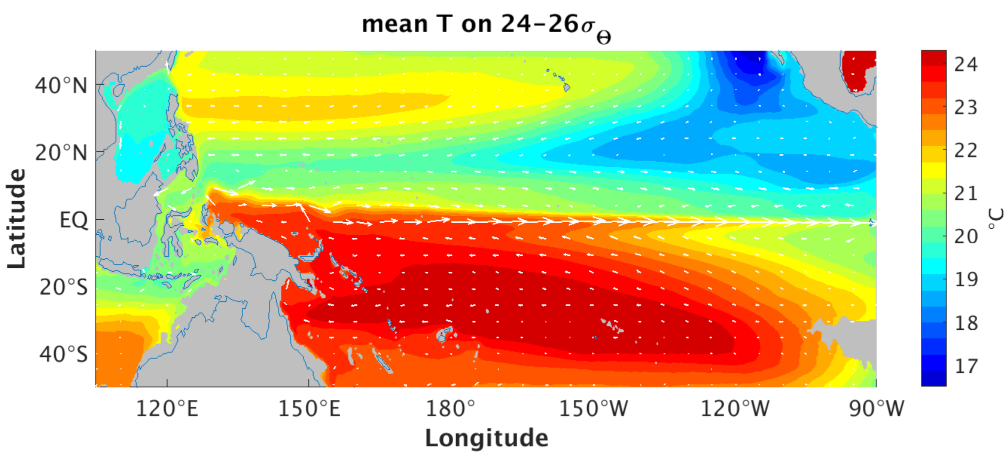

Figure 2.1: Time mean temperature averaged over the σ_{24}-σ_{26} isopycnal surfaces in the MOM025 control experiment.

(roughly 21°C-24°C), the relative contribution of each hemisphere‘s STC pycnocline transport has the potential to strongly influence the temperature of the water that is transported with the EUC and is then upwelled at the equator.

The STCs have been proposed to impact the decadal variability of the tropical Pacific Ocean in several ways. Early studies proposed that the equatorward advection of subducted temperature anomalies within the STCs play an important role (Gu and Philander 1997; Zhang et al. 1998; Giese et al. 2002). However, other studies found that subducted North Pacific temperature anomalies are dispersed before reaching the equator (Schneider et al. 1999a,b; Hazeleger et al. 2001b). According to Luo and Yamagata (2001), the advection of temperature anomalies from the subtropics to the tropics might still be effective in the Southern hemisphere. An alternative mechanism suggests that the anomalous STC volume transports can modulate the amount of cold subsurface waters that is advected into the tropics and upwelled to the surface along the equator where it interacts with the overlying atmosphere (Kleeman et al. 1999).

In support of the aforementioned theory, the different branches of the STCs have been found to strongly vary on interannual time scales (Lee and Fukumori 2003; Izumo 2005; Capotondi et al. 2005; Schott et al. 2007, 2008), whereby the STCs are closely linked to the ENSO cycle, with decreased overturning transport during El Niños and enhanced meridional transport during La Niñas (McPhaden and Zhang 2002; Izumo 2005). On decadal time scales, McPhaden and Zhang (2002) observed a decrease of the STC convergence at the thermocline depth of 11 Sv between the 1970s and 1990s at 9°N and 9°S, followed by a substantial increase of about 10 Sv between the 1990s and the early 2000s (McPhaden and Zhang 2004; Feng et al. 2010). Some studies expanded on this by including the trends of the WBC, resulting in much weaker decadal trends of the basin wide STC thermocline convergence than previously assumed (Lee and Fukumori 2003; Schott et al. 2007; Lee and McPhaden 2008). It should be noted, here, that the interannual variability of the STC branches is directly linked to the STC‘s decadal variability, e.g. through the interannually varying level of compensation between the WBC and the subsurface interior transport.

To draw conclusions on decadal changes in the tropical Pacific, we, therefore, ascribe importance to the understanding of both the interannual and the decadal variability of the STCs. There are several hypotheses as to what drives the STC interannual and decadal variability. They all agree on the surface winds being the driving force, however, what differs between these hypotheses is the location and the pattern of these winds. Nonaka et al. (2002), Lee and Fukumori (2003), Capotondi et al. (2005), and Izumo (2005) emphasise the importance of local (tropical) wind stress and wind stress curl for transport variations of the STC. In contrast, Kleeman et al. (1999) highlight the role of remote (off-equatorial) winds poleward of 23°. Farneti et al. (2014a) and McCreary Jr and Lu (1994) also point out the role of off-equatorial winds, however, they identify those that occur between about 15°-18° latitude as the primary driver of the low-frequency STC variability. The present study intends to identify the forcing of the individual STC branches (surface, subsurface interior, WBC) in each hemisphere as they may have distinct roles in impacting the decadal variability of the tropical Pacific. A particular focus of this study will be on the winds related to ENSO dynamics, following the idea that ENSO variability potentially self-regulates its low frequency background variations.

In this regard, a study of particular interest reveals a combination mode where the interannual (ENSO) and seasonal SST variability in the tropical Pacific form a nonlinear response in the atmospheric circulation (Stuecker et al. 2013). The corresponding circulation pattern features an anomalous Philippine anticyclone in the Northwestern tropical Pacific as well as a southward shift of westerly wind anomalies to the Southeastern tropical Pacific. Both features together result in a strong meridional shear of anomalous zonal wind across the equator. This atmospheric circulation, which has a nonlinear relation to ENSO, has been shown in previous studies to play a prominent role in the vertically integrated exchanges of upper ocean heat related to ENSO (McGregor et al. 2014a). However, its role in driving STC changes has yet to be fully explored. The present study aims to qualitatively and quantitatively assess the contribution of the transports induced by the nonlinear atmospheric forcing to the tropical Pacific overturning circulation.

Thus, in this study, we are not so much interested in how the STCs impact the tropical Pacific on decadal time scales, but more in what drives the STCs on both interannual and decadal time scales as we think it is important to first understand the dynamics behind the STC variability. As a next step, it is naturally worth to look at the actual impact of the STCs on the tropical climate. We investigate the physical mechanisms driving the STCs on interannual and decadal time scales, also asking how much ENSO itself can drive the modelled STC variability. For our analysis, we distinguish between winds that are linearly related to ENSO and non-linearly related to ENSO (combination mode). The fact that we make use of a high-resolution ocean general circulation model (OGCM) that resolves mesoscale variability in the tropics and subtropics enables us to realistically simulate the ocean‘s complex eddy structures at the Western boundary and tropical instability waves. It also allows for a separation of the different branches of the STCs that we expect to be more consistent with observations, specifically to distinguish between the WBC and the ocean interior flow. In previous studies, this distinction was hampered by a coarse model resolution (Izumo 2005; Capotondi et al. 2005).

The paper is structured as follows: in section 2 the OGCM as well as the wind forcing and the experimental setup are described. Section 3 gives an overview of the results, including the analysis of the co-variability between the STC branches at interannual and decadal time scales as well as the comparison of the ENSO forced experiments. Conclusions are discussed in section 4.

2.2 Model and Methods

2.2.1 The Ocean Model

The GFDL-MOM025 global coupled ocean sea-ice model is used for the analysis (Spence et al. 2014). This model is based on the GFDL CM2.5 coupled climate model (Delworth et al. 2012) and is coupled to the GFDL Sea Ice Simulator model. It has a 1/4° Mercator horizontal resolution globally with 50 vertical levels. The vertical level thicknesses range from 10m at the surface to about 200m at depth. Sea surface salinity is restored to a seasonally varying climatology on a 60 day time scale. The model is equilibrated with a 40 year spin-up control simulation forced with the ERA-interim climatology of heat, freshwater and momentum fluxes. Output is given as 5-day averages.

2.2.2 The Forcing

The ocean model is forced with atmospheric conditions derived from the ECMWF ERA-interim reanalysis product (Dee and Uppala 2009). The reanalysis product uses a variational bias correction system to account for the biases in satellite radiances. According to an assessment by Dee and Uppala (2009), the ERA-interim reanalysis provides an appropriate means for climate monitoring and analysis. The atmospheric conditions are converted to heat, freshwater and momentum fluxes across the ocean surface using the Coordinated Ocean-Ice Reference Experiments (CORE) bulk formulas. Using an inertial dissipative method the turbulent transfer coefficients (momentum, sensible heat, evaporation) are computed from 10 m wind speed, air temperature, and specific humidity. The forcing spans a time period of a bit more than 37 years from January 1979 to May 2016. Hence, the build-up phase of the most recent strong El Niño event of 2015/16 is included and could be used for the analysis. The ERA-interim winds were selected to overcome the strong trend biases in wind stress and wind stress curl over the tropical Pacific that are known to be present in the NCEP (National Centers for Environmental Prediction) wind product (McGregor et al. 2012a). McGregor et al. (2012a) found the spatial trend pattern of sea surface height (SSH) anomalies derived from NCEP winds to have a much lower spatial correlation (0.41) when compared with observed SSH anomalies than those derived from ERA-interim winds (0.83). It is noted that this choice moved us away from the more balanced fluxes of CORE forcing (Large and Yeager

2009), but it is more appropriate to address the proposed research questions.

2.2.3 The Experiments

We performed four experiments which are analogous to those of McGregor et al. (2014a) and extended them to 2016. The experiments all use the same climatological heat and freshwater forcing but they differ in their wind forcing. Experiment 1 is referred to as EXP_{FULL} as it is forced with the full ERA-interim wind field. For the three ENSO targeted experiments, the idea is to decompose the complex ocean dynamics response to ENSO into several more digestible components that are more intuitive and easier to understand. The decomposition is done on the equatorial Pacific surface wind stress forcing utilising linear regression and an EOF analysis. Prior to this, wind velocities are converted to wind stresses according to the quadratic stress law

$$\begin{pmatrix} \tau_x \\ \tau_y \end{pmatrix} = C_d \rho_a \begin{pmatrix} u \\ v \end{pmatrix} W, \tag{2.1}$$

where τ_x and τ_y are the horizontal wind stresses, C_d is the drag coefficient ($C_d = 1.5e^{-3}$), ρ_a is the reference atmospheric density ($\rho_a = 1.2\frac{kg}{m^3}$), u and v are the horizontal wind velocities, and W is the surface wind speed.

Experiment 2 only utilises wind stress anomalies that are linearly related to the ENSO cycle. This is achieved by regressing global wind stresses onto the Nino3.4 time series which is a direct indicator of the ENSO phase (SSTs are derived from ERSST version 4). As the Nino3.4 index is very close to the PC1 time series of wind stresses within the equatorial Pacific region (120°E-60°W, 10°N-10°S, corr=0.71) (cf. McGregor et al. 2014a), the resulting regression map largely coincides with the first EOF of the same region (spatial corr: 0.93). Due to its linear relationship with ENSO, the experiment is named $ENSO_{LIN}$ (Figure 2.2 a,c). We note that the fixed nature of this experiment is not entirely realistic as it does not represent

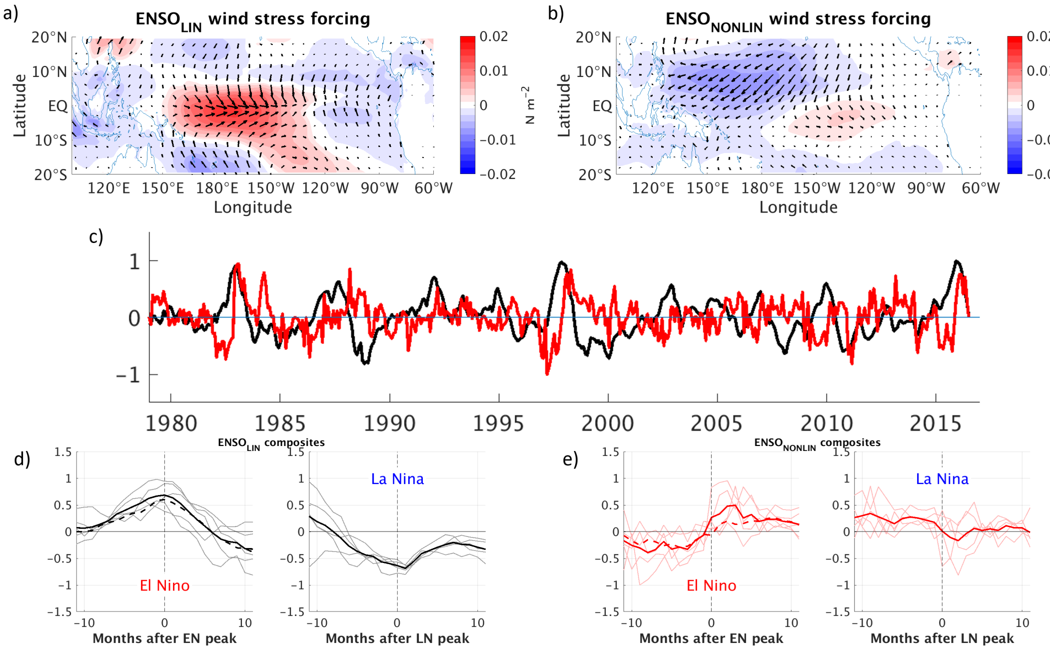

Figure 2.2: Wind stress patterns that are **a**) linearly related to ENSO ($ENSO_{LIN}$, linear regression against Nino3.4 index) and **b**) nonlinearly related to ENSO ($ENSO_{NONLIN}$, EOF2 of equatorial wind stresses). The zonal component is shaded where red means eastward. **c**) Time evolution of $ENSO_{LIN}$ (black) and $ENSO_{NONLIN}$ (red) wind stress forcings. **d**) and **e**) show the composite mean time series around EP El Niño (solid, 1982/83, 1987/88, 1991/92, 1997/98, 2002/03), CP El Niño (dashed, 1994/95, 2004/05, 2009/10, 2015/16) and La Niña (1988/89, 1998/99, 1999/2000, 2007/08, 2010/11) events for $ENSO_{LIN}$ and $ENSO_{NONLIN}$ wind stresses, respectively. Transparent lines show the single events. All time series are normalised and the patterns are standardised with the standard deviation of their time evolution.

the seasonally varying wind response to SST forcing. To produce the wind forcing we calculate the regression pattern using wind stress anomalies with respect to the climatology despite the fact that previous studies have reported a seasonal dependence of the wind response to SST forcing (e.g. Yang et al. 2001; Lengaigne et al. 2006). This dependence is characterised by a migration of anomalous winds from the North in boreal summer to the South in boreal winter. However, the annual meridional migration of winds is implicitly included in our analysis for strong ENSO events (see following two paragraphs).

Experiment 3 utilises wind stress anomalies that have a non-linear relationship with ENSO. To this end, we first subtract wind stress anomalies related to $ENSO_{LIN}$ from the EXP_{FULL} wind stress anomalies, globally. We then compute the first EOF of the residual wind stress in the tropical Pacific region (120°E-60°W, 10°N-10°S). This EOF is very similar to the EOF2 of the original wind stress field (PC corr: 0.83; spatial corr: 0.92) The resulting principle component time series (Figure 2.2c) is finally regressed onto the global residual wind stress field to obtain the associated global structure (Figure 2.2b). McGregor et al. (2012a) have demonstrated that this wind stress pattern represents a physical mechanism by which during the peak phase of large ENSO events the westerly wind response to anomalous eastern equatorial Pacific SST shifts southward which constitutes a key element in the termination of large El Niño events. Further, Stuecker et al. (2013) have shown that the origin of the wind stress pattern is the nonlinear atmospheric response to combined seasonal and interannual tropical Pacific SST changes. Due to the nonlinear relation to ENSO, this experiment is termed $ENSO_{NONLIN}$.

Experiment 4 uses the sum of $ENSO_{LIN}$ and $ENSO_{NONLIN}$ wind stress anomalies. It is therefore referred to as $ENSO_{ALL}$ and includes all wind stresses that are related to ENSO. As demonstrated in McGregor et al. (2012b) this combined experiment does well simulate the observed anomalous southward wind shift which also represents the seasonal dependence of SST forcing and wind response. To produce the final wind forcing of each of the aforementioned experiments, the wind stress anomalies of $ENSO_{LIN}$, $ENSO_{NONLIN}$, and $ENSO_{ALL}$ are each added to the wind stress climatology and converted back to wind velocities by which the ocean model is forced.

Except where the study's focus is on the evolution of STCs during ENSO events (section 2.3.2.3), our analysis is carried out on 12-month moving averages of anomalies with respect to the mean seasonal cycle and the linear trend of the period 01/1979-05/2016. All correlations and linear trends are significant at the 90% confidence level unless indicated otherwise. Significance is computed using a bootstrap approach with 10,000 iterations. To account for the monthly dependence of the data, a reduced number of degrees of freedom has been applied. Assuming that any one year (January-December) is independent of all other years we divide the time series into yearly chunks of 12 months length. Each bootstrap sample time series is created by sampling with replacement from the 37 individual years. The resulting time series is then correlated with the second time series of interest. Given 37 years of model data this leaves us with 37 degrees of freedom.

2.2.4 Definition of the STC Branches

The spatial extent of the two STCs and their branches is defined on the time mean as this is where these cells are most clearly identified. Bearing in mind that the STC transports change with the distance from the equator we choose 5° latitude for two main reasons: i) we want to capture the strong and meridionally close to uniform zonal winds corresponding to the linear theory of the build up and decay of El Niño events, and ii) we want to be reasonably close to the equator, without interfering with the equatorially confined tropical cells, to ensure that the equatorward flow of pycnocline water across this latitude band actually feeds the EUC which then distributes the water to the surface at the equator. Another advantage of choosing 5° latitude is the opportunity to compare our results to other model studies (e.g., Izumo 2005) as well as observational studies (e.g., Meinen and McPhaden 2000; Meinen et al. 2001).

In spite of this, questions still remain over whether 5° latitude is an adequate latitude to examine the STCs (Hazeleger et al. 2001a) given the possible existence of tropical cells (TCs) that re-circulate equatorial waters in a meridionally narrower and shallower cell than the STCs do (e.g., Hazeleger et al. 2001a; Izumo 2005). However, these studies show that TC downwelling occurs at 3°-5° latitude while the major horizontal flow of these cells occurs between 1°-3° latitude. Thus, the predominant portion of the transports across 5° latitude form part of the STCs and therefore also constitute source water of the EUC. This is corroborated by the relatively high coherence of the individual branches at 5° and 9° latitude (Figure 2.3).

An exception is the NH surface branch which behaves very differently between the

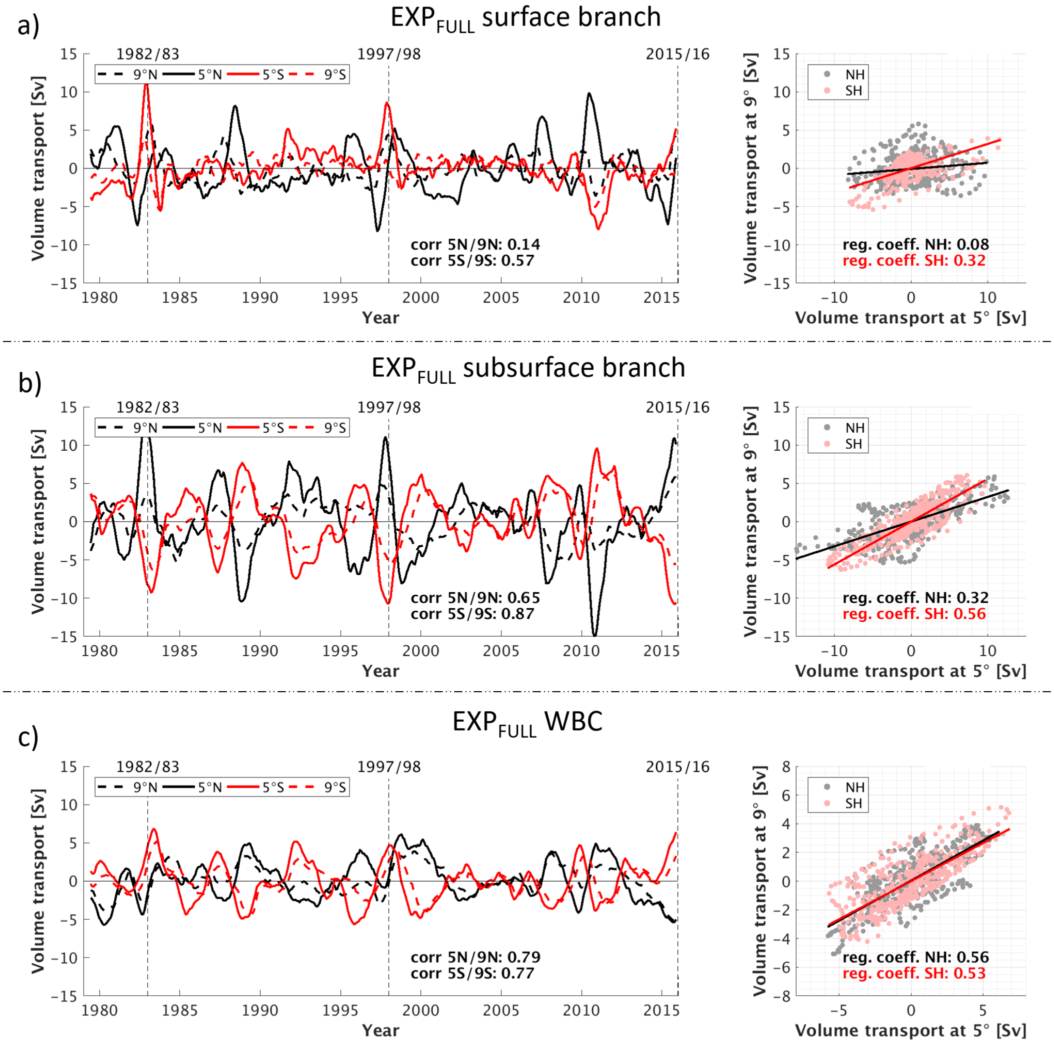

Figure 2.3: Transport anomalies of **a**) the surface branch, **b**) the subsurface interior branch, and **c**) the WBC in EXP_{FULL}. Transports integrated across 5°N (solid black), 5°S (solid red), 9°N (dashed black), and 9°S (dashed red) are plotted as time series and as scatter plots. The vertical dashed black lines indicate the strong El Niño events of 1982/83, 1997/98, and 2015/16. Positive means northward transport. The correlation between 5°N and 9°N in a) is insignificant at the 90% confidence level.

two latitudes, a fact that is also expressed in the insignificant correlation between the two latitudes. The different behaviour can be explained with the wind forcing (Figure 2.2 a,b). At 9°N, the surface branch is almost exclusively forced by the $ENSO_{NONLIN}$ winds with no contribution by the $ENSO_{LIN}$ winds while at 5°N both forcings play a role.

For the time mean in EXP_{FULL}, the vertical structure of the meridional flow in the tropical Pacific shows a clear distinction between the surface and the subsurface (Figure 2.4 a,b). At the surface, the water is largely diverging from the equator following Ekman dynamics induced by the overlying easterly trade winds (Figure 2.4e). At the subsurface, the basin-wide baroclinic zonal pressure difference induces geostrophic convergence (Figure 2.4f). As a separation between the surface

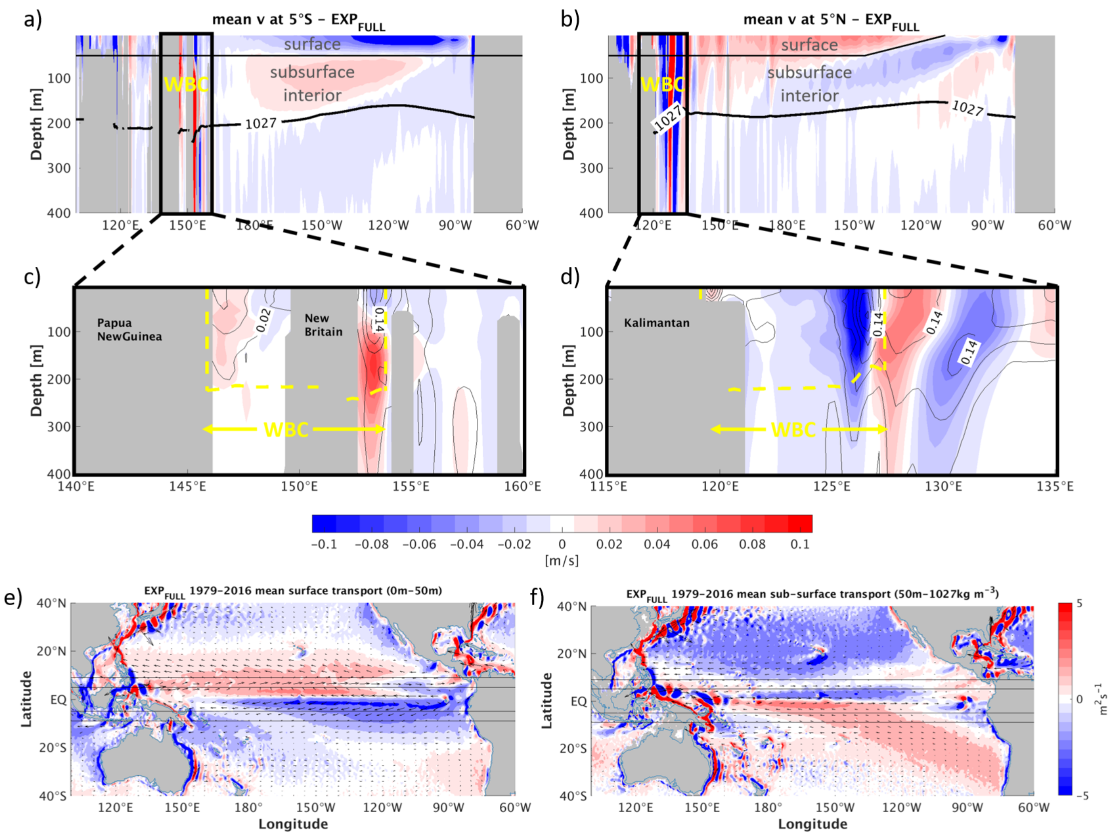

Figure 2.4: Mean meridional velocity (v) along **a**) 5°S and **b**) 5°N, in the upper Pacific Ocean in EXP_{FULL}. **c**) and **d**) are enlargements of the respective Western boundary regions. Mean of 01/1979-05/2016. Red shading means northward flow. Horizontal black line indicates the lower vertical boundary of the surface branch at 50 m (except slope at 5°N). Curved solid black line indicates the lower vertical boundary of the subsurface branch at σ_{27}. Note that the velocities need to be multiplied by 5 in panels c) and d). Black contours in panels c) and d) indicate the std of v. The contour interval is 0.4 $\frac{m}{s}$. **e**) and **f**) show maps of mean transport (meridional transport is shaded) integrated across the surface layer (0-50m) and the subsurface layer (50m-σ_{27}), respectively. The horizontal lines indicate the 5° and 9° latitudes in each hemisphere.

and subsurface branch most studies use the 50 m level, sometimes combined with the 1022 $\frac{kg}{m^3}$ isopycnal (e.g., Lee and Fukumori 2003; Izumo 2005; Capotondi et al. 2005). Figure 2.4 shows that at 5°S the 50 m level seems adequate so we use this as the boundary between the surface and subsurface branch. At 5°N, however, the surface Ekman flow seems to be confined to the basin interior with no transport east of 105°W. Instead, the equatorward subsurface flow rises to the surface between 145°W-105°W. To adapt to the changing surface-subsurface boundary, we choose the 50 m level west of 145°W and introduce a linear slope east of 145°W that reaches the surface at 105°W. East of this longitude, our definition accounts for no surface branch but only a subsurface branch.

To further separate the subsurface branch from the deep ocean we use the 1027 $\frac{kg}{m^3}$ isopycnal ($\sigma_{27} = \rho_{1027}$-1000 $\frac{kg}{m^3}$) as the lower boundary. In comparison with the ORAS4 reanalysis, the depth of the model's σ_{27} is about 20 m shallower and the pycnocline appears to be slightly narrower in the model. However, depths of neutral density levels (not shown) along which geostrophic flow is assumed to occur are very close to observations at 5°N and 5°S (Johnson and McPhaden 1999). Moreover, the integration depth of 150-250 m is in the same range as in earlier studies (e.g., Lee and Fukumori 2003; Izumo 2005; Capotondi et al. 2005) (150-300 m) and, importantly, the subsurface transport integration occurs over the range of isopycnals feeding the EUC (100-250 m).

Model studies have shown that there exist two main pathways for the equatorward pycnocline flow, one along the western boundary and one through the interior ocean (e.g., Liu et al. 1994; Lee and Fukumori 2003; Capotondi et al. 2005). As the WBC is subject to different dynamics than the interior flow, it is defined here as a separate branch. To be consistent with the vertical extent of the interior transport, the WBC is integrated from the surface down to σ_{27} (Figure 2.4 c,d). The actual WBC reaches depths of about 1000 m which is much deeper than what we include here, however, the transports according to both definitions have a very similar variability and only differ in their mean and slightly in their standard deviation (not shown). Considering that we are interested only in the anomalies justifies our definition.

Another issue is the longitudinal extent of the WBC. Owing to the lack of a continuous continental shelf in the western Pacific, we define the western edge of the western boundary region manually at each latitude such that it includes the WBC but not any currents west of that. This distinction is especially important around the equatorial region where the impact of the Indonesian Throughflow (ITF) becomes large. It is important to note that the ITF is defined as its own branch and is differentiated from the STCs. It was shown that the presence or absence of the ITF does not considerably impact the STC transports (Lee and Fukumori 2003).

To separate the WBC from the ocean interior we define a "core" WBC at each latitude, which is defined as the meridional transport integrated across 3° longitude and vertically integrated from the surface to σ_{27}. The "core" WBC is then correlated with the vertically integrated meridional transport at each longitude. Based on this method, the eastern edge of the WBC is defined as the last longitude (from west to east) before the correlation crosses the zero line. From this analysis, we get the following widths for the WBC at the respective latitude: 8.25° at 5°N and 8° at 5°S. Interior transports are, thus, defined as everything east of the western boundary until the eastern coastline of the Pacific. This applies for both surface and subsurface branches.

In order to examine the variability of the STCs we define an index of the combined NH and SH STC transport. We integrate the meridional velocity horizontally and vertically according to the above definition of the STC branches. The STC index is then computed as follows, with northward (southward) transport being positive (negative):

$$\begin{aligned} STC_{idx} &= STC_{NH} + STC_{SH} \\ &= (SFC - SUB - WBC)_{NH} + (SUB + WBC - SFC)_{SH}, \end{aligned} \tag{2.2}$$

where SFC, SUB and WBC denote the surface, subsurface and WBC branches of the STC. NH and SH refer to the Northern and Southern hemisphere, respectively.

2.2.5 Model Validation

The model mean state is validated against observational and reanalysis data. Where possible, the time periods of comparison have been chosen to be the same between model and observations. The mean state of the tropical Pacific is very close to the ORAS4 reanalysis with high spatial correlations of sections across 5°N/5°S for mean meridional velocity (0.75/0.95) and mean density (0.99/0.996). The mean STC strength in the EXP_{FULL} control experiment is stronger in the Southern hemisphere (35 Sv) than in the Northern hemisphere (29 Sv), This is consistent with Lohmann and Latif (2005) who found the overturning to be 40 Sv and 25 Sv for the Southern and Northern hemisphere STC at the same latitudes, respectively, using a stream function to define the STC index. Table 2.1 shows a comparison of the model versus observed mean STC transports. The mean Ekman divergence of 49 Sv as computed from the Era-interim wind stress is comparable to but somewhat weaker than the one calculated from ERS-1,2 scatterometer wind stresses (58 Sv) across the same latitudes (Schott et al. 2004). In terms of the boundary currents, the mean SH WBC is measured at 15 (±15) Sv using gliders (Davis et al. 2012), while the model mean of 8.1 Sv is only about half, yet within the range of uncertainty. Butt and Lindstrom (1994) observed the SH WBC to mainly occur through the straits between Papua New Guinea and New Britain and between New Britain and New Ireland, which is consistent with our model (cf. Figure 2.4c). In the Northern hemisphere, Wijffels

Table 2.1: Model versus observed mean transports of surface, subsurface interior and WBC branches of the STCs at 5°S and at 5°N. Units are Sv. Positive means northward transport. Numbers in brackets indicate the interval of confidence.

	EXP_{FULL}	Observations
Ekman divergence	49	58
NH WBC	-14.4	-14 (±1.5)
SH WBC	8.1	15 (±15)
NH interior	-3.2	-5 (±1)
SH interior	10.6	15 (±1)

et al. (1995) used ADCPs to measure the Mindanao Current to be 23 (±4) Sv on average of which 9 Sv turn west and form part of the ITF (Gordon et al. 1999) while the remaining 14 (±1.5) Sv feed the EUC (Johnson and McPhaden 1999). The latter number coincides with the modelled 14 Sv of the mean NH WBC. An observational validation of the mean SH subsurface interior transports (Figure 2.4a) is given by Zilberman et al. (2013) who observed meridional geostrophic velocity derived from Argo floats at 7.5°S (their Figure 3a). Spatially, the mean subsurface transports extend from 170°E-90°W both in the model and in the observations. Also the vertical extent of the mean equatorward transports compares well between model and observations, reaching down to a maximum of about 200 m between 170°W-150°W and shoaling towards the east reaching the 50 m level at about 100°W. Zilberman et al. (2013) observe an amplitude of 5 $\frac{cm}{s}$ for the geostrophic velocity below the 50 m level which is slightly higher than the modelled amplitude of 4 $\frac{cm}{s}$ for the subsurface branch. The strong southward velocity simulated at the Eastern boundary was also detected by the Argo floats and corresponds to the Peru-Chile Undercurrent as discussed by Montes et al. (2010) (their Figure 3 c,d). The integrated mean equatorward interior transports in EXP_{FULL} amount to 3.2 Sv and 10.6 Sv for the Northern and Southern hemisphere, respectively. This is in qualitative agreement with the observed transports by Johnson and McPhaden (1999) amounting to 5 (±1) Sv and 15 (±1) Sv, respectively, although with reduced magnitude.

The interannual variability of the model upper ocean transport (surface to pycnocline) at 9° latitude is comparable to the observed Ekman and geostrophic transports across 8° latitude in Meinen and McPhaden (2001) (their Figure 9) showing similar peaks around ENSO events. The modelled temporal evolution of the STC subsurface branches at both 5° and 9° latitude is also consistent with the geostrophic transports calculated by Bosc and Delcroix (2008) from observed sea level anomalies at 5° and 8° latitude. However, the amplitude of the modelled STC transport at 5° and 9° latitude is about half compared to the observations.

2.3 Results

2.3.1 STC index variability

The fully forced (EXP_{FULL}) STC index calculated at 5° latitude exhibits large temporal variations of up to +/-30 Sv (mean: 73 Sv), especially around El Niño and La Niña events (Figure 2.5 a). During El Niños the STCs slow down, meaning that less subtropical water intrudes the tropics and is upwelled along the equator. Also, at the surface less water escapes from the tropical region. This process is reversed during La Niñas when the STCs are strong and lead to an increase of subtropical water in the tropical region.

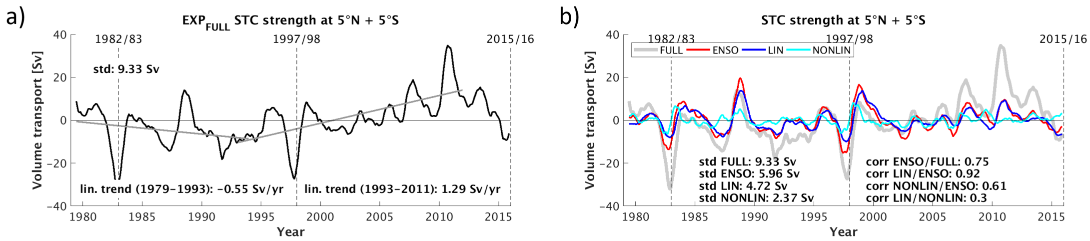

Figure 2.5: **a**) Anomalies of STC strength at 5°N + 5°S for EXP_{FULL}. The linear trend for the period 01/1979-05/2016 has not been removed here. The linear trends for the periods 1979-1993 and 1993-2008 are plotted as grey lines, however, the linear trend in the earlier period is insignificant while it is significant in the latter period at the 90% confidence level. The standard deviation and the linear trends are displayed in the plot. **b**) Anomalies of STC strength at 5°N + 5°S. Grey: EXP_{FULL}, red: $ENSO_{ALL}$, blue: $ENSO_{LIN}$, and cyan: $ENSO_{NONLIN}$. The vertical dashed black lines indicate the strong El Niño events of 1982/83, 1997/98, and 2015/16. Positive means anomalously strong STC.

A good agreement exists with the $ENSO_{ALL}$ STC index variance explaining 56% of the EXP_{FULL} STC index (corr: 0.75, Figure 2.5 b). $ENSO_{ALL}$ reaches about 2/3 of the standard deviation of EXP_{FULL}. Further breaking down the forcing shows that the linear wind stress forcing seems to play the dominant role explaining 85% of $ENSO_{ALL}$. The $ENSO_{NONLIN}$ STC index explains 37% of $ENSO_{ALL}$ and shows clear peaks during ENSO events, also suggesting a non-negligible role for $ENSO_{NONLIN}$.

On decadal time scales, the STC index also shows some variation which can be represented by the two linear trends before and after the observed phase shift in the tropical Pacific in the mid 1990s (McPhaden and Zhang 2004). EXP_{FULL} shows a decreasing linear trend for the time period 1979-1993 and a reversed trend after that (Figure 2.5 a). These trends are consistent with other model studies as well as observations (e.g., McPhaden and Zhang 2002; Lee and Fukumori 2003; McPhaden and Zhang 2004; Capotondi et al. 2005). Interestingly, for the targeted ENSO experiments ($ENSO_{ALL}$, $ENSO_{LIN}$, $ENSO_{NONLIN}$), neither of the two linear trends can be reproduced with a reasonable magnitude (Figure 2.5 b). A detailed investigation of the linear trends is presented in section 3.2.4.

2.3.2 Hemispheric separation of STC variability

As the STC index may mask some of the variability by combining the NH and SH STCs, we now analyse the STCs in each hemisphere separately. Examining the Northern and Southern hemispheric contributions to the total EXP_{FULL} STC transport reveals three fundamental differences (Figure 2.6 a): i) the NH STC displays interannual transport variability that is approximately 26% larger than that of the SH STC; ii) the two STCs do not occur simultaneously. Rather, the NH STC leads the SH STC variations by 3 months; consequently, the behaviour of the NH STC during El Niño/La Niña events strongly differs from the behaviour of the SH STC; iii) the decadal linear trend present in the STC index after 1993 is much more prominent in the SH STC.

Each of these hemispheric disparities and their physical origin are examined in detail in the following sub-sections utilising the ENSO targeted experiments. By comparing $ENSO_{ALL}$ to EXP_{FULL} we are able to estimate to what extent the STCs can be reproduced by only forcing them with winds that are linked to ENSO. By means of $ENSO_{LIN}$ and $ENSO_{NONLIN}$ we can further draw conclusions about the physical mechanism behind the STC transports.

2.3.2.1 Hemispheric difference in interannual transport

We find that on interannual time scales the variability of the NH STC (std: 5.7 Sv) is 26% larger than that of the SH STC (std: 4.5 Sv) in EXP_{FULL} (Figure 2.6 a). Looking at the individual branches of the STCs in EXP_{FULL} reveals two things. Firstly, the compensation between the subsurface interior and WBC branches is high in both hemispheres. Secondly, the compensation between the surface and the combined subsurface interior plus WBC branches is larger in the SH (corr:-0.75, Figure 2.6 b,c). This alone would imply a stronger SH STC variability. However, even though the degree of compensation is slightly weaker in the NH, the STC branches themselves display a stronger variability, which leads to the increased variance of the NH STC. The exception is the WBC which displays similar variability in both hemispheres.

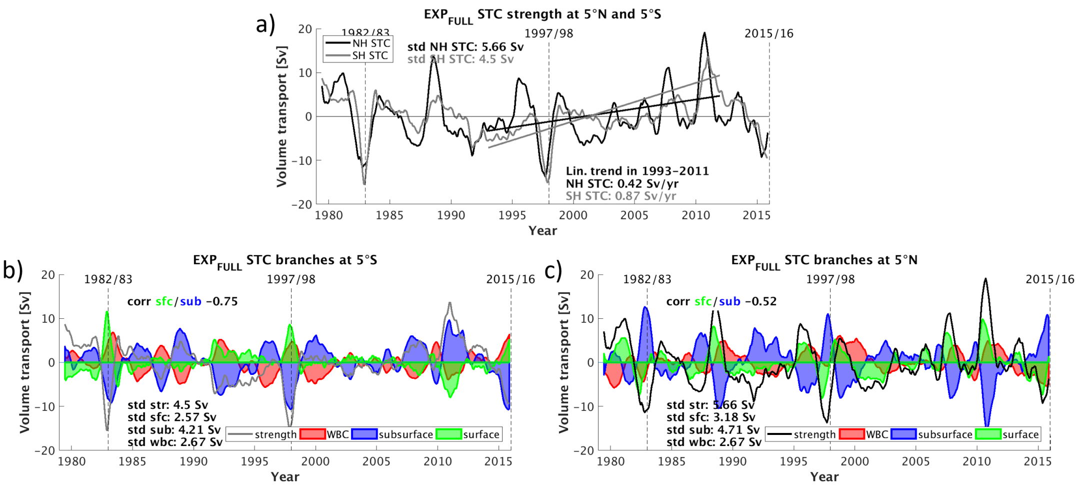

Figure 2.6: **a**) Anomalies of STC strength at 5°N (black) and 5°S (grey) for EXP_{FULL}. Standard deviations and correlation coefficients between the hemispheres as well as the linear trend are displayed in the plot. Positive means anomalously strong STC according to STC index. Panels **b**) and **c**) show the transport anomalies of the different branches of the STC integrated at 5°S and 5°N, respectively, for EXP_{FULL}. Solid grey/black line: STC strength, green shading: surface branch, blue shading: subsurface interior branch, red shading: WBC. Standard deviation of each branch and correlation coefficients between the surface branch and the sum of subsurface interior and WBC are displayed in each plot. The vertical dashed black lines indicate the strong El Niño events of 1982/83, 1997/98, and 2015/16. Positive means northward transport for the branches and anomalously strong STC for STC index.

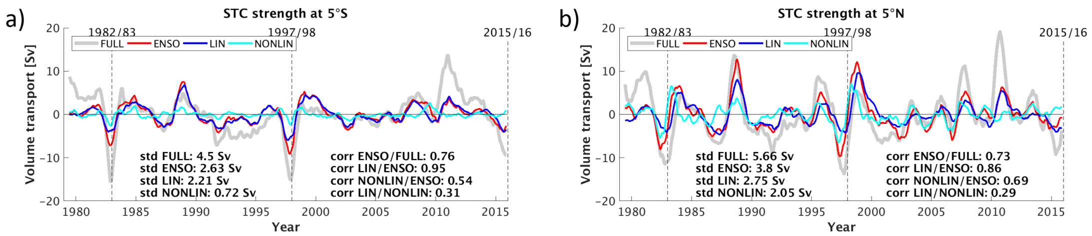

Figure 2.7: Anomalies of STC strength at **a**) 5°S and **b**) 5°N for all experiments. Grey: EXP_{FULL}, red: $ENSO_{ALL}$, blue: $ENSO_{LIN}$, and cyan: $ENSO_{NONLIN}$. Standard deviations and correlation coefficients between the experiments are displayed in the plot. The vertical dashed black lines indicate the strong El Niño events of 1982/83, 1997/98, and 2015/16. Positive means anomalously strong STC.

Here we investigate whether this hemispheric difference can be reproduced with the ENSO experiments. Analysing the $ENSO_{ALL}$ experiment output reveals that the hemispheric difference as discovered in EXP_{FULL} is reproduced reasonably well (Figure 2.7). On the basis that in $ENSO_{ALL}$ the NH STC (3.8 Sv) varies with 44% more intensity than the SH STC (2.63 Sv), we first take a look at the $ENSO_{LIN}$ experiment which represents the common linear view of ENSO dynamics. The interannual variance of $ENSO_{LIN}$ transports is 24% larger at 5°N (2.75 Sv) compared to 5°S (2.21 Sv). Thus, including the variability generated by $ENSO_{NONLIN}$ is synonymous with adding another 20% of hemispheric difference in interannual variance. This is taking into account the relative amplitudes of the $ENSO_{LIN}$ versus $ENSO_{NONLIN}$ transports.

The question can be raised why the $ENSO_{LIN}$ wind stresses generate stronger transport variability in the NH even though the wind stresses themselves vary stronger in the SH (Figure 2.2a). The answer is twofold. First, the surface branches are forced by the zonally integrated wind stresses, i.e., even though the centre of maximum variability is in the SH, the variability of the integrated wind stress along 5°N and 5°S is about the same in each hemisphere resulting in approximately equal Ekman variability. Second, the variability of the wind stress curl is stronger in the NH where it induces a stronger geostrophic flow (not shown). The resulting STC overturning transport, therefore, varies stronger in the NH.

We summarise this section by stating that the hemispheric disparity in the magnitude of the variance of the STCs can well be reproduced by forcing the STCs with ENSO related winds only. This is due to both the $ENSO_{LIN}$ and $ENSO_{NONLIN}$ winds with comparable contributions.

2.3.2.2 Covariability of the STCs in both hemispheres

As discussed above, the EXP_{FULL} STCs are not symmetric about the equator in terms of their transport variance. Focusing on the evolution of the STCs over time reveals that they are also not symmetric temporally, i.e. they do not vary synchronously. The NH STC seems to lead the SH STC by 3 months (lagged corr: 0.75, zero lag correlation: 0.68, Figure 2.6 a). This finding is qualitatively consistent with earlier studies that noticed that the zonal wind stress and the accompanying meridional Ekman transport at 5°N leads the one at 5°S (Meinen and McPhaden 2001; Alory and Delcroix 2002; Kug et al. 2003; Izumo 2005). The lag is well captured by the $ENSO_{ALL}$ experiment (lag: 4 months, lagged corr: 0.87, zero lag correlation: 0.71, Figure 2.8 a), i.e. ENSO related winds appear to be responsible for the lag.

Based on the results of the previous section exhibiting a high compensation between the subsurface interior and the WBC transports in both hemispheres, we here combine these two branches to one branch and refer to it as the "subsurface branch". Looking for the source of the lag in EXP_{FULL} (Figure 2.8 b), we find that the STC subsurface branches in the NH and SH are fairly synchronous (corr: -0.69 at zero lag). The SH surface branch also displays a strong temporal similarity to the NH and SH subsurface branches, which is reflected by the correlation coefficients of 0.78 and -0.75 at zero lag, respectively (not shown). The NH surface branch, on the other hand, displays its strongest correlation with the SH surface branch when it leads by 7 months (lagged corr: -0.66, zero lag correlation: -0.30). This result indicates that the source of the lead/lag relationship is in the NH surface transports. The lead time of 7 months only applies to the NH STC surface branch, while the SH surface branch and the subsurface branches (interior+WBC) of both hemispheres

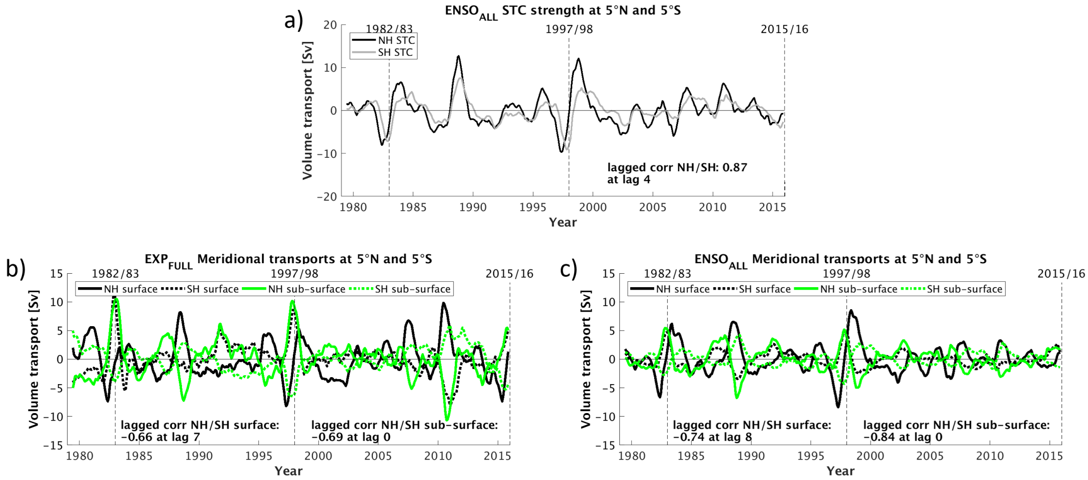

Figure 2.8: **a**) Anomalies of STC strength at 5°N (black) and 5°S (grey) $ENSO_{ALL}$. Positive means anomalously strong STC according to STC index. Anomalies of the STC branches at 5°N (solid) and 5°S (dashed) for **b**) EXP_{FULL} and **c**) $ENSO_{ALL}$. Black: surface branch; green: subsurface interior branch + WBC. Lagged correlation coefficients between the hemispheres are displayed in each plot. The vertical dashed black lines indicate the strong El Niño events of 1982/83, 1997/98, and 2015/16. Positive means northward transport.

act synchronously (zero lag).

As the STC index is computed as surface-subsurface (NH) and subsurface-surface (SH), respectively, and the magnitudes of the surface and subsurface branches are similar, the lead-lag relationship of the STC indices is the average of the surface and subsurface lags. This yields the lag of 4 months for the STC index. Again, we find the same lead/lag relationships between all branches in $ENSO_{ALL}$ (Figure 2.8 c), reinforcing our hypothesis that ENSO related winds are the primary cause for the lag.

Comparison of the $ENSO_{ALL}$ experiment with $ENSO_{LIN}$ and $ENSO_{NONLIN}$ reveals a strong temporal consistency between the $ENSO_{ALL}$ and $ENSO_{LIN}$ transports in the SH (see correlations in Figure 2.7 a). This means that the SH STC is largely forced by winds that are linearly related to ENSO, i.e. primarily by the strong zonal winds between ~5°S-5°N. These winds are also the underlying forcing of the warm water volume (WWV) changes as explained by the recharge-discharge-oscillator (RDO) theory, with anomalous westerlies (easterlies) leading to a WWV discharge (recharge) through the slow ocean adjustment via upwelling (downwelling) Rossby waves. This suggests that the SH STC largely follows the linear RDO theory.

In contrast, the influence of $ENSO_{LIN}$ is smaller in the NH STC where $ENSO_{NONLIN}$ also appears to play a prominent role (see correlations in Figure 2.7 b). The cyclonic structure in the Northwestern tropical Pacific wind field (Figure 2.2 b) induces Ekman transport that primarily affects the NH surface branch (e.g., McGregor et al. 2014a). The time evolution of the $ENSO_{NONLIN}$ wind stresses is out of phase with the $ENSO_{LIN}$ wind stresses (see Figure 2.2 b,c). Thus, the associated Ekman transports according to each forcing are out of phase, too. This result is consistent with Table 2 in Izumo (2005). Consequently, the lead time of 8 months for the $ENSO_{ALL}$ surface branches is consistent with the lead time between the two wind forcing time series (7 months, Figure 2.2 c). Plotting only the NH surface branch for all experiments confirms that its major contributor is the $ENSO_{NONLIN}$ experiment (Figure 2.9). $ENSO_{NONLIN}$ explains 77% of the variance of $ENSO_{ALL}$ and reaches clearly higher amplitudes than $ENSO_{LIN}$. Nonetheless, the contribution by $ENSO_{LIN}$, although weaker than the $ENSO_{NONLIN}$ contribution, is also clearly apparent and far from being negligible.

Summarising this section, we can say that the 3-month lag between the NH STC and SH STC transport has its origin in the NH surface branch. Moreover, we know that ENSO related winds are responsible for the phase shift. In particular, it is the cyclonic wind stress pattern over the North Western tropical Pacific corresponding to $ENSO_{NONLIN}$ that induces the lag between the hemispheres as seen in the fully forced STCs. The reason for the phase shift is the southward shift of anomalous zonal wind stress during an ENSO event. These winds are first shifted north early in an ENSO event and they then migrate southward (McGregor et al. 2012a). The cause of the southward wind shift has been investigated by earlier studies which relate the shift to the climatological weakening of the wind speeds south of the equator toward the end of the calendar year (MccGregor et al. 2012a; Stuecker et al. 2013).

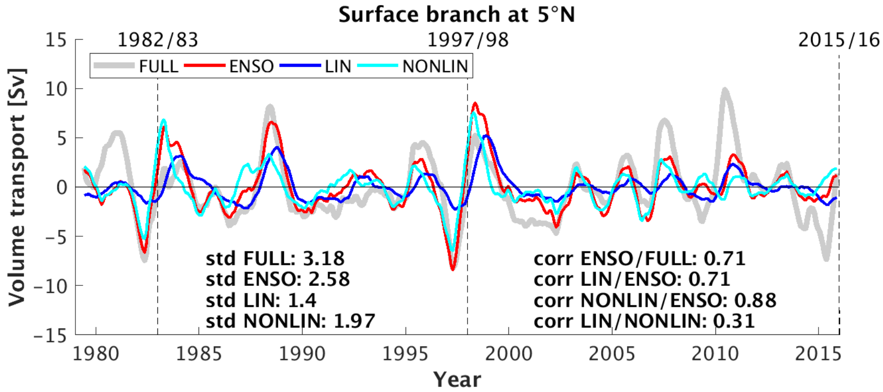

Figure 2.9: Anomalies of the NH STC surface branch at 5°N for all experiments. Grey: EXP_{FULL}, red: $ENSO_{ALL}$, blue: $ENSO_{LIN}$, and cyan: $ENSO_{NONLIN}$. Standard deviations and correlation coefficients between the experiments are displayed in the plot. The vertical dashed black lines indicate the strong El Niño events of 1982/83, 1997/98, and 2015/16. Positive means northward transport.

2.3.2.3 Evolution of El Niño/La Niña events

The phase difference between the STCs, as described in the previous section, causes them to play different roles during the development and decay of El Niño and La Niña events. The focus of this section is to analyse how the NH and SH STC evolve during the ENSO cycle. We therefore here apply a 3-month moving average to emphasise interannual variations. We distinguish between Eastern Pacific (EP) El Niños and Central Pacific (CP) El Niños following the "Nino" methodology set out by Yu and Kim (2013). Based on the Oceanic Nino Index (running 3-month mean SST anomaly averaged over the Nino3.4 region), we select the five strongest EP El Niños and the four strongest CP El Niños as well as the five strongest La Niña events from the 1979-2016 period to build event composites (Figure 2.2 d,e). It is noted that four of the five strongest El Niño events in our time period are EP types and only one is a CP type. Our analysis therefore mainly focuses on the EP type El Niño events. Again, the combination of the subsurface interior and the WBC transports is referred to as "subsurface branch" motivated by the compensating effect of the former two.

EP type El Niño events

We are first going to look at the average temporal evolution of the STCs in EXP_{FULL} during the EP type El Niño events (Figure 2.10). Prior to an El Niño event peak, the NH surface branch has the biggest influence as its transport strongly decreases between January to September of the El Niño year, slowing the NH STC. Around the event peak (Oct-Feb), the NH STC becomes stronger again due to a rapid switch of the surface branch towards positive anomalies, despite an ongoing gradual decrease in transport of the subsurface branch. During this peak period, the SH STC transport reduces significantly due to reductions in the transports of both the surface and subsurface branches. It is noted that the STC reduction in both hemispheres is dominated by the surface branches whose changes are roughly double those of the subsurface branches in the respective time periods given the partial compensation of the subsurface interior transport through the WBC.

During the event decay and post event (Mar to Nov of the year after the event), the NH surface branch remains anomalously strong while the SH surface branch changes sign and becomes strong, as well, further increasing the rate of the STCs. The NH subsurface branch adds to the STC strengthening later in the year (from August) while there is no effect of the subsurface branch in the SH integrated over this period. It should be noted that the enhanced STCs towards the end of the composite time frame are caused by the fact that El Niño events are mostly followed by La Niña events (Figure 2.2 c). Hence, what is actually shown is the build-up phase of a subsequent La Niña event. Looking at the STC evolution of the individual EP El Niño events, depicted by the grey shading in Figure 2.10a and b, reveals some diversity between the individual ENSO events. Still, the events tend to display similar characteristics in each hemisphere to the mean during all ENSO phases.

The ENSO forced ($ENSO_{ALL}$) STC composites have a very similar temporal evolution to the fully forced simulation described above, although with reduced amplitudes (correlation coefficients of all composite time series lie between 0.77-0.98). This confirms that the ENSO forcing ($ENSO_{LIN}$+$ENSO_{NONLIN}$) as defined in our study is sufficient to reproduce the temporal evolution of the STC branches during

El Niño/La Niña events.

We now break the ENSO driven STC down into linear and nonlinear ENSO changes to provide a better understanding of the drivers. Looking into the SH changes firstly, we find that the temporal evolution of the SH STC El Niño composite closely follows the linear ENSO theory ($ENSO_{LIN}$). The nonlinear forcing ($ENSO_{NONLIN}$) in the Southern hemisphere has a very minor impact on the SH STC. As to the NH STCs, both the $ENSO_{LIN}$ and $ENSO_{NONLIN}$ forcings play equivalent roles in the subsurface transports. At the surface, on the other hand, the transport is almost exclusively forced by the nonlinear wind stresses ($ENSO_{NONLIN}$). Specifically, the switch of a weak to a strong NH surface branch just prior to the event peak coincides with the switch of the tropical Northwest Pacific anti-cyclone to a cyclone. Thus, nonlinear wind stress forcing is required to explain the NH STC changes with maximum weakening occurring prior to the event peak.

CP type El Niño events

We also analyse the STC evolution during Central Pacific (CP) El Niños (dashed line in Figure 2.10). The temporal evolution of the STC strength resembles the EP evolution, although with only about 60% of the amplitude for the STC minimum prior to the event peak in both hemispheres. After the peak time the SH STC reaches the same strength for both El Niño types, while the NH STC regains much greater amplitude after CP El Niños. This strong regeneration after CP El Niño events is likely related to the development of La Niña events after every CP El Niño which is not the case for EP El Niño events.

We find that the ENSO driven part of the CP El Niños is almost exclusively driven by $ENSO_{LIN}$ winds, while $ENSO_{NONLIN}$ winds have no effect in either hemisphere. Figure 2.2e shows that the $ENSO_{NONLIN}$ winds are much weaker during the CP El Niño events explaining the minimal effect of these winds for the CP type of event. The strong regeneration of the STC strength at 5°N is not captured by the ENSO related winds. This suggests that the difference between EP and CP El Niño events lies in the residual winds. It also suggests that the $ENSO_{NONLIN}$ wind stress

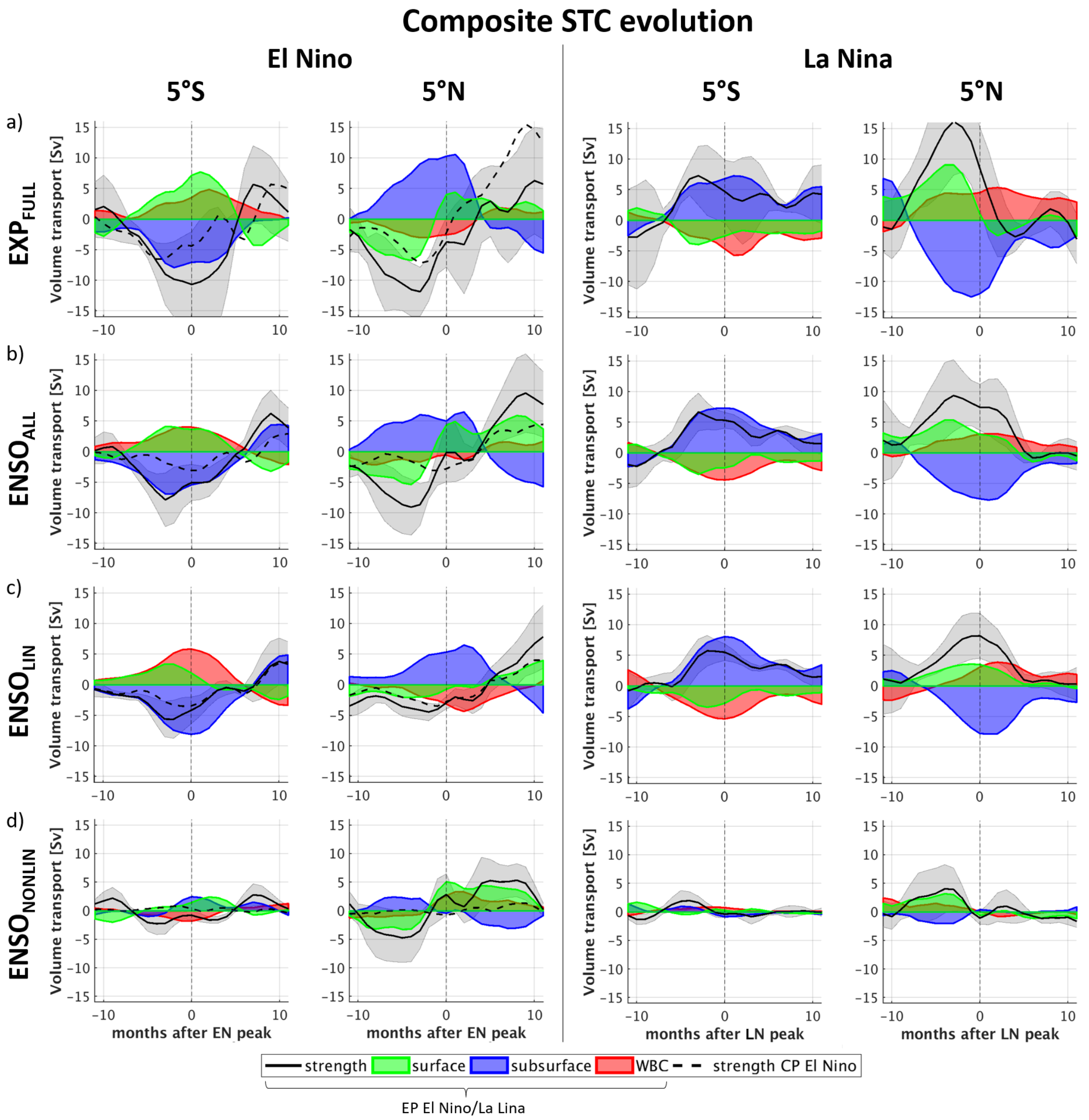

Figure 2.10: El Niño composites (1982/83, 1987/88, 1991/92, 1997/98, 2002/03, left column) and La Niña composites (1988/89, 1998/99, 1999/2000, 2007/08, 2010/11, right column) of the anomalous branches of the STC at 5°N and 5°S for **a**) EXP_{FULL}, **b**) $ENSO_{ALL}$, **c**) $ENSO_{LIN}$, and **d**) $ENSO_{NONLIN}$. Solid black line: STC strength for EP El Niño/La Niña events, grey shading: spread of single events, green shading: surface branch, blue shading: subsurface interior branch, red shading: WBC, dashed black line: STC strength for CP El Niño events (1994/95, 2004/05, 2009/10, 2015/16). The vertical dashed black line indicates the month of the event peak. Shown are the 11 preceding and following months of the event. A 3-month moving average has been applied to the data prior to analysis and plotting. Positive means northward transport for the branches and anomalously strong STC for the STC strength according to STC index.

pattern is predominantly related to EP El Niño and not CP El Niño events, which is corroborated by the minimal effect of $ENSO_{NONLIN}$ winds on the STC strength during CP El Niño events (cf. Figure 2.10d).

La Niña events

We now consider the evolution of the fully forced STCs during La Niña events (Figure 2.10). During the event growth period (Jan-Sep), the NH STC is largely responsible for the increase in STC transport. Both the surface and subsurface play a role in these NH STC changes, but as the surface transport lead those of the subsurface (i.e., NH surface transports peak 3 months prior to the event peak, while the subsurface transports peak 1 month prior to the event peak) they appear to be more important during this event growth phase. During the event peak (Oct-Feb), the NH surface branch returns to its mean value while the NH subsurface branch is at its peak strengthening magnitude. The SH STC branches start strengthening around July midway through the event growth period, and reach their peak magnitude in October. These SH STC changes occur in both the surface and subsurface maintaining a similar level through the event peak and decay in the following year. The ongoing strong SH STC goes back to the fact that La Niña events are usually followed by another La Niña event. In contrast to the SH STC, the NH STC returns back to normal within 4 months from the event peak.

Consistent with the El Niño composites, the ENSO forced ($ENSO_{ALL}$) La Niña composites reproduce the temporal evolution of the EXP_{FULL} composites in both hemispheres quite well. Looking to better understand the drivers of the STC changes, we break the ENSO driven STC down into its linear and nonlinear components. We find that the SH STC is solely forced by $ENSO_{LIN}$ event composite winds, as $ENSO_{NONLIN}$ winds produce only very small changes of SH STC transport (Figure 2.10). For the NH STC, both linear and nonlinear winds play an essential role. In the pre-event period, the nonlinear winds induce a strong NH surface branch which enhances the transport of the NH STC. Then during the event peak (Oct-Feb), the linear winds become the dominant contributor, forcing a strong NH STC, while the STC contribution of the non-linear winds returns to zero. During the event decay

(Mar-May), the $ENSO_{LIN}$ winds diminish and the NH STC returns to mean values.

Effect of STC transport variations on equatorial heat content

The STCs can affect the equatorial heat content through variations in their transport ($v'\overline{T}$ mechanism), without the need for the transport of off-equatorial temperature anomalies to the equator. At the surface, the diverging branches of the STCs transport warm water out of the equatorial region. At the subsurface, relatively cold water that has previously been subducted in the subtropics is brought into the equatorial region via the STC subsurface branches. Consequently, an increased overturning rate of the STCs comes along with more warm water leaving and more cold water entering the equatorial region, thus with a decreased heat content. Conversely, "slow" STC overturning results in an increased equatorial heat content.

ENSO summary

In summary, we can state that the temporal evolution of the SH STC largely follows the linear ENSO theory with zonal easterly (westerly) winds generating an accelerated (decelerated) STC. However, in contrast to theory these changes are most prominent in the surface transports, which means that much less upper ocean heat content is lost from the equatorial region to the Southern hemisphere. This result is consistent with earlier studies (Kug et al. 2003; McGregor et al. 2014a; Izumo et al. 2019). Note again that the subsurface branch is defined as the sum of subsurface interior and WBC transports. The variation of the subsurface interior transport is still dominating the surface and WBC transport variations. While the linear component is important in the NH STC changes during ENSO events, as well, the nonlinear winds also play a prominent role. Their influence is most apparent during the build-up and decay phase of El Niño events, when the NH STC is largely forced by $ENSO_{NONLIN}$ winds. For La Niña events, the impact of $ENSO_{NONLIN}$ winds is most important during the build-up phase. In both cases, the nonlinear winds act to shift the peak of anomalous NH STC changes to earlier in the event evolution period.

2.3.2.4 Multi-decadal changes

Here, we focus on understanding the longer term variability of the STCs which are thought to be related to changes in the background state in which ENSO operates. Observational studies have looked at the decadal variability of the Pacific Ocean's dynamics by means of changes in the average state over decade-long time periods (e.g., McPhaden and Zhang 2002, 2004). Accordingly, McPhaden and Zhang (2002) found a decrease of the STC convergence at 9°N and 9°S of about 0.5 $\frac{Sv}{yr}$ prior to the 1990s, followed by a substantial increase of about 1 $\frac{Sv}{yr}$ between the 1990s and the early 2000s (McPhaden and Zhang 2004).

Our analysis is done at 5° latitude but, when using the same time periods, we find qualitatively similar trends. The total STC (5°N+5°S) decreases by 0.56 $\frac{Sv}{yr}$ between 1979-1993. It subsequently increases by 0.98 $\frac{Sv}{yr}$ between 1993-2008. However, McPhaden and Zhang (2004) did not consider the STC trend in each hemisphere separately, only discussing the combined trend of the pycnocline convergence (9°S-9°N).

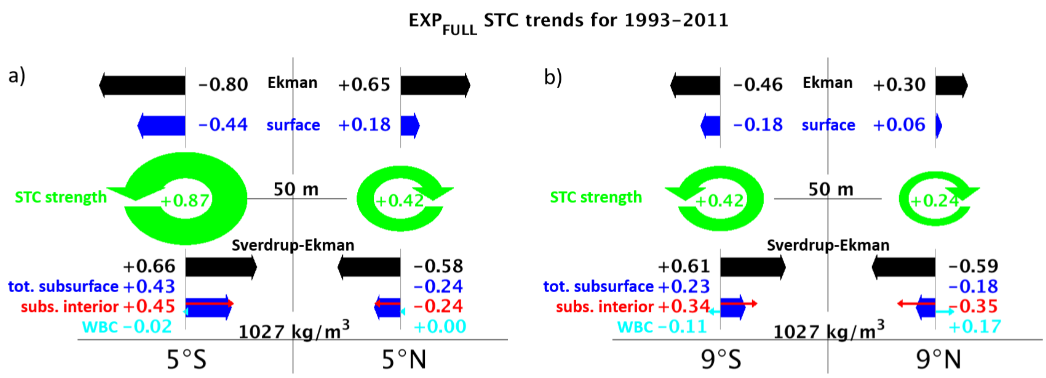

Figure 2.11: Linear trend of STC transports (Sv/yr) at **a**) 5°S and 5°N and **b**) 9°S and 9°N in EXP_{FULL} for the period 1993-2011. The blue arrows indicate the trends of the surface branch (above circle) and the subsurface branch (below circle). The subsurface branch is separated into the subsurface interior trend (red) and the WBC trend (cyan). Also shown are the trends of the Ekman transport (above circle) and the geostrophic transport (below circle) derived from the wind forcing of EXP_{FULL} (black). The trend values are stated next to the corresponding arrows, where positive (negative) values represent an increase in northward (southward) transport. The circle indicates the trend of the STC strength and is the sum of the surface, subsurface interior and WBC trends in their mean direction. The WBC trends at 5°S and 5°N are insignificant at the 90% confidence level.

Following from there, we take a look at the trends of the individual STCs. To rule out possible discrepancies in the first couple of model years right after the model initialisation, we focus our analysis of the decadal STC changes on the period from 1993-2011. This period also captures the peak of the recent Pacific trade wind intensification (McGregor et al. 2018) and both its start and its end mark phase changes in the Pacific decadal state (e.g. Hare and Mantua 2000; Bond et al. 2003). It is therefore reasonable to take this representative period when analysing the decadal changes of the STCs.

In EXP_{FULL}, the decadal variability of the STCs at 5°N and 5°S appears asymmetric across the hemispheres (Figure 2.11a). The SH STC ($+0.87\ \frac{Sv}{yr}$) increases at double the rate as the NH STC ($+0.42\ \frac{Sv}{yr}$). The surface and subsurface interior branches change at a very similar rate within each hemisphere, although much stronger in the SH. The WBC does not appear to play any role in the STC spin up in both hemispheres during this period. Specifically, we do not find a compensation of the subsurface interior and WBC branches at 5° latitude, as Lee and Fukumori (2003) and Capotondi et al. (2005) did at 9° latitude. The STC trends at 9°N and 9°S are generally weaker than at 5°N and 5°S. However, the fact that the difference in trends is also seen at 9°N and 9°S (Figure 2.11b) gives us confidence that the meridional STC asymmetry is not dependent on the choice of latitude. None of these trends in STC transport is produced by the targeted ENSO simulations (Figure 2.5 b), a result which is consistent with past work (e.g., England et al. 2014). To better understand these changes we estimate surface and subsurface transports from the linear trend of the surface wind stress forcing in EXP_{FULL} (Figure 2.12).

We expect the surface branches to be primarily forced by the overlying zonal wind stress and the accompanied Ekman transport. The zonal wind stress trend averaged across 5°N is 27% weaker than across 5°S (Figure 2.12a). The corresponding Ekman transports have according trends (Figure 2.11). However, the trends in the surface branches, in particular at 5°N, are much weaker than what Ekman theory suggests (72% weaker at 5°N, Figure 2.11).

As to the subsurface interior branch, Sverdrup theory suggests that this is forced by the basin-wide zonal pressure gradient which generates a geostrophic transport in meridional direction. The geostrophic transport can either be calculated directly from the sea surface height or as a residual by subtracting the Ekman transport from the Sverdrup transport, where the Sverdrup transport is derived from the wind stress curl. For both methods, the theoretically expected trend in geostrophic transport is approximately equal in both hemispheres (Figure 2.12b). However, the trend of the modelled subsurface interior branch at 5°N is only about half of that at 5°S (Figure 2.11).

Owing to the poor agreement between the modelled branches and the theoretical transports, we conducted a multilinear regression analysis to determine the relative contributions of the Ekman and geostrophic components to the modelled surface

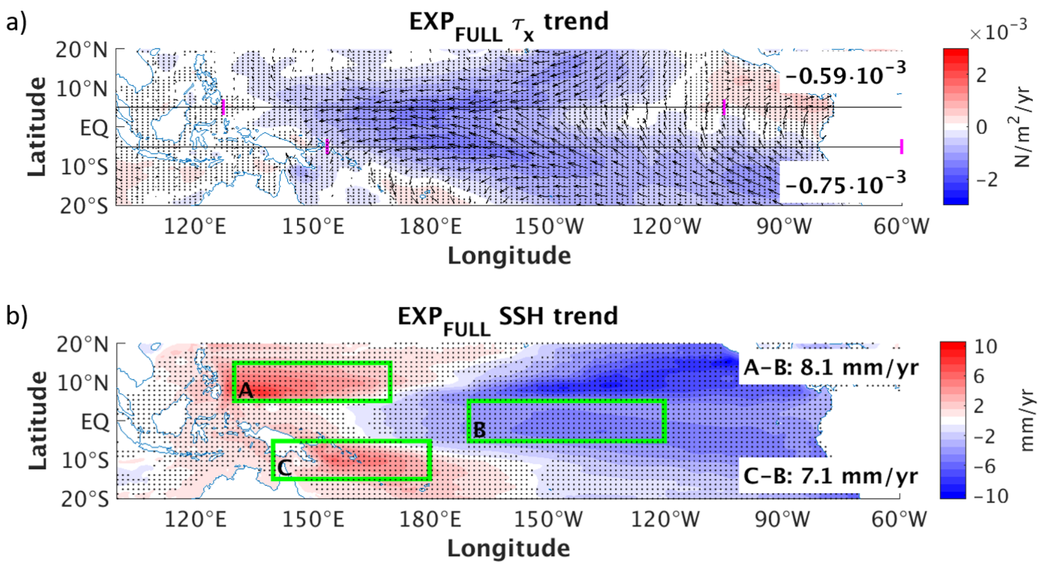

Figure 2.12: Linear trend for the period 1993-2011 in EXP_{FULL}. **a**) wind stress (zonal component τ_x shaded). The horizontal lines indicate the latitudes 5°N and 5°S. The numbers indicate the trends zonally averaged across the basin between the magenta lines. Red means increased eastward wind stress. **b**) sea surface height (SSH). Boxes A and B are the same as used by Feng et al. (2010), while box C is added to represent the SH trend. The numbers indicate the differences between the box averages. Red means increased sea surface height. In a) and b) the stippling indicates regions of significant trends at the 90% confidence level.

and subsurface STC branches (Tab. 2.2). We therefore solve the set of Eq. 2.3 for the parameters a, b, c, and d which quantify the Ekman and geostrophic components, respectively. A least squares estimation is applied in order to minimise the deviation of the observed data points from the fitted regression.

$$\begin{aligned} SFC &= \mathbf{a} \cdot T_{Ek} + \mathbf{b} \cdot T_{Geo} \\ SUB &= \mathbf{c} \cdot T_{Ek} + \mathbf{d} \cdot T_{Geo} \end{aligned} \tag{2.3}$$

The analysis reveals that at 5°S the ocean dynamics controlling these branches are consistent with linear and steady Ekman and Sverdrup theories. The surface branch is mainly driven by the Ekman component but is also partly influenced by the geostrophic transport, which explains the reduced trend of the modelled branch compared to that expected by calculations of Ekman transport. These findings are in accordance with Izumo (2005) who found a similar relation between theoretical and actual transports on interannual time scales.

At 5°N, however, Sverdrup theory cannot explain the weak modelled trends for both the surface and subsurface interior branch in EXP_{FULL}. The modelled surface branch trend is only 28% of the trend in Ekman transport, while there is no geostrophic influence in the surface layer according to the multilinear regression analysis. The modelled trend in subsurface interior transport is 41% that of the geostrophic transport and in contrast to the SH, the NH subsurface transport appears to be strongly influenced by Ekman transport (Tab. 2.2).

Table 2.2: Regression coefficients for the multilinear regression of surface and subsurface STC branches against Ekman and geostrophic transports at 5°S and at 5°N.

	5°S		5°N	
	Ekman	Geo	Ekman	Geo
surface	0.83	0.33	0.36	-0.02
subsurface	0.03	0.64	0.31	0.72

To further investigate this unexpected behaviour of the decadal trends at 5°N, we

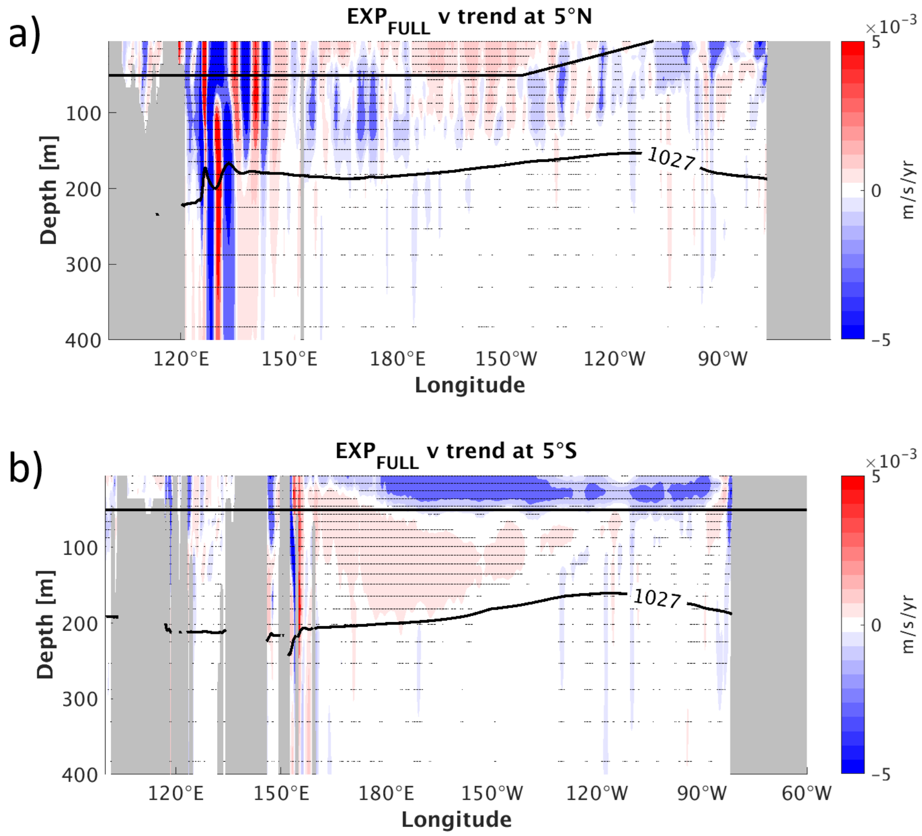

Figure 2.13: Linear trend of meridional velocity (v) for the period 1993-2011 in EXP_{FULL} across **a**) 5°N and **b**) 5°S. Red means increased northward velocity. The stippling indicates regions of significant trends at the 90% confidence level.

plot a section of the meridional flow showing its trend at each grid point across the basin at 5°N and 5°S (Figure 2.13). The plot shows that at 5°N the linear trends do not coincide with the definition of the branches. Instead, positive and negative trends are highly mingled across the 50 m level. Because of the interference between the surface and subsurface branches the linear trends of the two branches are partially cancelling. This explains the strongly reduced trends that we find for the modelled STC branches at 5°N. The origin of this vertical interference is thought to be the high eddy activity across 5°N (Chen et al. 2015b). At 5°S, on the other hand, the two branches can be clearly separated by means of the decadal trends.

Summing up, we find a strong hemispheric discrepancy for the decadal trends between 1993-2011. The trends at 5°S are in accordance with the driving forces and the theory. The strongly reduced trend of the NH STC can be traced back to enhanced vertical interference at 5°N. Our targeted experiments ($ENSO_{ALL}$, $ENSO_{LIN}$, $ENSO_{NONLIN}$) can not reproduce any trend implying that the multi-decadal variability of the STC transport is not influenced by ENSO dynamics (Figure 2.5 b).

2.4 Discussion and Conclusions

We have analysed the shallow overturing circulation in the Pacific Ocean by means of a high-resolution ocean model forced by observed atmospheric conditions. Using a set of model experiments based on different wind forcings we could relate the features of the STC variability to the oceanic and atmospheric processes that drive them. Our analysis leads to the following conclusions.

The temporal evolution of the interannual variability of the STCs can well be reproduced by forcing the ocean only with winds that are linearly and non-linearly related to ENSO ($ENSO_{ALL}$). In terms of variance, $ENSO_{ALL}$ generates about 2/3 of the STC transport forced by the total wind variability (EXP_{FULL}). This suggests that ENSO related winds play an important role in driving the STCs on interannual time scales. Given the strong relationship between STC subsurface convergence and equatorial SST (e.g., Izumo 2005; Capotondi et al. 2005), these winds evidently impact the climate of the tropical Pacific on these time scales.

The hemispheric difference in transport variance that was found for the STCs on interannual time scales appears to be induced by winds related to ENSO. The differing transport variance is nearly equally explained by the equatorial zonal wind stresses related to $ENSO_{LIN}$ and by the $ENSO_{NONLIN}$ wind stresses. In addition to the study by Kug et al. (2003) who divided the winds that are linearly related to ENSO into hemispherically symmetric and anti-symmetric parts, we find the winds with a nonlinear relationship to ENSO almost double the hemispheric disparity in ocean transports. It is also noted that both Kug et al. (2003) and McGregor et al. (2014a) focus on the upper ocean mass exchange (integrated from the surface to the pycnocline), while the present study examines how the rate of the NH and SH STC branches varies with the different forcings which ultimately changes the rate of upwelling at the equator.

We find a temporal asymmetry of the STC transports in the two hemispheres, whereby the NH STC leads the SH STC by 3 months. As most studies concentrate on the subsurface STC convergence which is proposed to occur in phase across the hemispheres (e.g., Cheng et al. 2007; Lübbecke et al. 2008; Schott et al. 2008; Farneti et al. 2014a; Chen et al. 2015a), this temporal asymmetry has only briefly been mentioned before by Izumo (2005) and Ishida et al. (2008). In (Izumo 2005), the authors note a low simultaneous correlation between the Ekman transports at 5°N and 5°S and relate this to the anomalous displacement of the intertropical convergence zone (ITCZ). In (Ishida et al. 2008), the authors highlight the temporal asymmetry between the NH and SH upper ocean meridional transports. They attribute the asymmetry to the NH WBC explaining that it lags the NH interior transport by several months while both transports are in phase (negative) in the SH.

In the present study, however, we distinguish between the surface and the subsurface interior transports. This separation allows us to identify that the WBC and the subsurface interior transports are anti-correlated in both hemispheres (not only in the SH). Moreover, we find that rather than the NH WBC lagging the NH interior transports, it is the NH surface branch which leads both the NH subsurface interior and NH WBC branches. This circumstance ascribes particular importance to the NH surface transport, turning out to be a crucial factor in impacting the meridional mass exchange between the tropics and subtropics. The surface branch asymmetry is a consequence of the anti-cyclonic wind stress pattern over the Northwest tropical Pacific ($ENSO_{NONLIN}$). The fact that the timing of the $ENSO_{NONLIN}$ wind stress evolution is out of phase with the $ENSO_{LIN}$ wind stresses eventually results in the NH leading the SH surface branch by 8 months. Combined with the in-phase relationship of the subsurface and WBC branches the total STC time lag is 3 months.

The time lag between NH and SH STCs leads to both cells playing different roles during the evolution of ENSO events. In this regard, the $ENSO_{NONLIN}$ winds critically influence the temporal evolution of the NH STC. This influence is reflected by a shift of the peak anomalous NH STC changes to 3 months earlier than when forced by the zonal wind stresses only. Since the SH STC is mainly forced by the $ENSO_{LIN}$ wind stresses, this means that the NH STC is strongest (weakest) prior to the SH STC during El Niño (La Niña) events, which might attribute predictive skill to the NH STC. On a similar note, Widlansky et al. (2014) suggested predictive skill emerging from the tropical North Pacific anti-cyclone inducing prolonged low sea levels after strong El Niño events. Further to this, based on the differing evolution of the STCs in each hemisphere combined with each hemisphere‘s differing mean state, temperatures could act to modulate the temporal evolution of ENSO events and play a role in the apparent event seasonal synchronisation.

During the recent (multi-)decadal period, the SH STC appears to have played the most prominent role in the observed change of the tropical Pacific background state as the STC at 5°S increases at double the rate compared to 5°N. The reduced variability at 5°N relative to 5°S is not found to be due to reduced forcing, but is related to the enhanced vertical interference which appears to be induced by the high eddy activity that is present across the basin at this latitude (Chen et al. 2015b; Holmes et al. 2018). It is interesting to note that a similar hemispheric difference is found when the STCs are defined at 9° latitude, although the underlying physics are thought to be quite distinct from those occurring at 5° latitude, as this indicates the asymmetry is not sensitive to the latitude of the STC definition.

While it is currently unclear if this asymmetry would be apparent during past decadal changes, our results are in line with Luo and Yamagata (2001) who also ascribed a major role to the SH. Their mechanism is based on an atmospheric teleconnection from the Eastern equatorial Pacific to the subtropics and the subsequent advection of temperature anomalies back to the equator ($\overline{v}$T$'$). This is fundamentally different to the mechanism in the present study which is based on the varying overturning rate of the STCs (v$'\overline{T}$). We still need to better understand if the STC changes identified here influence the actual properties of the water upwelled in the equatorial region. However, as described in section 2.4, it appears that the major portion of pycnocline water that is transported towards the equator across 5° latitude actually originates from the subtropics and has the potential to modify the properties of the upwelled water.

Our results show that the (multi-)decadal variability of the STC transport in either hemisphere is not driven by ENSO-related winds. The long-term trends in the volume transport of the STCs cannot be reproduced by our targeted ENSO experiments. Therefore, we can exclude this mechanism to be responsible for changes in the background state of the tropical Pacific Ocean, consistent with England et al. (2014). In contrast to earlier studies (McCreary Jr and Lu 1994; Farneti et al. 2014b), the observed wind forcing utilised in EXP_{FULL} and its decomposition for the other three experiments does not have clear distinctions between tropical and subtropical regions. However, in terms of the wind decomposition carried out, the $ENSO_{NONLIN}$ experiment winds (Figure 2.2b) clearly has the strongest wind signature in the subtropical Northern hemisphere region. We find that while these winds drive STC interannual variability, they do not seem to play a role in driving the observed decadal STC changes.

Interestingly, the WBC in each hemisphere does not display a decadal trend during the 1993-2011 period. This is in contrast to analysis that was done for a similar period at 9° latitude, where the WBC and subsurface interior flow clearly oppose each other (e.g., Lee and Fukumori 2003; Lee and McPhaden 2008). We have repeated our analysis at 9° latitude and our results are consistent with the above mentioned studies, i.e. the decadal trends of the WBC and subsurface interior transport anomalies are counteracting each other. The reason for the missing trends of the WBC at 5° latitude can be attributed to the strong anomalies in the years 1995/96 which are much weaker at 9° latitude (Figure 2.14). This implies that the interannually varying level of compensation between the WBC and the subsurface interior transports strongly affects the level of compensation on decadal time scales. The varying level of compensation between boundary and interior transports is thought to be

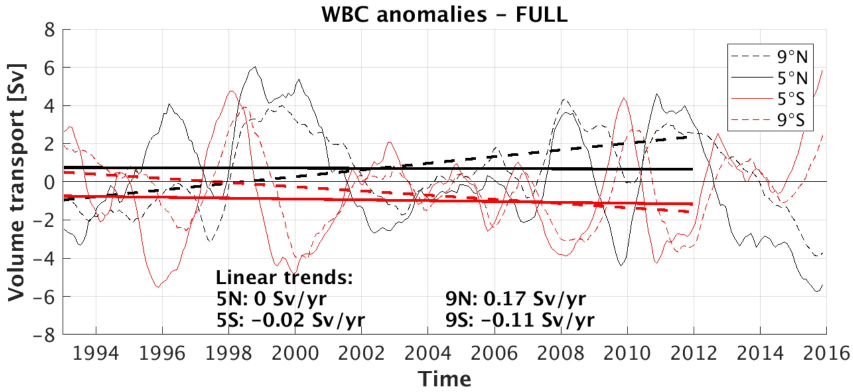

Figure 2.14: WBC transport anomalies and linear trends for the period 1993-2011 in EXP_{FULL}. Solid black (red) lines indicate transport at 5°N (5°S), dashed black (red) lines indicate transport at 9°N (9°S). Positive means northward transport. The WBC trends at 5°N and 5°S are insignificant at the 90% confidence level.

very important for the tropical Pacific Ocean heat budget (Hazeleger et al. 2004).

Relating our results back to McPhaden and Zhang (2004), we find the same asymmetry of decadal STC trends at 9° latitude which is consistent with their study and can be inferred from their Figure 3a. We find that the reason for the reduced STC trend at 9°N is largely related to the reduced increase of the Ekman driven surface branch (66% weaker, subsurface branch 22% weaker, Figure 2.11b). However, an additional component of the NH STC trend weakening originates from a stronger WBC at 9°N which poses a greater compensation to the subsurface interior transport (49%) compared to 9°S (32%). The intention here is to point out the hemispheric difference in decadal STC trends and the potential impact of this difference on the tropical decadal variability rather than providing a physical explanation of the reduced trend in the Northern hemisphere. Hence, the proposed explanations are not meant to be definite but are rather a suggestion of possible causes for the difference in trends that have to be examined further in a future study.

Despite the SSH pattern of the tropical Pacific being closely related to the subsurface STC transport on interannual time scales (SSH leading by 2 months), this relationship appears to break down at longer time scales, in particular at 5°N. Thus, our results raise questions over the use of sea level measurements to monitor the decadal variability of the interior subsurface transport which is an integral part of the STCs (e.g., Feng et al. 2010). Given that the actual NH STC trend (Figure 2.11) is only half of that expected via calculation with the SSH gradients (cf Figure 2.12b), our results suggest that caution should be placed in interpreting decadal STC changes derived from SSH. This in turn might lead to false conclusions on the amount of upwelled water at the equator and the associated SST and air-sea heat flux anomalies which determine the tropical Pacific climate.

We understand that the definition of the branches may introduce some uncertainty here. As can be seen from Figure 2.4b the distinction between the mean surface and subsurface interior branches at 5°N seems to be not very clear. This is also represented in the high regression coefficient between the subsurface branch and the Ekman transport (0.31). However, we have tested various definitions of the STC branches. Separating the surface and subsurface interior transports by an isopycnal surface instead of a constant depth level, did not change the main results of this study. We have also tested numerous different definitions of the WBC, in particular at 5°N, some of which also include the re-circulations and offshore branches. These definitions were based on various methodologies in order to find the longitude that best separates the WBC from the interior flow. Based on the correlation analysis as described in section 2.4, defining the WBC width by correlation with the core WBC transport is clearly physically meaningful. Thus, we believe that our definition of the STC branches provides a solid foundation for our analysis.

Previous studies have shown that spiciness anomalies that are generated in the subtropics and are largely transported with the STC branches have the potential to reach the equatorial Pacific where they can impact the heat exchange with the atmosphere (Schneider 2000, 2004). Even though the decadal trend of the STC at 5°N is small large amounts of water are transported towards the equator. Given the strong spiciness gradients found in each hemisphere, an open question is how the transport of spiciness anomalies of the NH and SH STC impacts the tropical climate. This will be the focus of future work.

Chapter 3

Subtropical to Tropical Pathways of Pacific Ocean Spiciness

This Chapter has been submitted for publication as:

Zeller, M., McGregor, S., Capotondi, A., and van Sebille, E., 'Subtropical to tropical pathways of ocean spiciness', *Climate Dynamics*

Preface

Understanding mechanisms of tropical Pacific decadal variability is of high importance for differentiating between natural climate variability and human induced climate change in a region that sets the framework for the El Niño - Southern Oscillation. Here, we investigate the advection of density compensated temperature anomalies ("spiciness mechanism") as a potential contributor to tropical Pacific decadal variability. We use an ocean general circulation model along with a Lagrangian tracer simulator to backtrack spiciness anomalies from the equatorial region. Consistent with observations, we find the primary source regions of spiciness generation to be in the eastern subtropics of each hemisphere. Our results indicate that 75% of the equatorial subsurface water originates in the subtropics, of which two thirds come from the Southern Hemisphere. We further show that for a warm spiciness peak at the equator, ~90% of the spiciness anomalies are sourced from the Southern Hemisphere. As opposed to previous studies, our results suggest that the majority of these warm spiciness anomalies travel via the interior pathway and a much smaller fraction travels via the western boundary current (WBC). The relative importance of the pathways changes when following cool spiciness anomalies. Here, the major contributor to the cool peak at the equator is the Northern hemisphere (NH) WBC (48%), followed by smaller contributions by the Southern hemisphere (SH) WBC and SH interior. A possible explanation for this varying relative importance of the pathways is hemispheric differences in the mean spiciness distribution in the Pacific basin. The NH mean pycnocline temperatures are up to 4°C cooler than the corresponding SH temperatures. Consequently, the relative contributions of NH versus SH pathways may affect the spiciness signal emerging at the equator. Our results do support this explanation.

3.1 Introduction

In recent decades, a lot of effort has been put into the understanding of the Pacific Decadal Oscillation (PDO) which has its dominant expression in the extratropical North Pacific. A summary of the findings and the current state of knowledge is provided by Newman et al. (2016). The PDO along with its often recognised Pacific-wide sea surface temperature (SST) manifestation, the Interdecadal Pacific Oscillation (IPO), both display a clear decadal SST signal in the tropical Pacific. However, the origin of this tropical SST signal remains unclear. Despite this, these decadal SST changes in the tropical Pacific have been found to be of great importance for various reasons. Setting the framework of the El Niño - Southern Oscillation (ENSO), low-frequency changes in the tropical Pacific have been associated with changes in the frequency, intensity (Zhao et al. 2016), flavour (Freund et al. 2019), and predictability (Neske and McGregor 2018) of ENSO events. Moreover, the recent negative phase of the IPO was shown to explain a large portion of the pause in global surface warming at the beginning of the 21^{st} century (Kosaka and Xie 2013; England et al. 2014). Considering the unique impact of the tropical Pacific on the global climate, a better understanding of the drivers of the tropical Pacific decadal variability would be of great scientific and societal value. Various theories exist that aim to identify the drivers that generate tropical Pacific decadal variability. These drivers can broadly be separated into two main categories: i) local drivers that reside in the tropical Pacific and ii) remote drivers that impact the tropics via teleconnections.

Local drivers are largely related to the occurrence of ENSO. Vimont (2005) suggests that simple averages over ENSO cycles along with a changing ratio of El Niño versus La Niña events over time imprints on the decadal signal in the tropical Pacific. Another explanation is given by Rodgers et al. (2004) who argue that the dynamical nonlinearities associated with ENSO lead to a "rectification" of the interannual ENSO variations into the mean state.

In terms of remote drivers, various studies have focused on atmospheric dynamics attributing tropical Pacific decadal variability to subtropical-tropical interactions via changes in strength of the Hadley circulation (Barnett et al. 1999; Di Lorenzo et al. 2015) and inter-basin teleconnections via changes in the zonal Walker circulation (McGregor et al. 2014b; Chikamoto et al. 2016).

In the ocean, the Pacific subtropical cells (STCs) are the oceanic counterpart to the atmospheric Hadley cells connecting the subtropics with the equator (McCreary Jr and Lu 1994; Liu et al. 1994; Lee and Fukumori 2003; Schott et al. 2004; Capotondi et al. 2005). As the STCs regulate the supply of cold subsurface water to the equator, they have been associated with decadal changes in the tropical Pacific through several different mechanisms. Kleeman et al. (1999) proposed that long-term variations in the STC strength have the potential to modulate the tropical Pacific climate through changes in the rate of equatorial upwelling. In a recent study, Zeller et al. (2019) suggested that this mechanism is specifically contributed to by the changes in the Southern hemisphere STC strength. The consequential hemispheric asymmetry of STC transports may critically modulate this mechanism given the difference in mean subsurface ocean temperature between the Northern and Southern hemispheric extratropics. An alternative mechanism is based on the advection of temperature anomalies from the mid-latitudes to the tropics with the mean STC circulation (Gu and Philander 1997; Giese et al. 2002; Zhang et al. 1998). This mechanism is negligible as temperature anomalies subducted in the central North Pacific, where the decadal signal is strongest, have been shown to decay before reaching the equator (Schneider et al. 1999a,b; Hazeleger et al. 2001b). The relative importance of each of the above mentioned mechanisms to produce the full decadal signal is still unknown.

Schneider (2000) proposed a third mechanism to drive tropical Pacific decadal variability which involves the spiciness of the ocean. Ocean spiciness has been defined by Munk (1981) as density compensated anomalies of temperature and salinity. On a layer of constant density, hot and salty water is defined as being more spicy than cool and fresh water. Density compensated temperature (spiciness) anomalies are fundamentally different from thermal anomalies generated by subduction as the ones analysed by Gu and Philander (1997) and Schneider et al. (1999a).

Subducted thermal anomalies modify the vertical density structure of the ocean by uplifting/suppressing the mean thermocline and are of diabatic origin. Spiciness anomalies, on the other hand, are density-compensated and do therefore not affect the density profile. They behave like passive tracers and propagate with the mean circulation along isopycnal surfaces without significant dissipation.

Spiciness can be generated by two distinct mechanisms. i) Through anomalous advection across mean temperature gradients as explained by Schneider (2000). In this case, anomalous winds and wind stress curl force anomalous ocean currents which shift temperature gradients on isopycnals away from their mean position. This shift causes temperature anomalies on isopycnals, hence spiciness anomalies. ii) Through convective mixing at the base of the surface mixed layer, as explained by Yeager and Large (2007). The generation occurs predominantly during winter when stratification is weak in the subtropical and mid-latitude regions where unstable vertical salinity gradients prevail. These conditions allow for enhanced vertical mixing which causes a sharp gradient of both temperature and salinity at the base of the mixed layer. Through the penetrative mixing at the base of the convective boundary layer a shallow layer of strongly density compensated water with various combinations of temperature and salinity properties is formed between the mixed layer above and the permanent pycnocline below. This layer is the region where spiciness anomalies are generated and from where they are advected away by the mean circulation.

Observations substantiate the existence of spiciness anomalies in the mid-latitudes of all ocean basins (Yeager and Large 2007) as well as in the tropical Pacific Ocean (Li et al. 2012). The model study by Schneider (2000) suggests the existence of a decadal mode of coupled ocean-atmosphere dynamics based on the oceanic advection of spiciness anomalies from the subtropics to the equator. Upon reaching the equator, these spiciness anomalies are upwelled to the surface where they create equatorial sea surface temperature anomalies which in turn produce a fast atmospheric response responsible for changing the sign of the subtropical spiciness anomalies and reversing the phase of the cycle.

However, it is still unclear if spiciness anomalies can persist from the source region to the Eastern equatorial Pacific where they potentially upwell and interact with the atmosphere. Another contentious question is whether spiciness anomalies travel to the tropical Pacific via the Western boundary as suggested by Schneider (2000), Giese et al. (2002), and Yeager and Large (2004) or if they propagate through the interior ocean as suggested by Li et al. (2012) and Thomas and Fedorov (2017). In the present study, we aim to shed light on the pathway of the subtropical to tropical exchange and the potential contribution of the "spiciness mechanism" to tropical Pacific decadal variability using a high resolution ocean general circulation model (OGCM) along with a Lagrangian particle simulator.

The paper is structured as follows: section 2 details the OGCM and the Lagrangian tracer model as well as the Lagrangian tracer experiments that have been carried out. Section 3 describes the occurrence and pathways of spiciness anomalies. A discussion and conclusions are provided in section 4.

3.2 Model and Methods

3.2.1 The Ocean Model

We use a global coupled ocean sea-ice model (GFDL-MOM025) which is based on the GFDL CM2.5 coupled climate model (Delworth et al. 2012) and is coupled to the GFDL Sea Ice Simulator model. The GFDL-MOM025 model has a 1/4° Mercator horizontal resolution globally and 50 vertical levels. The vertical level thicknesses range from 10 m at the surface to about 200 m at depth. Sea surface salinity is restored to a seasonally varying climatology on a 60 day time scale. To reach equilibrium, the model is forced with the ERA-interim climatology of heat, freshwater and momentum fluxes in a 40 year spin-up control simulation. The OGCM resolves mesoscale variability in the tropics and subtropics and the use of 5-day average output enables us to reliably include the spatially complex transport of tracers by mesoscale eddies.

After reaching equilibrium, the ocean model is forced with climatological heat and freshwater fluxes and a fully varying wind field derived from the ECMWF ERA-interim reanalysis product (Dee and Uppala 2009) that extends from January 1979 to May 2016. The ERA-interim winds were selected to overcome the strong trend biases in wind stress and wind stress curl over the tropical Pacific that are known to be present in the NCEP/NCAR (National Centers for Environmental Prediction/National Center for Atmospheric Research) wind product (McGregor et al. 2012a). While this choice moved us away from the more balanced fluxes of CORE (Coordinated Ocean-ice Reference Experiments) forcing (Large and Yeager 2009), the more realistic wind stress forcing appears to be more appropriate to address the proposed research questions.

3.2.2 Decadal Spiciness Variability

Here, we define spiciness as temperature on isopycnal surfaces. This is equivalent to choosing salinity on the same surfaces, as by definition they show the same behaviour. The mean spiciness distribution is characterised by two zonal lobes of spiciness maxima, one in each hemisphere, stretching from the west to the east. The SH lobe is clearly warmer than the NH lobe with SH temperatures reaching up to 25°C compared to 21°C in the NH. The mean spiciness structure agrees well with Argo observations (Figure 3.1a). Based on Argo floats, Yeager and Large (2007) and Li et al. (2012) identified the subtropical Northeastern and Southeastern Pacific as prominent regions for the generation of strong spiciness anomalies during winter. Consistent with these observations, we find the strongest variance of modelled spiciness in the Northeastern and Southeastern subtropical Pacific (Figure S3.1).

We focus on the spiciness anomalies in the eastern/central equatorial Pacific where spiciness anomalies are meant to upwell after their advection from the subtropics. Averaging over the equatorial region (EQbox, 160°E-100°W, 2°S-2°N, Figure 3.1a)

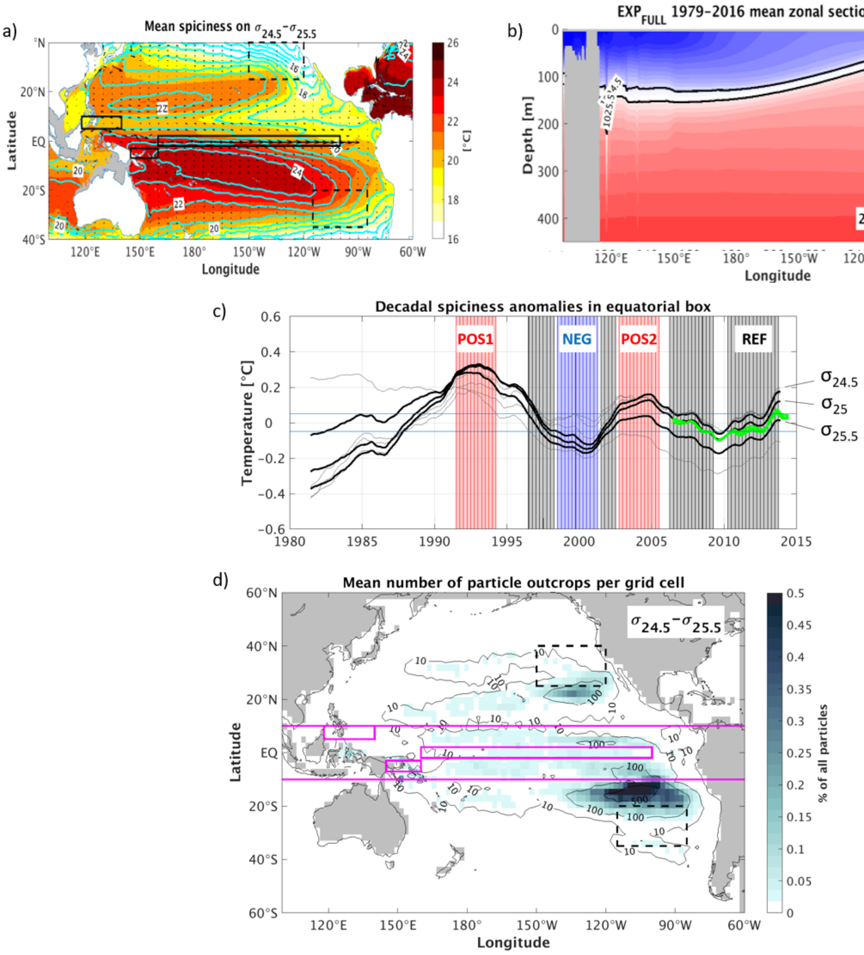

Figure 3.1: **a**) GFDL-MOM025 mean spiciness averaged over the $\sigma_{24.5}$, σ_{25}, and $\sigma_{25.5}$ surfaces. Cyan contours with white labels show Argo observations. The dashed boxes indicate the observed source regions of spiciness anomalies. The solid boxes at the western boundary are used to distinguish WBC pathways from interior pathways. The solid box along the equator indicates the region where spiciness anomalies emerge after they are advected from their source region. **b**) Mean density section across equatorial Pacific. The $\sigma_{24.5}$ and $\sigma_{25.5}$ isopycnals are highlighted. **c**) Evolution of spiciness anomalies averaged over the equatorial box on different isopycnal surfaces ranging from σ_{23} to σ_{26}. The isopycnal layers $\sigma_{24.5}$ to $\sigma_{25.5}$ are highlighted as they show the strongest decadal variability. The green lines show Argo observations. A 5-year moving average has been applied to highlight low frequency changes. Overlying red, blue, and grey boxes/lines indicate the particle release periods/dates for the warm, cool, and neutral experiments, respectively. **d**) Percentage of particle outcrops (particles crossing MLD) averaged over all experiments for all released particles. Contours indicate the number of outcropped particles.

we find the strongest decadal spiciness signal to emerge on the σ_{24} to $\sigma_{25.5}$ isopycnal surfaces (Figure 3.1c). This is also the range of isopycnals that Schneider (2000) found to exhibit the strongest decadal changes in spiciness. Further to this, spiciness anomalies on the σ_{24} isopycnal surface do not propagate outside the tropics as they are largely confined to the surface and are thus strongly affected by the seasonal outcropping of isopycnals (not shown). We therefore restrict our analysis to the $\sigma_{24.5}$, σ_{25}, and $\sigma_{25.5}$ isopycnal surfaces. Figure 3.1b shows the mean density structure in a vertical zonal section through the equatorial Pacific averaged between 2°S and 2°N. The $\sigma_{24.5}$ and $\sigma_{25.5}$ isopycnals are highlighted and illustrate a shallowing from west (>100m) to east (<50m). We identify two warm peaks (POS1, POS2) with anomalous isopycnal layer temperatures of up to +0.33°C and +0.16°C, respectively, and one cool peak (NEG) with anomalous temperatures of down to -0.17°C. In the following, we are seeking to identify the source regions of the contributing spiciness anomalies by backtracking particles from the equatorial region.

3.2.3 The Lagrangian Particle Simulator

To follow the potential pathways of the spiciness anomalies through the ocean we make use of the OceanParcels Lagrangian particle simulator (Lange and Sebille 2017). Using a fourth order Runge-Kutta time integration OceanParcels allows us to simulate the trajectories of virtual particles through space and time. As by definition spiciness anomalies can only travel along isopycnal surfaces, we convert the 5-day average ocean model output (horizontal velocities, temperature, salinity) from Cartesian coordinates to density coordinates by linear interpolation onto predefined density surfaces. Particles are therefore tracked on 2-D isopycnal surfaces. The tracer simulations are computed off-line and use the ocean model 5-day average horizontal velocities. We also sample the hydrographic field along the particle trajectories which enables us to readily monitor the evolution of temperature, salinity and depth of each particle.

3.2.4 The Tracer Experiments

Particle sets, which behave like passive tracers akin to spiciness anomalies, are released in the EQbox region on the isopycnal surfaces exhibiting the strongest decadal spiciness signal ($\sigma_{24.5}$, σ_{25} , $\sigma_{25.5}$). For each decadal peak of spiciness anomalies (POS1, POS2, NEG) particle sets are released at 3-month increments providing 12 different release dates. This procedure increases the number of particles tracked and also ensures that the particle trajectories are independent of the exact release date. We find this to be a reasonable trade-off between the number of particles released and computational efficiency. For comparison, a reference particle set (REF) is released at 41 release dates in between the identified decadal spiciness peaks. The REF release dates were distributed across the entire time period to ensure independence between release dates and thus increase the number of degrees of freedom when calculating the significance of the changes in the other experiments. For all experiments, each particle set is tracked backward in time for 10 years on daily time steps. Particle positions, spiciness and other properties are saved every month. As spiciness anomalies lose their characteristic as a passive tracer once they are upwelled into the mixed layer and come into contact with the atmosphere, in the following we consider only those particles which have not yet crossed the temporally and spatially varying mixed layer depth (MLD) as they are advected backward in time. The MLD is an output variable of the OGCM and is determined by density criteria. To account for the effect of subgrid-scale advection through baroclinic eddies, we apply horizontal Brownian diffusion to the advection scheme. According to Okubo (1971), diffusivities of 10-100 $\frac{m^2}{s}$ are representative for turbulent diffusion at spatial scales of 10-100 km, respectively. In consideration of our model resolution with a grid cell length of ∼25 km, we choose a default diffusivity of 10 $\frac{m^2}{s}$. In a more recent estimate, Ruehs et al. (2018) suggests a diffusivity of about 300 $\frac{m^2}{s}$ for the same length scale. We, therefore, test the sensitivity of our results to the chosen value of diffusivity (see section 3.3) and the results appear to be insensitive to this choice.

3.3 Results

3.3.1 Subtropical-Tropical Water Pathways

As a first step we focus on the pathways of water parcels propagating between the subtropics and the tropics. To this end, we apply the condition that particles originating in the equatorial region have to cross 10° latitude at some point during their trajectory, while all other particles are disregarded. We also distinguish between four pathways for the advection of particles from the subtropics to the equator: the Western boundary and the interior pathway in both the Northern and Southern hemisphere. To be classified as a NH (SH) western boundary pathway, particles have to cross the NH (SH) WBC box (cf. Figure 3.1 d) and 10°N (10°S). Particles that cross 10° latitude outside of the respective WBC box are classified as travelling on the interior pathway.

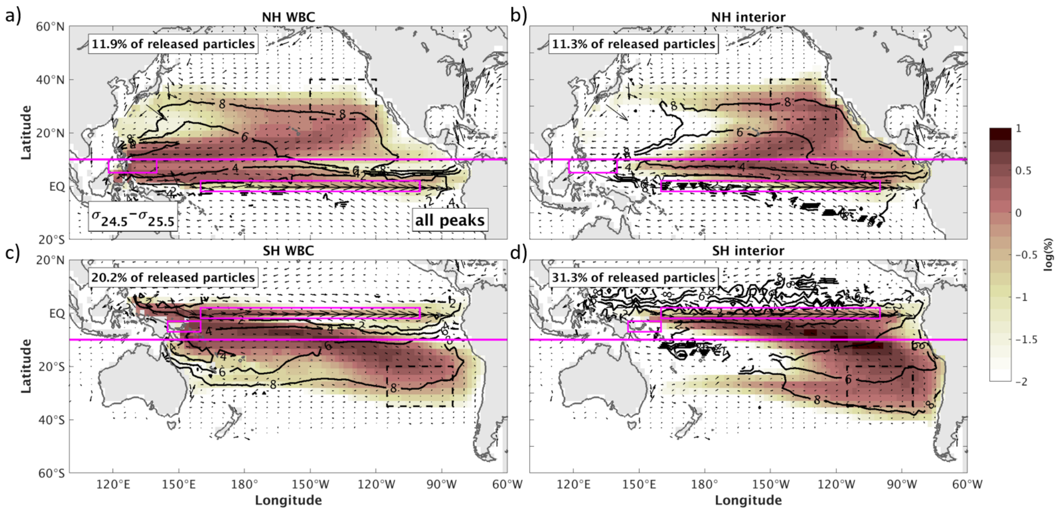

Figure 3.2: Tracer pathways on top of $\sigma_{24.5-25.5}$ (all four experiments combined) along the different pathways: **a**) NH WBC, **b**) NH interior, **c**) SH WBC, **d**) SH interior. The boxes are the same as in Figure 1a. The shading indicates the particle density (percentage of particles that cross grid cell) to identify the pathways, with the colour scale being logarithmic, i.e. 1=10%, 0=1%, -1=0.1%. Overlying arrows show the time mean ocean current velocities averaged over the respective isopycnal surfaces. Black contours indicate the median travel time of particles in years. The relative contribution of each pathway is indicated as a percentage with respect to all particles crossing 10° latitude in the upper left corner of each panel.

The examination of the pathways reveals that there are no major differences in the particle density distribution between the four experiments (cf. Figures S3.2-S3.5) which corroborates our assumption that the particles are advected with the mean circulation. It is therefore legitimate to consider the composite of all experiments for this case. In our time frame of 10 years, 75% of all particles arriving at the equator have their origin in the subtropics (Figure 3.2, Table 3.1) while the remaining 25% come from within the tropics. Half of all particles enter the tropics from the SH while a quarter enters from the NH. This preference for the SH pathways is consistent with the existence of the potential vorticity barrier between 10-15°N which inhibits the exchange of water from the subtropics to the tropics through the interior (Lu and McCreary Jr 1995). The SH exchange displays a clear preference for particles to enter the equatorial region via the interior pathway (with the interior transports typically being 50% larger than the WBC transports), while both pathways are generally of equal prominence in the NH.

On average, water parcels take about 4 years to propagate from the eastern subtropical Pacific to the EQbox region via the interior pathway, and about 6 years when they propagate via the WBC (Figure 3.2). The 25^{th} and 75^{th} percentiles of the particle propagation time deviate from the median by about 1-1.5 years. These reported propagation times are in line with previous findings (Schneider 2000).

3.3.2 Advection of Spiciness Anomalies

We now consider the spiciness (temperature) anomalies that these water parcels carry to assess and quantify the relative importance of the four pathways and their impact on the EQbox decadal spiciness anomalies. To this end, particles are only tracked as long as they maintain a temperature anomaly above 0.1°C for the warm peaks and below -0.1°C for the cool peak. We consider this threshold to be reasonably small to include as many spiciness anomalies as possible but still large enough to have an impact on the equatorial Pacific temperature budget. Going forward in time, this is equivalent to removing the particle's trajectory before the associated spiciness anomaly is generated. Applying this additional condition affects the relative importance of the resulting pathways differently for the different experiments. Therefore, investigating the composite of all experiments is not legitimate in this case.

Table 3.1: Percentage of particles following each pathway (**and maintaining their temperature anomaly**) for each experiment and the average over all experiment (AVG). Note that the bold numbers in AVG do not take into account the values of REF when taking the average.

	NH WBC	SH WBC	NH interior	SH interior	SUM
POS1	10.9 (**1.5**)	23.2 (**6.4**)	6.5 (**1.1**)	30.5 (**16.6**)	71.1 (**25.6**)
POS2	11 (**0.1**)	21.5 (**2.2**)	11.6 (**0**)	30.3 (**1.3**)	74.4 (**3.6**)
NEG	14.8 (**5.3**)	18.3 (**2.6**)	11.4 (**0.2**)	30.7 (**3**)	75.2 (**11.1**)
REF	10.8 (**0**)	18 (**0**)	15.7 (**0**)	33.7 (**0**)	78.2 (**0**)
AVG	11.9 (**2.3**)	20.2 (**3.7**)	11.3 (**0.4**)	31.3 (**7**)	74.7 (**13.4**)

3.3.2.1 Positive spiciness anomalies

Table 3.1 reveals that POS1 is clearly the most efficacious experiment when it comes to the advection of spiciness anomalies. More than 25% of all particles released in POS1 maintain their spiciness anomaly and are sourced from outside the tropics. This is equivalent to more than one third of all particles that are sourced from outside the tropics maintaining their spiciness anomaly. In POS1, it is evident that the SH plays a much more important role in carrying subtropical spiciness anomalies to the EQbox region than the NH (Figure 3.3). The combined percentage of particles carrying spiciness anomalies from the NH subtropics to the tropics is 2.6%, which is roughly 10% of the magnitude of the SH (Table 3.1). The overall dominant pathway is the SH interior which accounts for to 16.6% of all particles released, more than half of the particles following the SH interior pathway, and two thirds of all particles which maintain their spiciness anomaly.

The temporal evolution of the POS1 spiciness anomalies from their source region to the equator exhibits a gradual decrease along the interior pathways from about 0.8°C to about 0.4°C, and a rather constant value of about 0.4°C along the NH and SH WBC (Figure 3.4, thick red line). The evolution indicates that particles are

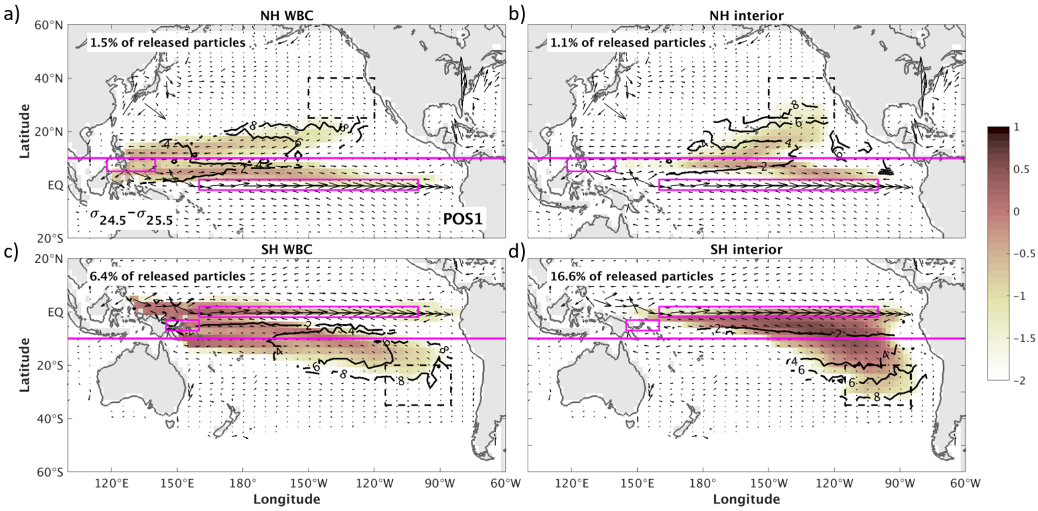

Figure 3.3: Same as Figure 3.2 but with the additional condition that spiciness anomalies of each tracer must not fall below 0.1°C. Shown is the POS1 experiment. Black contours indicate the median travel time of particles in years.

more prone to lose their spiciness anomaly when they travel along the interior while particles largely preserve their spiciness anomaly along the WBC pathway. The explanation is given by the spatial distribution of the temperature anomalies along each pathway (Figure S3.7). The distribution shows that for the interior pathways subtropical spiciness anomalies are rather generated within the region of strongest spiciness variability, i.e. spiciness anomalies have a comparatively high magnitude. Spiciness anomalies following the WBC pathway, on the other hand, tend to be generated outside the main area of strongest spiciness variance and therefore are smaller from the start (cf. Figure 3.4 and Figure S3.7). The thin lines in Figure 3.4 show the temperature anomaly averaged over all particles. Comparing the thin to the thick line reveals that the subtropical spiciness anomalies have a large effect on the total spiciness anomaly in POS1.

Along with the evolution of averaged spiciness anomalies, the evolution of the number of particles maintaining spiciness anomalies also has to be considered (Figure 3.5). In the Northern hemisphere, we see a gradual increase in the number of particles, however, the total numbers are very small and their effect may be negligible. In fact, the amount of particles is either still below or has just reached the 1%

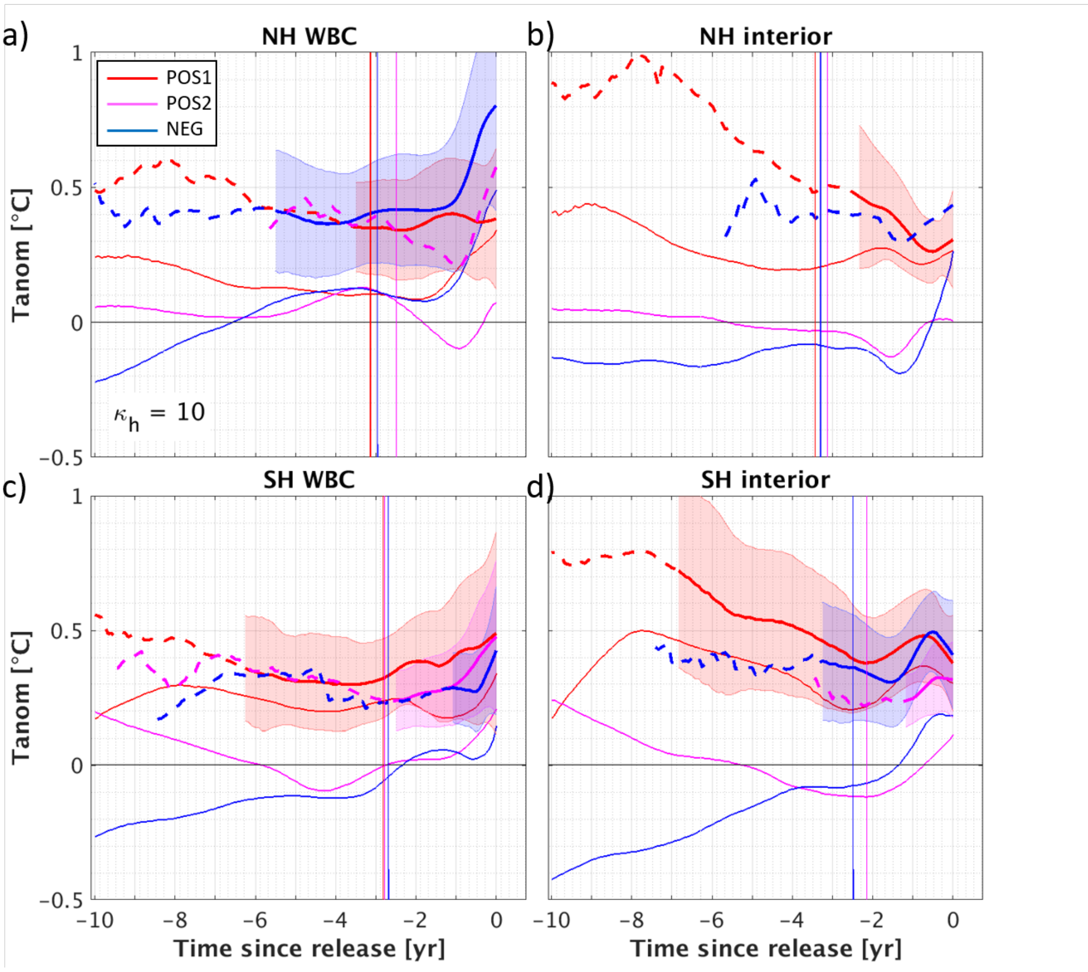

Figure 3.4: Temporal evolution of spiciness anomalies along the different pathways: **a**) NH WBC, **b**) NH interior, **c**) SH WBC, **d**) SH interior. The thick lines show the temperature anomaly averaged over all particles which maintain their spiciness anomaly for each pathway. The thin lines show the temperature anomaly averaged over all particles for each pathway. Note that NEG anomalies have been multiplied by -1. Thick lines become dashed when less than 1% of particles relative to all particles released are left. The shading represents the particle spread (std) at each time step. The vertical lines indicate the average time when particles have reached 10° latitude.

mark when they arrive at the tropics (vertical lines in Figure 3.5). In the Southern hemisphere, the number of particles maintaining spiciness anomalies rather gradually increases along the WBC pathway, indicating a constant generation of spiciness anomalies along the way. The number of particles for the SH interior pathway exhibits a remarkably strong increase between 1-3 years before arriving at the equator (Figure 3.5). This strong increase coincides with the time when particles are at the spiciness generation region in the Southeastern subtropics (cf. Figure 3.1d).

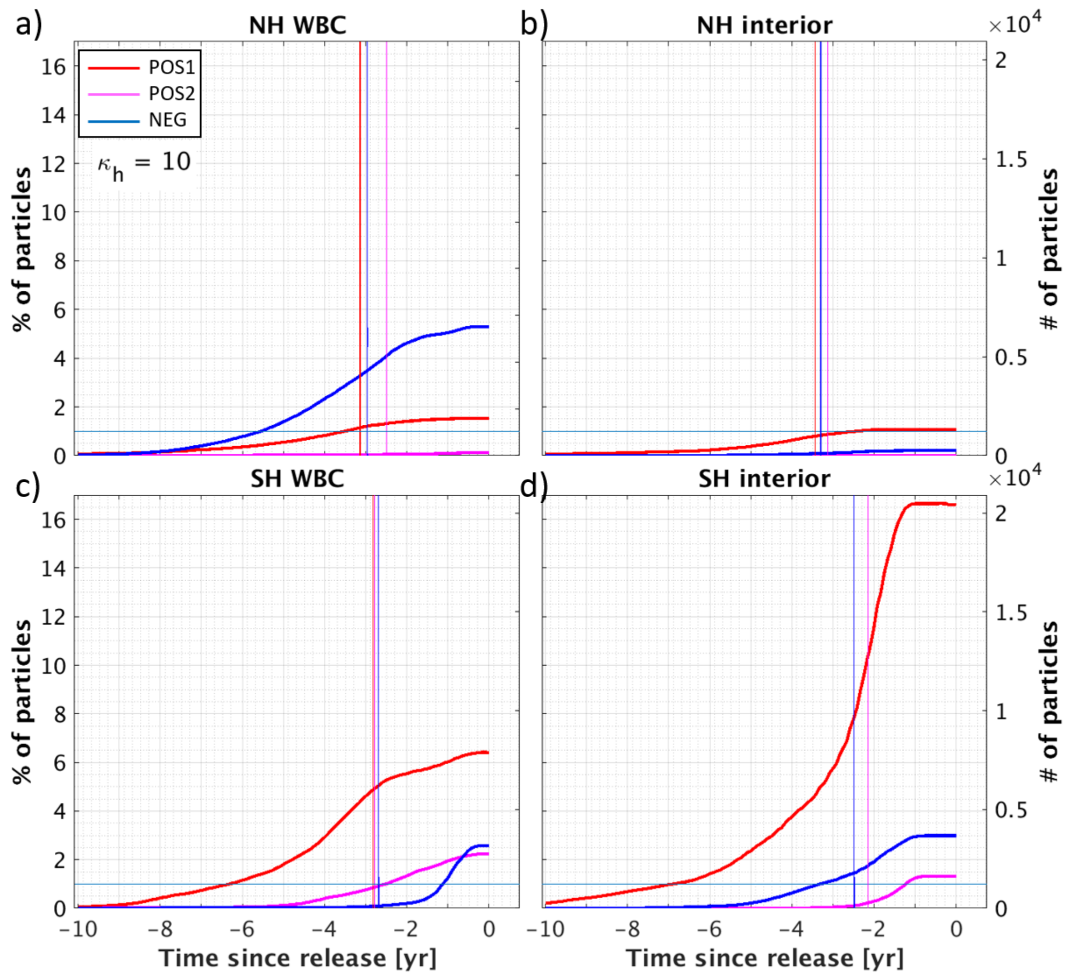

Figure 3.5: Temporal evolution of number of particles and percentage of all particles released along the different pathways: **a**) NH WBC, **b**) NH interior, **c**) SH WBC, **d**) SH interior. The horizontal line indicates the 1% mark. The vertical lines indicate the average time when particles have reached 10° latitude.

In POS2, only 3.6% of the particles carry their spiciness anomaly from the subtropics to the equator (Table 3.1). Roughly two thirds of these particles propagate via the SH WBC and one third via the SH interior (Figure S3.6). However, given the low percentage their contribution to the equatorial heat budget is negligible as can be inferred from comparing the thin with the thick magenta line in Figure 3.4. This comparison shows that the subtropical spiciness anomalies (thick lines) have no effect on the total spiciness anomaly averaged over all particles (thin lines) which is mostly hovering around zero. The small impact of POS2 spiciness anomalies is also demonstrated by the fact that by the average time that the particles enter the tropics at 10° latitude the amount of particles is still less than 1% for all pathways (Figures 3.4 and 3.5, magenta line). The spatial distribution of the temperature anomalies along each pathway is depicted in Figure S3.8.

3.3.2.2 Negative spiciness anomalies

When particles carry a cool temperature anomaly, 11.1% maintain their anomaly from the subtropics to the equator (Figure 3.6). In total, half of the spiciness anomalies are sourced from the Northern hemisphere and the other half from the Southern hemisphere (Table 3.1). Interestingly, cool spiciness anomalies during this event preferably propagate along the NH WBC (5.3%) while the NH interior only carries a very small amount (0.2%). The SH contribution is partitioned into 3% via the SH interior and 2.6% via the SH WBC. In terms of the temporal evolution (Figure 3.4, blue line), the spiciness anomalies largely stay on a constant level, however, for the NH WBC pathway the temperature anomaly almost doubles from about 0.4°C to 0.8°C during the last year before arriving at the equator. The spatial distribution of the temperature anomalies along the pathways (Figure S3.9)

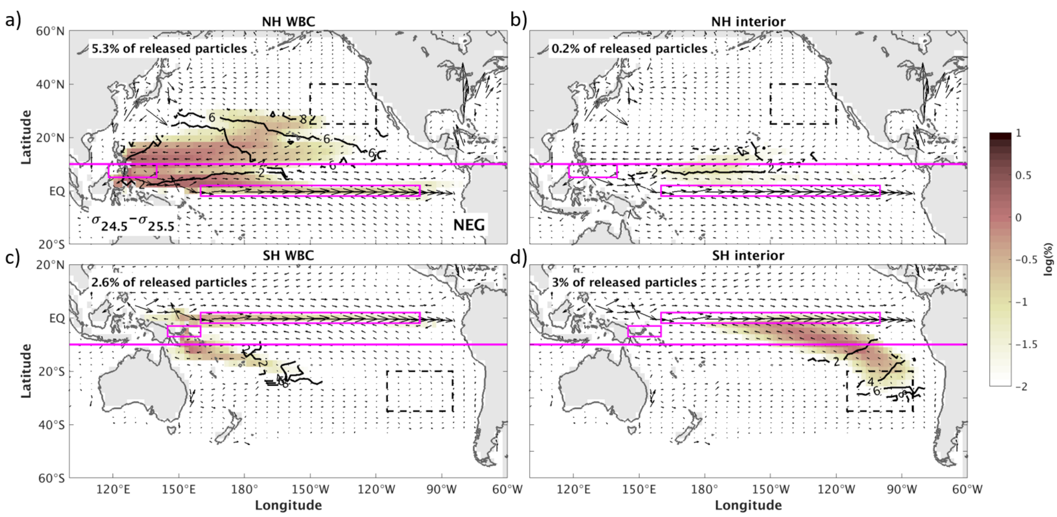

Figure 3.6: Same as Figure 3.3 but for NEG experiment.

reveals that the remotely generated spiciness anomalies grow as they pass the far west equatorial Pacific. This explains the rapid increase in the magnitude of the spiciness anomalies that follow the NH WBC pathway.

The number of spiciness anomalies increases gradually along the NH WBC pathway (Figure 3.5a, blue line) and along the SH interior pathway (Figure 3.5d). In contrast to POS1, there is no substantial rise along the SH interior pathway during years 1-3 before arriving at the equator (Figure 3.5d).

3.3.3 Sensitivity to horizontal diffusion coefficient

We have tested the sensitivity of the advection of particles to different diffusion coefficients (Table 3.2). The results indicate that with increasing diffusivity the percentages of the WBC pathways generally increase, except for the SH WBC pathway at a diffusivity of 1000 $\frac{m^2}{s}$. This relationship applies to both plain water parcels and spiciness anomalies. The increased percentages result from an increased spatial radius of probability for the location of each particle during the advection. This radius increases with a higher diffusion. As a consequence, at a higher rate of diffusion the probability that particles can cross 10° latitude increases. Interestingly, diffusion does not appear to impact the interior pathways given the negligibly small changes, except for the increase of the NH interior pathway at a diffusivity of 1000 $\frac{m^2}{s}$. This is thought to be related to the smaller spatial temperature gradients in the interior as compared to the western boundary which inhibits diffusion even at high diffusivity values.

While we do not have an explanation for the reduced percentage of the SH WBC pathway at a diffusivity of 1000 $\frac{m^2}{s}$, the sensitivity analysis shows that our results are not sensitive to the chosen value of diffusivity. As the percentages in our default case are somewhere in the mid of the range, we believe that κ=10 $\frac{m^2}{s}$ is a reasonable value for the diffusion coefficient.

Table 3.2: Percentage of particles following each pathway (and maintaining their temperature anomaly) for different horizontal diffusion coefficients κ [$\frac{m^2}{s}$].

POS1	NH WBC	SH WBC	NH interior	SH interior	SUM
κ = 0	7.7 (1.2)	17.5 (4.3)	6.5 (1.1)	30.4 (16.7)	62.1 (23.3)
κ = 10	10.9 (1.5)	23.2 (6.4)	6.5 (1.1)	30.5 (16.6)	71.1 (25.6)
κ = 100	12.1 (1.9)	25 (7.2)	6.6 (1.2)	30.2 (16.4)	73.9 (26.7)
κ = 1000	14.9 (2.6)	21.8 (5.6)	8.2 (2.2)	30.3 (16)	75.2 (26.4)

3.4 Discussion and Conclusions

The present study provides a quantitative assessment of the relative contribution of different pathways to the transport of water and spiciness anomalies from the Pacific subtropics to the equator. We find that approximately 50% of the water arriving at the equator is sourced from the SH subtropics, one quarter is sourced from the NH subtropics, and the remaining quarter has its origin within the tropics (defined here as 10°S-10°N). These results compare well with Blanke and Raynaud (1997) who also used backward Lagrangian simulations to quantify the origin of the EUC water. The results are also in very good agreement with the recent study by (Nie et al. 2019) who found a subtropical to tropical ratio of 4/1. In their study, the authors further determined that the subtropical contribution primarily stems from the North and South Eastern subtropical mode waters, while the tropical contribution arises from the equatorially confined tropical cells. Similar to (Nie et al. 2019), our results suggest an increasing contribution of the WBC (interior) water towards the western (eastern) equatorial undercurrent (Figure 3.2). Knowing the source regions of upper Pacific Ocean equatorial water emphasises the need of observations in the respective remote areas to better estimate the water properties which are advected to the equator. Information about the pathways further helps to better understand the mechanisms and predict the interannual to decadal climate of this region.

The most important outcome of this study is that spiciness anomalies can travel from the subtropics to the equator. We show this for two out of the three case studies where we backtrack spiciness anomalies from the equator at periods of equatorial spiciness peaks, namely POS1 and NEG. In both cases, we find a considerable impact of subtropical spiciness anomalies for the formation of equatorial spiciness peaks. The "spiciness mechanism" thus constitutes a valid instrument of inducing TPDV. In the case of the positive peak in equatorial temperature in the early 1990s (POS1), almost all of the subtropical spiciness anomalies originate from the Southern hemisphere and the large majority of the SH spiciness anomalies (72%) travel via the interior pathway. This is in disagreement with previous studies suggesting that temperature anomalies travel via the western boundary pathways Giese et al. (2002); Yeager and Large (2004), while it corroborates the studies that propose the interior pathway to be the more dominant Li et al. (2012); Thomas and Fedorov (2017). This result is important as it implies a shortened lead time for the predictability of equatorial spiciness peaks because interior pathways on average have a two year shorter transit time (4-6 years) than the WBC pathways (6-8 years). Assuming that spiciness anomalies make up a substantial portion of the equatorial SST variance, the shortened lead time also affects the predictability of the tropical Pacific climate as a whole.

Further, our results for POS1 show a decrease of temperature anomalies over time for the interior pathways and no change for the WBC pathways (Figure 3.4, red line). The reason for this is that spiciness anomalies propagating via the WBC pathways do not originate from further poleward than 20° latitude, whereas spiciness anomalies propagating via the interior pathways originate from as far poleward as 30° latitude (cf. Figure 3.3). Thus, early spiciness anomalies propagating via the interior pathway originate from the region with the strongest variance in spiciness (Figure S1) resulting in strong spiciness anomalies accordingly (Figure S7). Interestingly, once the POS1 spiciness anomalies arrive at the equator they tend to have similar magnitudes no matter which pathway they took.

It is interesting that in contrast to the positive peak in spiciness (POS1) which has its largest spiciness anomaly contribution from the SH interior, the negative spiciness peak (NEG) is primarily contributed to by spiciness anomalies following the NH WBC pathway (48%). As a consequence, the lead time for the potentially predictable cold equatorial spiciness signal is two years longer than that of POS1. It is unknown whether the hemispheric difference in spiciness contribution identified by POS1 and NEG is a symptom of some larger scale process.

A special case is given by POS2. In this case, the contribution of remotely generated spiciness anomalies is negligible while there still exists a warm spiciness peak at the equator. We propose that the signal is still remotely forced but not by the advection of spiciness anomalies, but by the changing proportion of NH versus SH advection of mean spiciness. Given the large differences in mean spiciness of up to 4°C between both hemispheres (Figure 3.1a), deviations from the normal transport proportion lead to the generation of spiciness anomalies at the equator once the water masses merge and join the EUC.

This consistency between the source hemisphere of the anomaly and the mean temperature of the hemisphere applies to all three case studies and can be inferred from the ratio of Northern versus Southern hemisphere pathways (Figure 3.7). The ratio is clearly smaller for the two warm spiciness events (POS1, POS2) compared to the reference experiment (REF), which suggests that an anomalously large portion of warm equatorial waters comes from the Southern hemisphere. Moreover, the POS1 and POS2 ratios are outside the distribution of ratios derived from 10,000 times randomly subsampling 12 out of the 41 release dates of the REF experiment, highlighting the significance of the difference of these ratios from the reference ratio (Figure 3.7). Conversely, for the cold spiciness event the NH versus SH ratio is greater than for the REF experiment, although within the range of possible ratios for REF conditions, indicating that more equatorial water than usual originates from the Northern hemisphere. As mentioned before, this explanation mainly applies to the POS2 spiciness event where there is almost no contribution from remotely generated spiciness anomalies. Conversely, POS1 and NEG both show clear contributions from subtropical spiciness anomalies, so the relevance of locally generated spiciness anomalies as described above remains unclear and is subject to more data in the future.

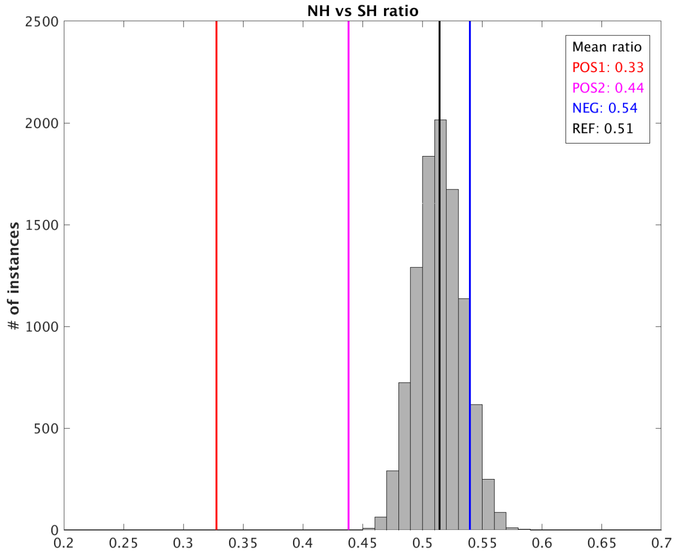

Figure 3.7: Ratio of NH versus SH contributions to equatorial water indicated as vertical lines for POS1 (red), POS2 (magenta), NEG (blue), and REF (black) experiments. The vertical lines indicate the mean ratio averaged over all release dates. The grey bars show the histogram of ratios derived from 10,000 random subsamples of 12 out of the 41 release dates for the REF experiment.

As we utilise climatological heat fluxes to force the ocean, the generation mechanism through convective mixing at the base of the surface mixed layer is likely poorly represented. Instead, the majority of spiciness anomalies will be generated through anomalous advection across mean temperature gradients as explained in section 1. It also has to be kept in mind that the length of the considered time period only allows us to investigate three decadal peaks. Therefore, we cannot claim statistical significance for the exact contributions of each pathway for the different experiments. It may be possible that the relative importance of the pathways will change for future peaks in equatorial spiciness.

In terms of the robustness of the results, the largest uncertainty arises from the potential impact of diapycnal diffusion which is not considered in this study. Diapycnal diffusion can have a considerable impact on the magnitude of spiciness anomalies over time as observed by (Johnson 2006), although their study only focuses on a single spiciness anomaly in the Southern hemisphere subtropics. An estimate of the uncertainty of the pathways is implicitly provided by the width of the pathways in the probability distribution maps in Figures 3.2, 3.3, and 3.6.

Finally, the main outcome of this study is the demonstration that for large temperature peaks at the equator the "spiciness mechanism" can act as an important contributor. Under consideration of the relative importance of the different pathways, spiciness anomalies are able to be advected from the subtropics to the tropics while preserving a considerable fraction of their anomaly. Under the assumption that the corresponding temperature anomalies are upwelled along the equator this may have an appreciable impact on the decadal variability of the tropical Pacific. In a future study, we will assess the contribution of these spiciness anomalies to the equatorial heat budget and compare it with the contributions provided by other oceanic mechanisms.

3.5 Supporting Information

Introduction

The Supplementary material provides additional information about the study. However, the information provided here is not necessary for the understanding of the main results of the study. In the Supplementary, we first show a map of the standard deviation of spiciness anomalies which indicates regions of strongest spiciness generation. The figure shows that simulated spiciness is in good agreement with observed spiciness. We further present the particle density maps of the individual experiments without considering the spiciness anomaly of the particles. In the main study, we combine these maps into one composite map due to the high similarity between the individual maps. We also show the particle density map of POS2 considering the spiciness anomaly of the particles. As stated in the main study, this map demonstrates that the effect of POS2 spiciness anomalies can be regarded as negligible. Finally, we display maps showing the spatial distribution of the mean spiciness anomalies for the POS1, POS2 and NEG experiments. These maps provide further information in addition to the temporal evolution of the spiciness anomalies which is shown in the main study.

Map of standard deviation of spiciness anomalies

Figure S3.1 shows the standard deviation of spiciness anomalies in the GFDL-MOM025 model together with the observed standard deviation by Argo floats. This figure provides additional information about the regions of strongest spiciness generation.

Information on individual experiments referring to Figure 2 in the main manuscript

Figures S3.2-S3.5 show the pathways of water parcels for the individual Lagrangian experiments. The relative importance is largely similar in all cases which justifies our approach of combining all particles (cf. Figure 2).

POS2 pathways of spiciness anomalies

Figure S3.6 shows the pathways of spiciness anomalies in the POS2 experiment. This figure has been omitted in the main manuscript due to the negligible impact of these spiciness anomalies given their very low number.

Maps of mean temperature anomalies

Figures S3.7-S3.9 show maps of the mean temperature anomalies for each experiment. The figures provide additional information on the spatial distribution of the temperature anomalies as they propagate along the different pathways. The figures should be considered in conjunction with Figure 3, Figure 4, and Figure 6 in the main manuscript and Figure S3.3, respectively.

Map of standard deviation of spiciness anomalies

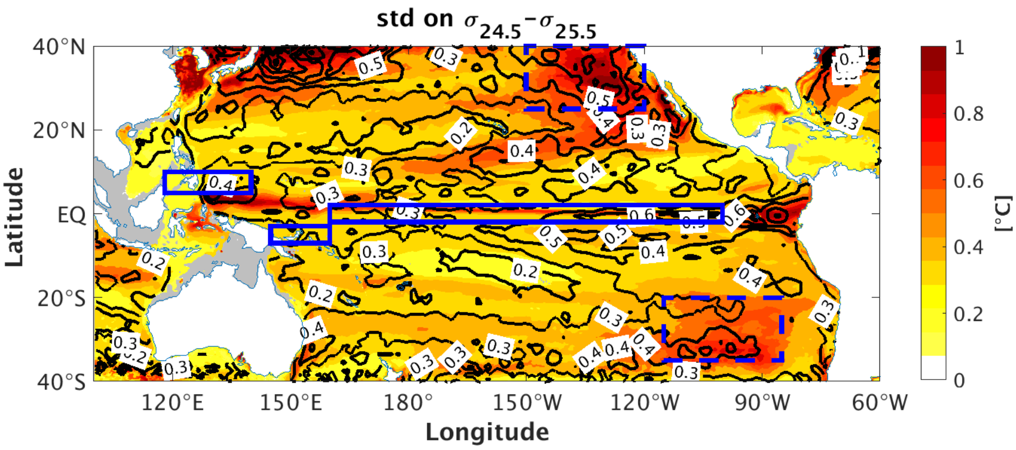

Figure S3.1: Standard deviation of spiciness anomalies averaged over the $\sigma_{24.5}$, σ_{25}, and $\sigma_{25.5}$ surfaces. Black contours with white labels show Argo observations. The dashed boxes indicate the observed source regions of spiciness anomalies. The solid boxes at the western boundary are used to distinguish WBC pathways from interior pathways. The solid box along the equator indicates the region where spiciness anomalies emerge after they are advected from their source region.

Information on individual experiments referring to Figure 2 in the main manuscript

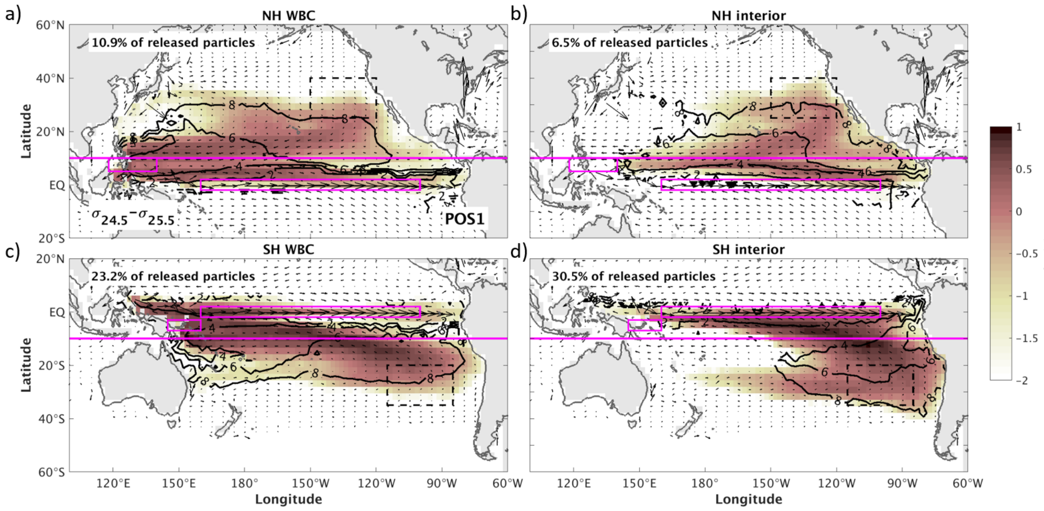

Figure S3.2: Tracer pathways on top of $\sigma_{24.5-25.5}$ for POS1 experiment. **a**) NH WBC, **b**) NH interior, **c**) SH WBC, **d**) SH interior. The boxes are the same as in Figure 1a. Particles have to cross the NH (SH) WBC box and 10°N (S) to be counted to the NH (SH) Western boundary pathway. Particles that cross 10° latitude without crossing the respective WBC box are counted towards the interior pathway. The shading indicates the particle density (percentage of particles that cross grid cell) to identify the pathways, with the colour scale being logarithmic, i.e. 1=10%, 0=1%, -1=0.1%. Overlying arrows show the time mean ocean current velocities averaged over the respective isopycnal layers. The relative contribution of each pathway is indicated as a percentage with respect to all particles crossing 10° latitude in the upper left corner of each panel.

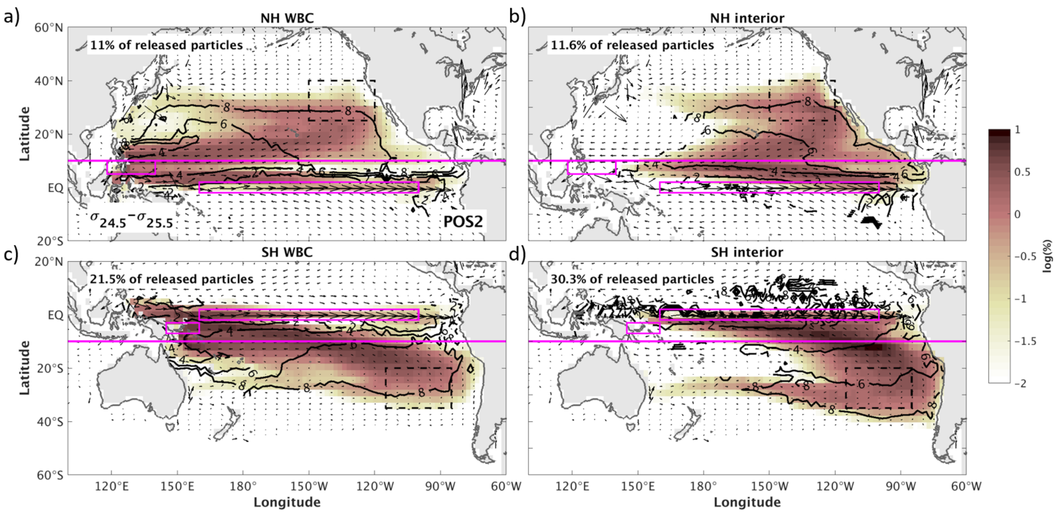

Figure S3.3: Same as Figure S3.2 but for POS2 experiment.

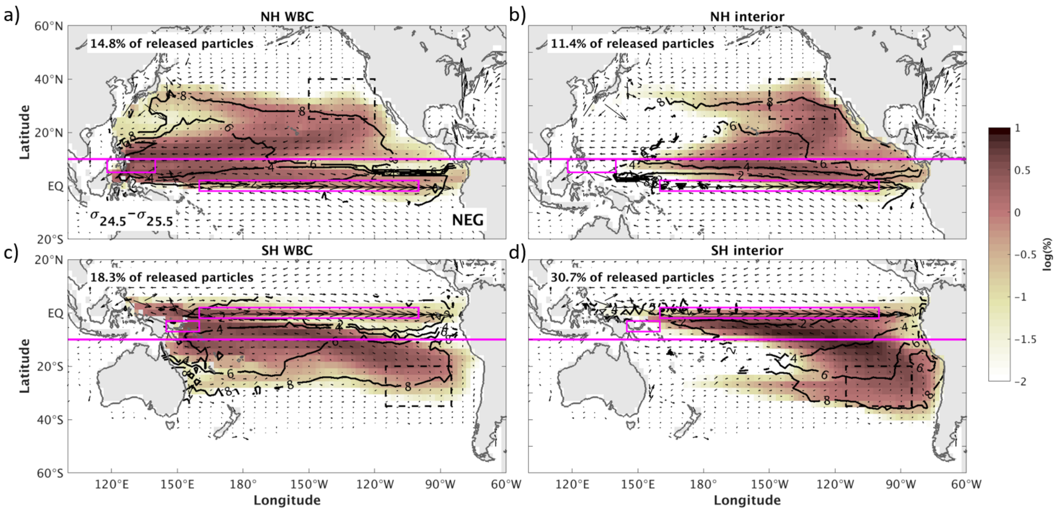

Figure S3.4: Same as Figure S3.2 but for NEG experiment.

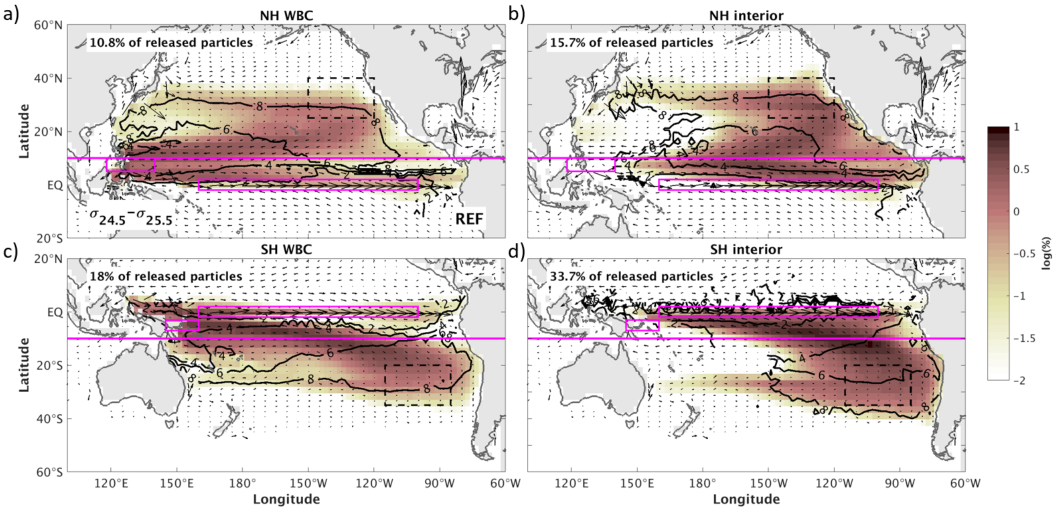

Figure S3.5: Same as Figure S3.2 but for REF experiment.

POS2 pathways of spiciness anomalies

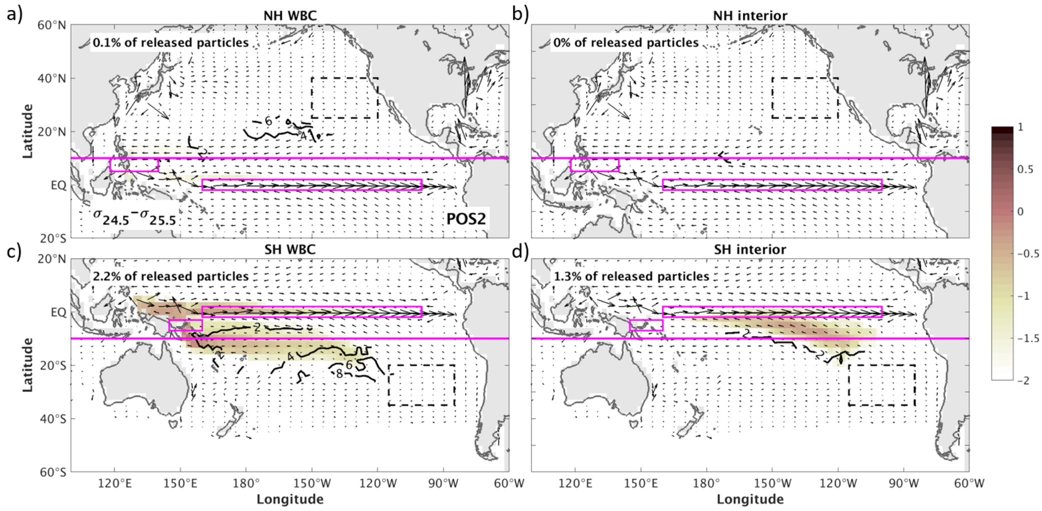

Figure S3.6: Same as Figure S3.3 but with the additional condition that spiciness anomalies of each tracer must not fall below 0.1°C. Shown is the POS2 experiment. White contours indicate the mean travel time of particles in years.

Maps of mean temperature anomalies

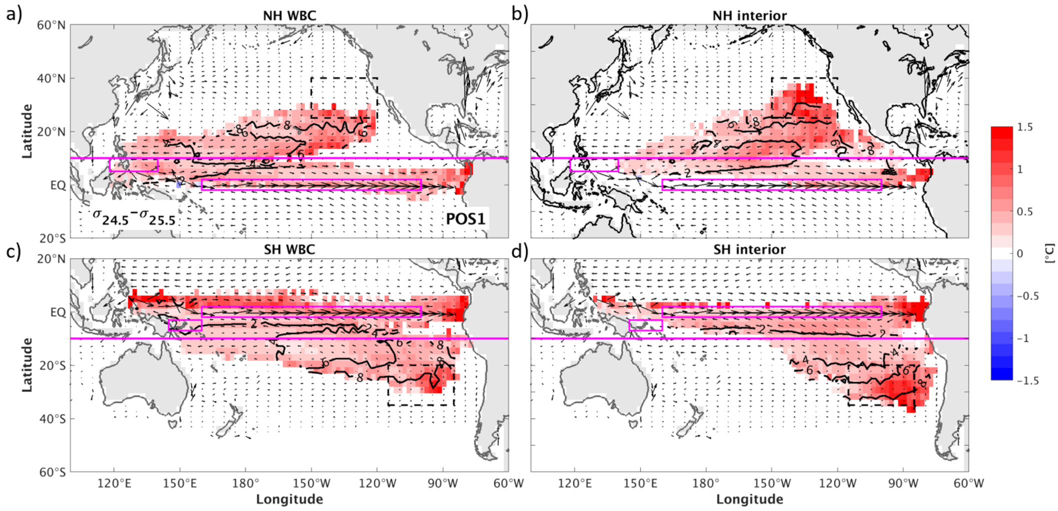

Figure S3.7: Mean temperature anomalies for the particles maintaining their temperature anomaly. **a**) NH WBC, **b**) NH interior, **c**) SH WBC, **d**) SH interior. Shown is the POS1 experiment. White contours indicate the mean travel time of particles in years.

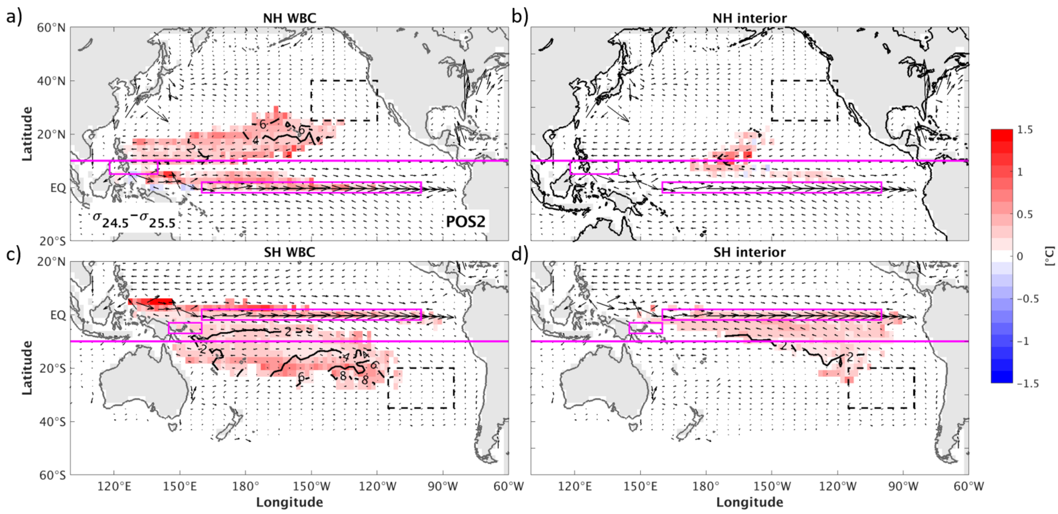

Figure S3.8: Same as Figure S3.7 but for the POS2 experiment.

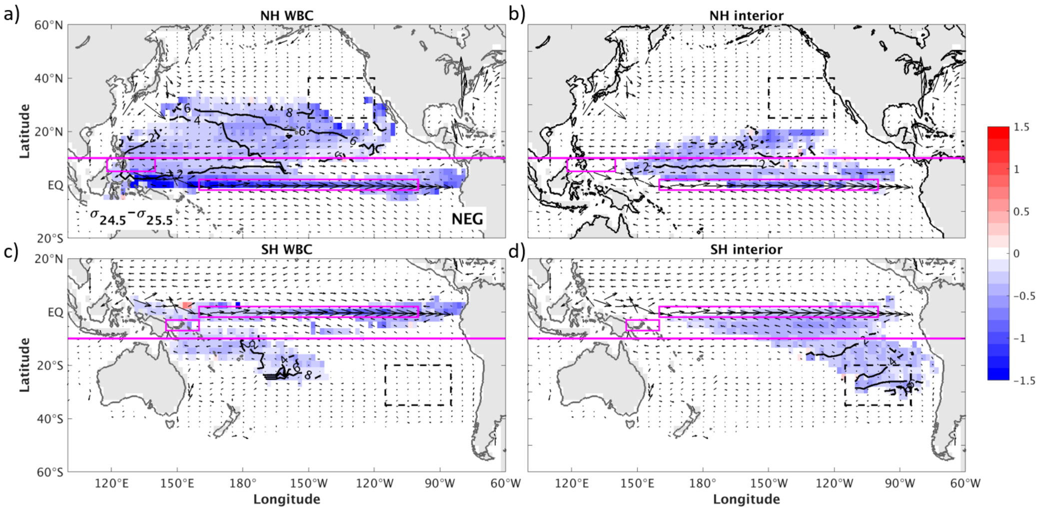

Figure S3.9: Same as Figure S3.7 but for the NEG experiment.

Chapter 4

On the Relative Importance of Spiciness Anomalies on the Equatorial Pacific Mixed Layer Heat Budget

This Chapter is to be submitted for publication as:

Zeller, M., and McGregor, S., 'On the relative importance of spiciness anomalies on the equatorial Pacific mixed layer heat budget', *Geophysical Research Letters*

Preface

We investigate the equatorial Pacific mixed layer heat budget with a focus on the contribution of "spiciness anomalies". Spiciness anomalies are generated in the subtropical Pacific of both hemispheres and are advected with the mean circulation towards the tropics where they finally upwell at the equator and interact with the atmosphere. Equatorial upwelling is known to be a dominant process for generating equatorial temperature anomalies. Spiciness anomalies have been proposed as a mechanism of inducing tropical Pacific decadal variability. However, a quantitative assessment of the impact of spiciness anomalies on the equatorial heat budget is still lacking. In the present study, we use an ocean general circulation model to examine the impact of spiciness anomalies on the vertical heat advection into the equatorial near-surface layer. We distinguish between locally and remotely generated spiciness anomalies. Our results indicate that spiciness anomalies account for 30-60% of the vertical heat advection, with the influence increasing as the region gets confined closer to the equator. The major impact originates from locally generated spiciness anomalies. However, remotely generated spiciness anomalies also have an impact on the equatorial heat budget making up 14-23% of the variance, with the impact decreasing towards the western equatorial Pacific. Our results further suggest that the impact of remotely generated spiciness anomalies is considerably larger during La Niña phases as opposed to El Niño phases.

4.1 Introduction

Ocean spiciness anomalies, which are defined as density-compensating temperature or salinity anomalies (Munk 1981), have been proposed as a potential contributor to tropical Pacific decadal variability (TPDV) (Schneider 2000, 2004). Their impact on TPDV is suggested to arise from the equatorial emergence of remotely generated spiciness anomalies at the surface. A measure of spiciness is anomalous temperature or salinity variations on an isopycnal surface. Spiciness is typically generated in regions of weak ocean stratification stimulating convective vertical mixing. Both in observations (Yeager and Large 2004, 2007) and in models (Zeller et al. subm), these regions have been identified as the subtropical Northeastern and Southeastern Pacific, where unstable vertical salinity gradients prevail. Under favourable conditions, which usually occur in winter when stratification is weak, spiciness is generated through strong diapycnal mixing at the base of the convective boundary layer. This diapycnal mixing creates a shallow transition layer between the mixed layer above and the permanent pycnocline below that is characterised by enhanced stratification due to enhanced gradients of temperature and salinity. Moreover, the transition layer is strongly density compensated with a wide range of different temperature and salinity combinations.

A different generation mechanism of spiciness anomalies is based on the mean spiciness distribution in the Pacific basin (Schneider 2000). If anomalous currents cross mean spiciness gradients, these gradients are displaced, creating spiciness anomalies. Schneider (2000) proposed a decadal spiciness mode by which spiciness anomalies generated in the subtropics are advected to the equator with the mean circulation where they upwell to the surface which generates an atmospheric coupling back to the subtropics where spiciness anomalies of a different sign are generated and transported to the equator closing a 10 year cycle.

In a subsequent study, (Schneider 2004) examined the impact of surfacing spiciness anomalies on the overlying atmosphere by injecting artificial spiciness anomalies in the equatorial Pacific upwelling region. His results confirmed a coupled mode of ocean-atmosphere variability. However, the author also suggests that the involved feedbacks are relatively weak and therefore the implications on the decadal variability are small.

Zeller et al. (subm) have shown that in some cases spiciness anomalies can be advected from their generation region in the subtropics to the equator. The aim of the present study is a quantitative assessment of the impact of spiciness anomalies on the equatorial Pacific mixed layer heat budget. We distinguish between locally generated spiciness anomalies and remotely generated spiciness anomalies that have been advected from the subtropics. However, the remotely generated spiciness anomalies are of bigger interest as they provide potential predictability given their transit time of several years.

4.2 Model and Methods

4.2.1 The Ocean Model

We use the GFDL-MOM025 global ocean model (Spence et al. 2014) which is based on the GFDL CM2.5 coupled climate model (Delworth et al. 2012). The GFDL-MOM025 model is coupled to the GFDL Sea Ice Simulator model. The model has a 1/4° Mercator horizontal resolution globally. It further has 50 vertical levels with vertical level thicknesses ranging from 10 m at the surface to about 200 m at depth. Sea surface salinity is restored to a seasonally varying climatology on a 60 day time scale. A 40 year spin-up control simulation that is forced with the ERA-interim climatology of heat, freshwater and momentum fluxes, is used to equilibrate the model. The model output is provided as 5-day averages.

The ocean model simulation utilised here is forced with ECMWF ERA-interim reanalysis data (Dee and Uppala 2009). The heat and freshwater fluxes are computed from climatological surface temperature, surface humidity and surface winds via bulk formulas. The momentum flux is computed with the fully varying reanalysed wind field. The simulation spans the time period from January 1979 to May 2016 which amounts to a bit more than 37 years. The ERA-interim winds were selected to overcome the strong trend biases in wind stress and wind stress curl over the tropical Pacific that are known to be present in the NCEP/NCAR (National Centers for Environmental Prediction/National Center for Atmospheric Research) wind product (McGregor et al. 2012a). In their study, McGregor et al. (2012a) compared the observed and modelled trend pattern of sea surface height (SSH) using different wind forcings. They found that the spatial correlation of the trend patterns is higher when SSH is forced by ERA-interim winds (0.83) than when it is forced by NCEP/NCAR winds (0.41). It is noted that while this choice moved us away from the more balanced fluxes of CORE forcing (Large and Yeager 2009), we believe that the use of the more realistic wind stress forcing is more appropriate to address the proposed research questions.

4.2.2 Calculation of the Heat Budget

Given a stationary three-dimensional box with volume V_D and box averaged temperature

$$T_D = \frac{\iiint_D T \; dx \; dy \; dz}{V_D}, \tag{4.1}$$

the change in T_D with time is given by:

$$\frac{\delta T_D}{\delta t} = \frac{Q_{sfc} - Q_{pen}}{\rho_0 \; C_p \; V_D} + \langle Q_{adv} \rangle + \langle resid \rangle, \tag{4.2}$$

where Q_{sfc} is the horizontally averaged net surface heat flux, Q_{pen} is the horizontally averaged penetrative solar flux at the base of the box, $\rho_0 = 1026 \; kg \; m^{-3}$ is a reference ocean potential density, $C_p = 3995 \; J \; kg^{-1} \; K^{-1}$ is the specific heat capacity of seawater, and Q_{adv} is the net oceanic advection of temperature into the box from the sides and from the bottom. The term $resid$ represents residual effects which are not resolved by the model. These residual effects include sub-grid scale lateral mixing, local and nonlocal vertical mixing, as well as entrainment from below. The angle brackets $\langle\ \rangle$ signify a volume average over V_D.

The advective term is calculated following the methodology of Lee et al. (2004):

$$\langle Q_{adv} \rangle = -\frac{1}{V_D} \int_{S_D} (\mathbf{u} \cdot \mathbf{n})\ \delta T\ dS, \tag{4.3}$$

where $\int_{S_D}$ denotes the integral across the bounding surface of the box, $\mathbf{u} = (u, v, w)$ is the three dimensional current velocity, and $\mathbf{n}$ is the outward pointing unit normal vector along S_D. $\delta T = T - T_D$ is the temperature anomaly at the boundary relative to the box averaged temperature.

In the present study, we are interested in the relative contribution of the heat advection through the individual boundaries of the box. The methodology applied for the calculation of the advective heat transport allows the computation of heat advection through single surfaces of the box by applying Equation 4.3 accordingly. For instance, the temperature advection through the western boundary can be computed as:

$$\langle Q_{adv\_west} \rangle = \left[\iint_{S_{west}} u\ \delta T\ dy\ dz \right]' / V_D, \tag{4.4}$$

where the prime ($'$) denotes anomalies to the mean seasonal cycle. In this case, the time dependent temperature anomaly is multiplied by the time dependent zonal velocity at each grid point of the western boundary surface. The result is then integrated over the western boundary surface and finally divided by the box volume to yield the flux of temperature *(K/s)* into (positive) or out of (negative) the box.

4.2.3 Spiciness Anomalies

To detect the portion of a temperature anomaly that is density compensated by salinity at each location and point in time, we convert the 3-D Cartesian model temperature field to density coordinates by vertical linear interpolation onto defined surfaces of constant density. The defined density surfaces range from σ_{22} to σ_{27} with an increment of 0.1 kg/m^3. Spiciness anomalies are then defined as nonseasonal anomalies of temperature on the isopycnal surfaces.

To examine the impact of spiciness anomalies on the equatorial heat budget, we utilise the Nino3 region (5°S-5°N, 150°W-90°W). To assess the sensitivity of the results to the position and extent of the equatorial region, we also define other boxes along the equator (see boxes in Figure 4.2). These are: the Nino3.4 region (5°S-5°N, 170°W-120°W), an elongated equatorial box (2°S-2°N, 160°E-100°W), and a narrow version of the Nino3 region (2°S-2°N, 150°W-90°W). As a lower vertical boundary of all boxes, we choose the 75 m level. At this level, we still have a considerable magnitude of upwelling of up to 4 cm/h (Figure 4.1). We also ensure that our defined range of isopycnal surfaces all intersect with this level in our defined boxes at least during some periods of the simulation (Figure 4.2).

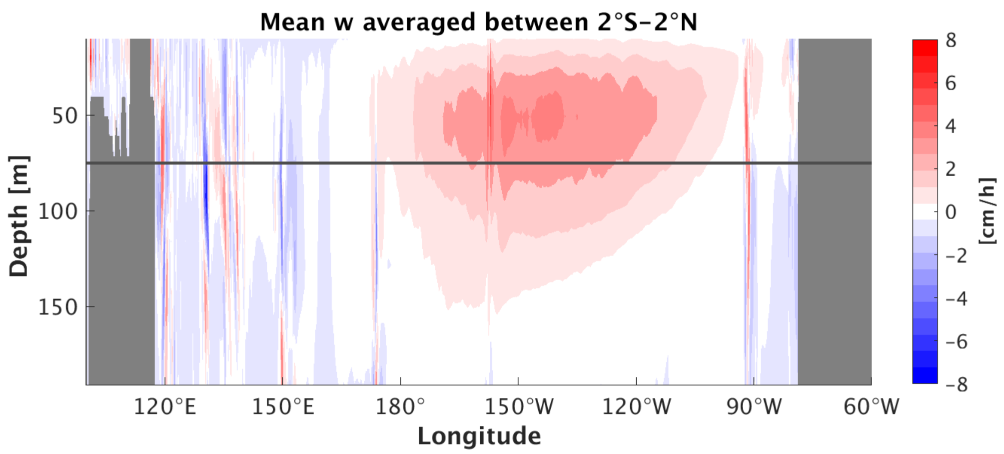

Figure 4.1: Mean vertical velocity averaged over the entire time period (1979-2016) and between 2°N and 2°S. The 75 m level is indicated as a horizontal black line.

4.3 Results

4.3.1 Equatorial Heat Budget

As our model simulation is forced with heat and freshwater fluxes derived from climatological surface conditions, changes in the equatorial heat content are primarily

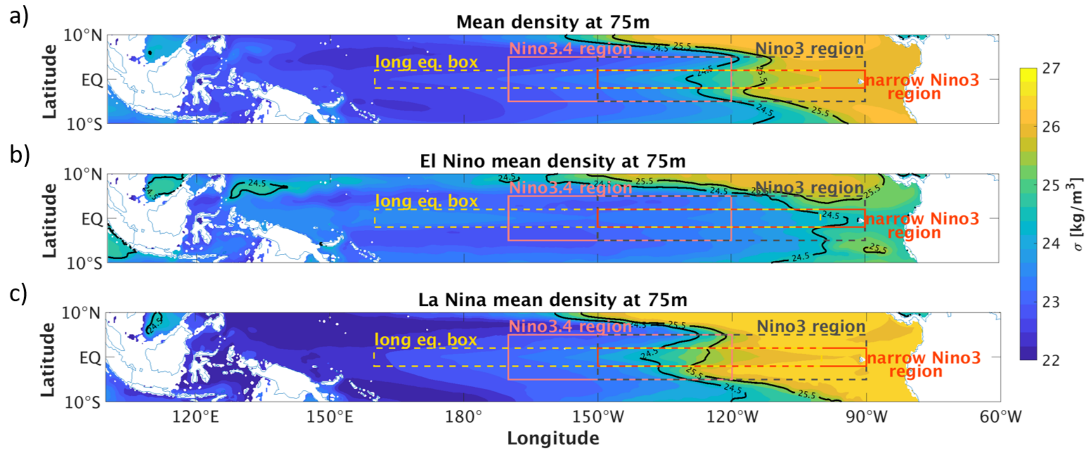

Figure 4.2: Density on the 75 m level averaged over **a**) the entire time period (1979-2016), **b**) the three strongest El Niño events (DJF, 1982/83, 1997/98, 2015/16), and **c**) the three strongest La Niña events (DJF, 1988/89, 2007/08, 2010/11). The $\sigma_{24.5}$ and $\sigma_{25.5}$ surfaces are highlighted as black contours. The boxes indicate the Nino3.4 region (5°S-5°N, 170°W-120°W), the Nino3 region (5°S-5°N, 150°W-90°W), a narrow Nino3 region (2°S-2°N, 150°W-90°W), and an elongated equatorial box (2°S-2°N, 160°E-100°W).

associated with advection of temperature into the box from the sides and from the bottom (Figure 4.3). The temperature changes associated with the surface heat flux act as a damping to the changes caused by advection. The sum of the temperature tendencies associated with the surface heat flux and the temperature advection closely resembles the time derivative of the box averaged temperature (r=0.85), which is expected from Equation 4.2. Any differences are due to residual effects that are not explicitly calculated in the heat budget, as described in section 4.2.2.

We next subdivide the net temperature advection into the defined equatorial region into the advection through the individual boundary surfaces of the box as demonstrated in Equation 4.4. Heat is advected into the box in the lead-up to an El Niño event and out of the box after the event peak setting the conditions for a subsequent La Niña event (black line, Figure 4.4). The heat transport largely occurs through the bottom and the Western boundaries which is in line with anomalous westerlies (easterlies) moving warm water to the east (west) through the Western boundary as well as with anomalous downwelling (upwelling) vertically moving warm (cold) water through the bottom surface during El Niño (La Niña) events (e.g., Meinen and

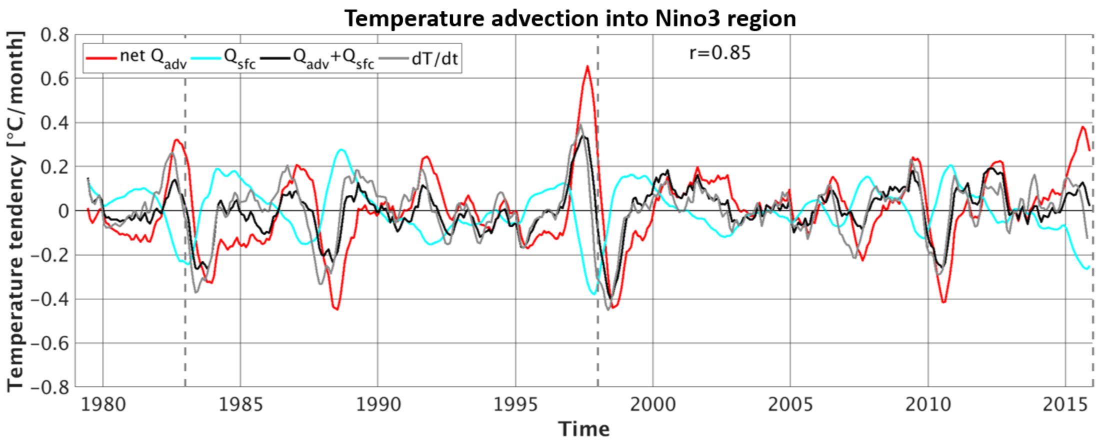

Figure 4.3: Heat budget of the Nino3 region above 75 m. Shown are the temperature tendencies of the box averaged temperature associated with the net surface heat flux (cyan), the net advection (red), and the sum of surface heat flux and net advection (black). Also shown is the temperature tendency of the box averaged temperature (grey).

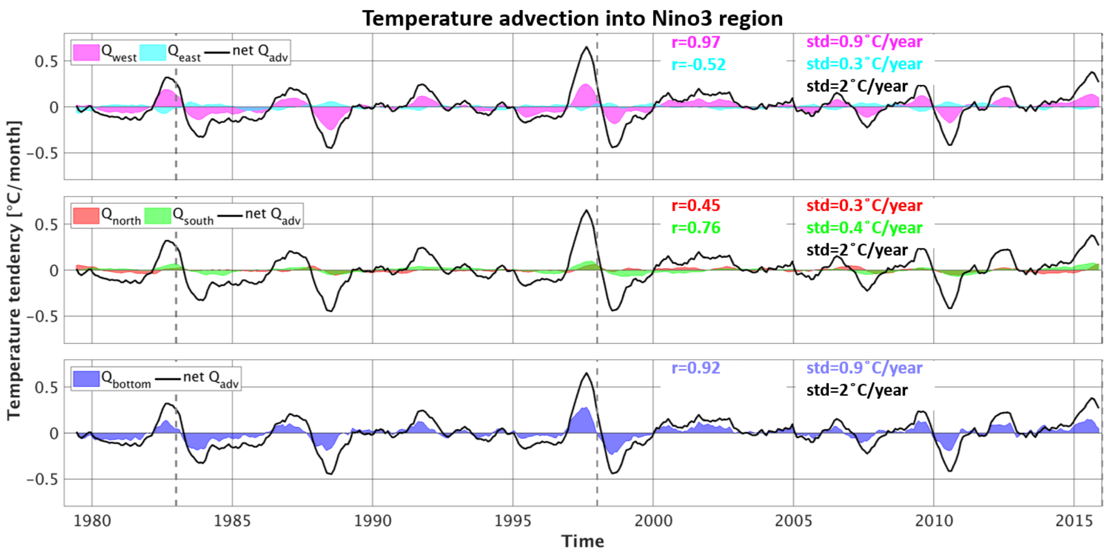

Figure 4.4: Contributions to the heat advection into the Nino3 region. Shown are the total heat advection (black lines), the contributions through the Western (magenta) and Eastern (cyan) boundaries, the contributions through the Northern (red) and Southern (green) boundaries, and the contribution through the bottom (blue) boundary. The correlation coefficients between the total advection and its individual components as well as the standard deviations are displayed in the plot.

McPhaden 2000). Transports through the Eastern, Northern and Southern boundaries are comparatively small (Figure 4.4). The transport through the bottom (thermocline feedback + Ekman feedback) and the Western boundary (zonal advective feedback) each explain about half of the total heat transport into the region. Both transports are highly correlated with the total transport (bottom: 0.92, West: 0.97).

4.3.2 Vertical Heat Transport

Spiciness anomalies are upwelled to the surface in the equatorial outcropping region after joining the equatorial undercurrent (EUC), forming part of the heat advection through the bottom boundary of the equatorial box. We, therefore, further subdivide the heat transport through the bottom boundary $w\delta T$ by breaking its two variables, w and $\delta T = T - T_D$, down into their mean and anomalous parts, such that $w = \overline{w} + w'$ and $\delta T = \overline{\delta T} + \delta T'$:

$$w\delta T \equiv w'\overline{\delta T} + \overline{w}\delta T' + w'\delta T' + \overline{w\delta T}, \tag{4.5}$$

where the overline ($^{-}$) denotes the mean seasonality and the prime ($'$) denotes anomalies to the mean seasonality. T and T_D represent the temperature at the bottom boundary of the box and the boxed averaged temperature, respectively. The dominating component of vertical heat transport is the mean upwelling of anomalous temperature ($\overline{w}\delta T'$, thermocline feedback) which represents the effect of Kelvin waves on the equatorial heat content. In the leadup to an El Niño event anomalous westerlies excite an equatorial downwelling Kelvin wave as well as an upwelling Rossby wave (e.g., Neske and McGregor 2018). The eastward propagating Kelvin wave causes an instantaneous recharge of heat in the equatorial Pacific. The westward propagating Rossby wave is reflected at the western boundary into an upwelling Kelvin wave which induces a delayed discharge of heat. The thermocline feedback correlates at 0.74 with the total vertical heat advection and exhibits almost the same variance (blue line, Figure 4.5). The second largest contribution comes from the anomalous upwelling of mean temperature ($w'\overline{\delta T}$, Ekman feedback). The major effect of the Ekman feedback is on the recharge of heat shortly after the peak of El Niño events due to its rapid reversal from weak to strong upwelling (red line, Figure 4.5). This rapid reversal counteracts the general discharge of heat after the peak of El Niño events driven by the mean upwelling of cold temperature anomalies and promotes a fast transition back to neutral or El Niño-like conditions. The anomalous upwelling of anomalous temperature $w'\delta T'$ largely acts as a damping to the total vertical heat advection (r=-0.41) and ENSO. However, due to its small magnitude it only has a minor effect on the total vertical heat advection (green line, Figure 4.5). Since we are looking at anomalies there is no effect from the mean upwelling of mean temperature ($\overline{w\delta T}$).

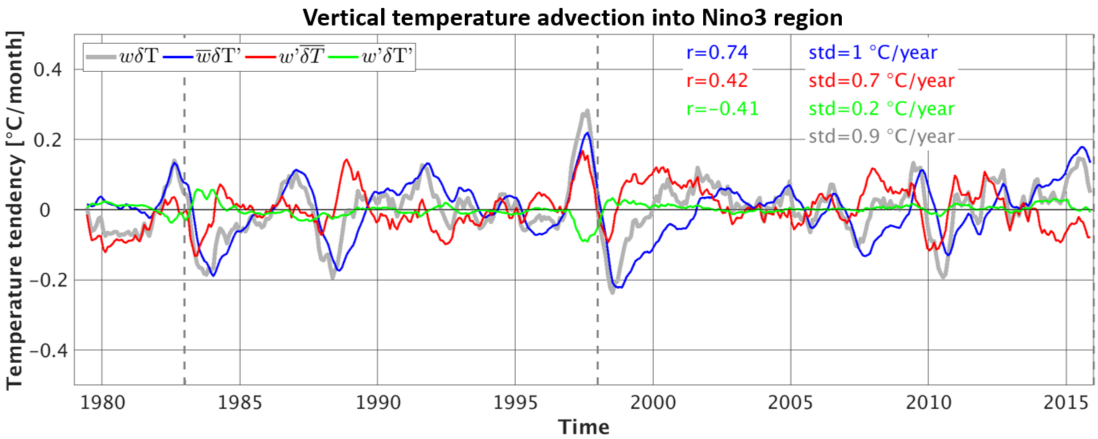

Figure 4.5: Contributions to the vertical heat advection into the Nino3 region. Shown are the total heat advection (grey), the mean advection of anomalous temperature (blue), the anomalous advection of mean temperature (red), and the anomalous advection of anomalous temperature (green). The correlation coefficients between the total vertical advection and its individual components as well as the standard deviations are displayed in the plot.

4.3.3 The Contribution of Spiciness Anomalies

On the basis that the vertical heat advection into the upper equatorial Pacific is dominated by the mean upwelling of anomalous temperature, we are seeking to further separate the contribution of spiciness anomalies to the total $\overline{w}\delta T'$ mechanism. A comparison of the Nino3 region bottom surface (75 m) temperature anomalies with the spiciness anomalies averaged over the same regional surface suggests an appreciable role of spiciness anomalies for the total vertical heat advection (Figure

4.6). It is clear that both temperature anomalies are highly correlated and both exhibit significant interannual peaks. It is also clear that the spiciness anomalies have a reduced amplitude relative to the temperature anomalies, which suggests that they play a secondary supporting role rather than dominating the temperature changes.

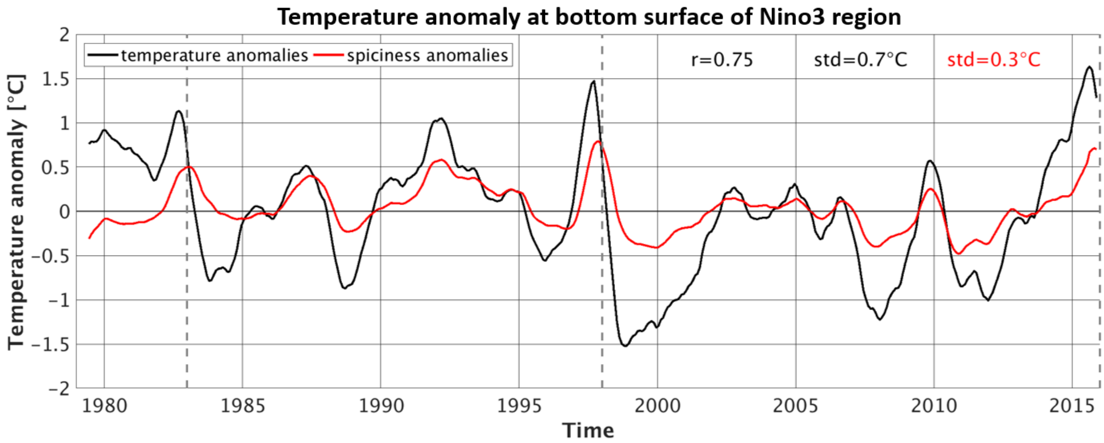

Figure 4.6: Temperature anomalies (black) and spiciness anomalies (red) spatially averaged over the bottom boundary of the Nino3 region at 75 m.

To compute the vertical heat advection through spiciness anomalies, we apply Equation 4.4 to the bottom surface. However, rather than using the temperature anomalies with respect to the box averaged temperature for δT, we only utilise the anomalous spiciness component of the temperature anomalies. The heat advection through spiciness anomalies is clearly detectable but weaker than the total $\overline{w}\delta T'$ advection (Figure 4.7). The effect of spiciness is mainly a reinforcement of the ENSO cycle, however, the heat advection via anomalous spiciness appears to lag the total $\overline{w}\delta T'$ advection by 2 months.

Our primary interest lies in the contribution of subtropically generated spiciness anomalies because of their proposed role in driving tropical Pacific decadal variability and their associated potential predictability. Previous studies have shown that these remotely generated spiciness anomalies preferably travel towards the tropics on isopycnal surfaces between $\sigma_{24.5}$ and $\sigma_{25.5}$ (Schneider 2000 and Chapter 3 of this thesis). We, therefore, divide the isopycnal range as defined earlier (see section

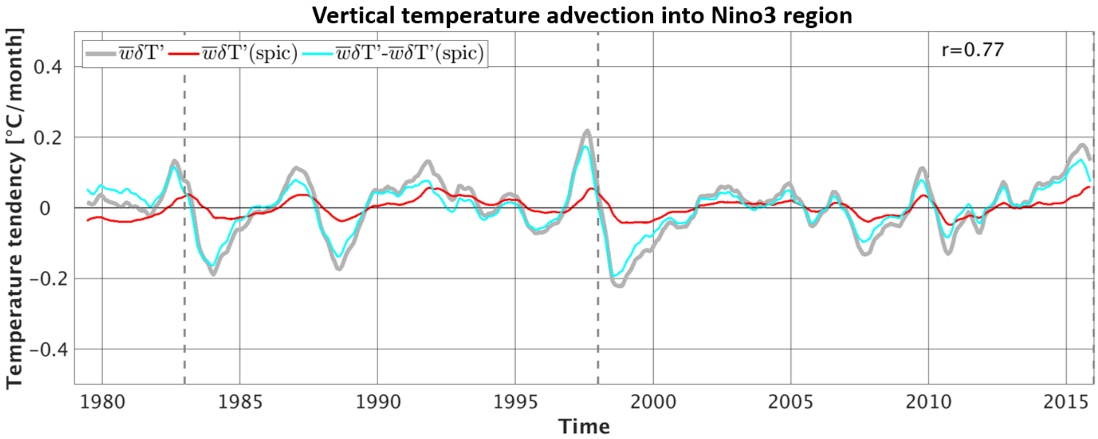

Figure 4.7: Contributions to the total $\overline{w}\delta T'$ heat advection into the Nino3 region. Shown are the total heat advection (grey), the heat advection through spiciness anomalies (red) and the difference between the former two (cyan).

4.2.3) into three layers: isopycnals $< \sigma_{24.5}$ (top layer), isopycnals between $\sigma_{24.5}$ and $\sigma_{25.5}$ (middle layer), and isopycnals $> \sigma_{25.5}$ (bottom layer).

Spiciness anomalies upwelled into the Nino3 region are strong in all three isopycnal layers (Figure 4.8b) with magnitudes of up to 1.5°C, both positive and negative. However, the area of intersection with the Nino3 region's bottom surface strongly differs between the three isopycnal layers (Figure 4.8c). Generally, the top layer covers the largest area (magenta line in Figure 4.8c), followed by the bottom layer (green line in Figure 4.8c), while the middle layer mostly only shows narrow stripes of intersection (blue line in Figure 4.8c). This means that even though remotely generated spiciness anomalies may exhibit an appreciable magnitude, their contribution to the total spiciness of the Nino3 region's bottom surface is relatively small after being weighted with the intersecting area (Figure 4.8a).

This is also apparent when calculating the vertical heat advection into the Nino3 region via spiciness anomalies in all three isopycnal layers (Figure 4.9). Generally, the contributions to the total signal all vary in phase. However, the largest contribution is made by the top layer ($<\sigma_{24.5}$), which explains 85% of the total variance. The signals from the middle and bottom layers are much smaller and closely resemble each other. The remotely generated spiciness anomalies of the middle layer

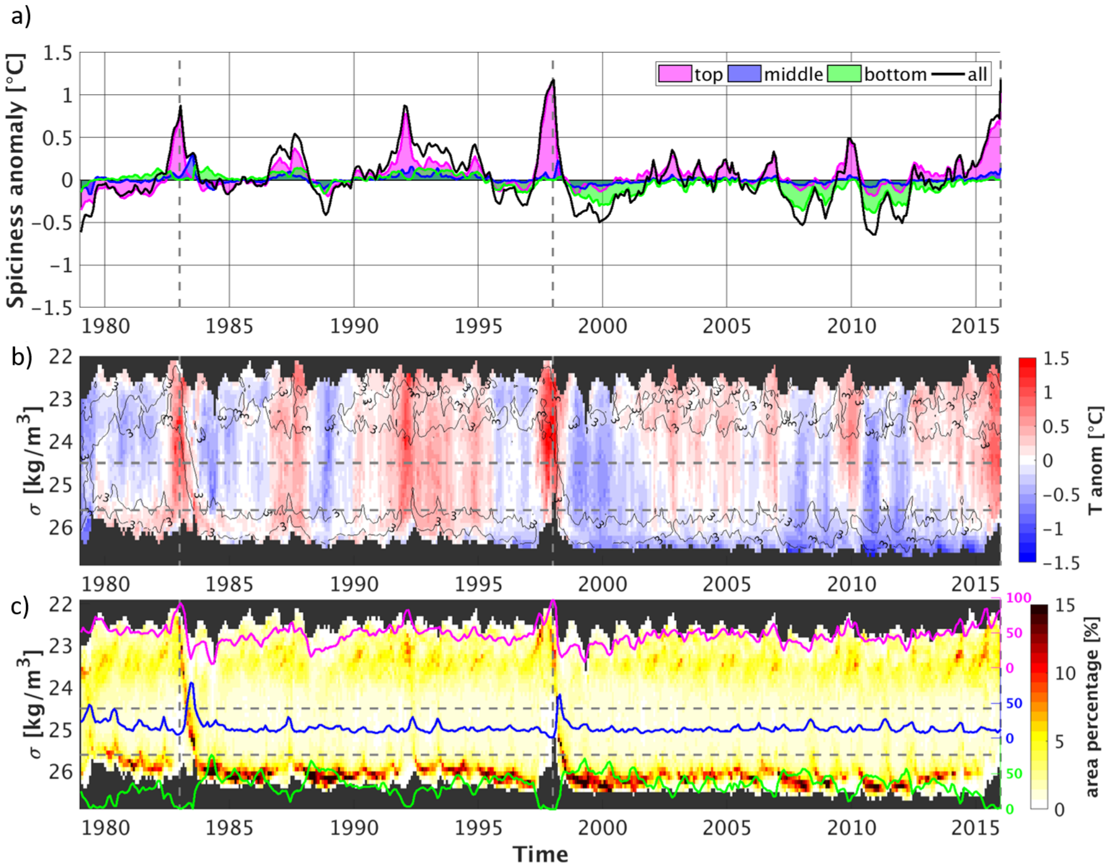

Figure 4.8: **a**) Spiciness anomalies at the 75 m level integrated across all isopycnal surfaces and weighted by the outcropping area of each isopycnal at each point in time. **b**) Spiciness anomalies at the 75 m level. Shown are all isopycnals between σ_{22} to σ_{27} that intersect with this depth level. The horizontal dashed lines indicate the $\sigma_{24.5}$ and $\sigma_{25.5}$ isopycnals. **c**) Area percentage of outcropped (75 m) isopycnals at each time step relative to the total surface area of the Nino3 region. The magenta, blue, and green lines show the total area percentage of the top, middle, and bottom isopycnal layers, respectively, as defined in the text.

have their biggest impact during La Niña phases while their impact during El Niño phases is mostly very small, except for the first half of the 1990s.

4.3.4 Sensitivity to the Position and Extent of the Equatorial Box

If we test the sensitivity of our results to the position and extent of the equatorial box, we see a general consistency of the results (Table 4.1). In all regions, the heat

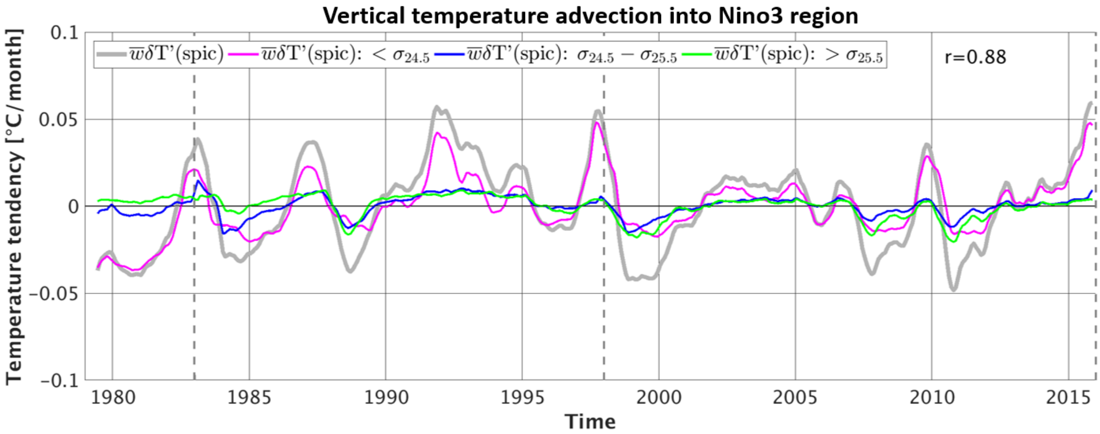

Figure 4.9: Contribution of spiciness anomalies to the total $\overline{w}\delta T'$ heat advection into the Nino3 region. Shown are the total advection through spiciness anomalies (grey) and its contributions by the top (magenta), middle (blue), and bottom (green) isopycnal layers as defined in the text. The correlation coefficient between the total spiciness signal and the contribution by the middle layer of isopycnals is 0.88.

budget is controlled by the net advection through the sides of the box and is damped by the surface heat flux (cf. Figure S4.1). Also, in all cases, the transport through the bottom boundary of the box is the dominating component (cf. Figures S4.2-S4.4). However, towards the east (Nino3.4 region and elongated equatorial box) the vertical heat advection increasingly leads the total heat advection, which is consistent with the ocean dynamics theory of warm water volume changes that implies a change of the thermocline depth (vertical heat advection via thermocline feedback) before an upper ocean adjustment through horizontal currents (horizontal heat advection via zonal advective feedback). According to this mechanism, during an El Niño event (conversely for a La Niña), anomalous westerly winds chronologically lead to decreases in Ekman transport, surface divergence, South equatorial current, equatorial upwelling, and eventually in geostrophic meridional transports, thus in pycnocline convergence.

In terms of the different mechanisms of vertical temperature advection, the mean upwelling of anomalous temperature ($\overline{w}\delta T'$) clearly dominates in the two Nino3 boxes as well as in the Nino3.4 box (cf. Figure S4.5 a and b). This is particularly apparent in the Nino3.4 region, which is almost exclusively driven by the $\overline{w}\delta T'$ mechanism

Table 4.1: Correlation coefficients between various heat advection components (rows) for the different equatorial boxes (columns).

	Nino3 box	Nino3.4 box	Nino3 narrow box	Equatorial box
$Q_{adv} + Q_{sfc}$ vs. dT/dt	0.85	0.5	0.8	0.28
Q_{adv} vs. Q_{adv_bottom}	0.92	0.97	0.84	0.53
$w\delta T$ vs. $\overline{w}\delta T'$	0.74	0.96	0.73	0.38
T_{anom} vs. $spic_{anom}$	0.75	0.5	0.73	0.52
$\overline{w}\delta T'$ vs. $\overline{w}spic'$	0.77	0.69	0.7	0.62
$\overline{w}spic'$ vs. $\overline{w}spic_{middle}'$	0.88	0.67	0.89	0.82

as the other two mechanisms are relatively weak and appear to cancel each other. Only in the elongated equatorial box the influence of the Ekman feedback ($w'\overline{\delta T}$) appears to be of equal importance to $\overline{w}\delta T'$ (Figure S4.5 c). This is due to the fact that in the western equatorial Pacific the thermocline is generally much deeper than 75 m. Consequently, temperature anomalies on this level are comparatively small (cf. Figure S4.6c) and anomalous vertical temperature advection is largely driven by anomalous upwelling of cold water.

Despite considerable spiciness anomalies existing at the bottom surface of the Nino3 region, the associated vertical heat advection into the box shows a reduced impact of spiciness anomalies (Figure 4.7). The same applies to the Nino3.4 region (Figure S4.7 a). Interestingly, the impact of spiciness anomalies doubles when considering the elongated equatorial box (Figure S4.7c) even though spiciness anomalies averaged across the bottom boundary are slightly smaller (Figure S4.6c). The reason for this is that the fraction of the temperature anomaly at the bottom boundary which is density compensated is large compared to the other regions (Figure S4.6c). Moreover, the mean upwelling is largest closer to the equator. Both conditions increase the effect of spiciness on the mixed layer heat content. The narrow Nino3 region also shows an increased impact of spiciness anomalies compared to the default Nino3 region (Figure S4.7b). This increased effect is due to larger spiciness anomalies closer to the equator (cf. Figure S4.6b and Figure 4.6).

The outcrop area of isopycnals differs between the different regions (cf. Figure 4.8

and Figures S4.8-S4.10). In the Western and central equatorial Pacific isopycnals $< \sigma_{24.5}$ dominate while in the Eastern equatorial Pacific isopycnals $> \sigma_{25.5}$ occupy the largest areas of the boxes. As a consequence, the Nino3.4 region and the elongated equatorial region are even more dominated by the locally generated spiciness anomalies on isopycnals $< \sigma_{24.5}$ (Figures S4.11 a and c). The narrow Nino3 region, on the other hand, shows a clear signal of heat advection through remotely generated spiciness anomalies, primarily during La Niña phases (Figure S4.11b).

4.4 Discussion and Conclusion

In the present study, we examined the near-surface heat budget in the equatorial Pacific using an ocean general circulation model. Our results show a damping effect of the surface heat flux relative to the advective term with a slight lag of about 2-3 months (Figure 4.3 and Figures S4.1). This predominant damping response is because the ocean is forced with a prescribed climatological heat flux. Thus, positive ocean-atmosphere feedbacks (e.g., wind-evaporation-sea surface temperature feedback) that can enhance heat flux variability cannot occur in the model. The damping occurs due to positive (negative) anomalous heat advection into the box creating a negative (positive) anomalous ocean-atmosphere temperature difference, that consequently leads to negative (positive) anomalous surface heat flux. These atmospheric feedbacks are important when further investigating the impact of SST anomalies on the local and remote climate. However, this idealised model setting does not influence the advection of spiciness anomalies to the equator and their impact on the near-surface heat budget in the equatorial Pacific.

The finding that the temperature advection into the box is dominated by vertical advection through the bottom boundary (Figure 4.4 and Figures S4.2-S4.4) is consistent with previous studies (e.g., Lee et al. 2004; Huang et al. 2012; Boucharel et al. 2015). Moreover, the increased importance of zonal temperature advection towards the western equatorial Pacific is in line with the results of Vialard et al.

(2001) and McPhaden (2002).

We further examined the different mechanisms of vertical temperature advection into the box. Our results show that the vertical temperature advection is dominated by the mean upwelling of anomalous temperatures for three out of the four regions identified here, with the exception being the elongated equatorial box where the anomalous upwelling of mean temperatures also plays a significant role. Consistent with Huang et al. (2012), our results indicate that during the build-up phase of El Niño events, both the thermocline feedback ($\overline{w}\delta T'$) and the Ekman feedback ($w'\overline{\delta T}$) contribute to the recharge of heat, while during the decay phase the discharge of heat is controlled by the thermocline feedback alone. The nonlinear vertical advection term ($w'\delta T'$) acts as a weak damping.

Our results further show an increased variance of the vertical temperature advection and its components for the two regions closer to the equator (Figure S4.7 b and c). The reason for the stronger signal in these regions compared to the Nino3 (Figure 4.5) and Nino3.4 (Figure S4.7a) regions is that the mean as well as the anomalous upwelling is confined to a narrow band around the equator. On top of this, the signal becomes even stronger towards the east where the mean upwelling has its maximum (Figure 4.1).

Regarding the contribution of spiciness anomalies, about 30% of the total vertical temperature advection arises from the mean upwelling of spiciness anomalies for the Nino3 region and about 25% for the Nino3.4 region. For the regions confined closer to the equator the fraction even rises to about 67%. The reason for the increased influence of spiciness anomalies closer to the equator is the increased fraction of spiciness anomalies versus temperature anomalies close to the equator. While this fraction is about 40% for the meridionally wider regions it is 56% for the meridionally narrower regions. In fact, while the temperature anomalies decrease towards the west, spiciness anomalies seem to be rather evenly distributed across the entire equatorial Pacific. This arises from a comparison of the spiciness anomalies in the Nino3 region (Figure 4.6) and the elongated equatorial region (Figure S4.6c). The spiciness anomalies are of the same order of magnitude at a consistently high area coverage (cf. Figure 4.8b,c and Figure S4.10b,c).

The bulk of spiciness anomalies upwelled into the equatorial Pacific mixed layer are locally generated spiciness anomalies on the isopycnal range $< \sigma_{24.5}$. As examined in the previous chapter of this thesis (Chapter 3), there are two mechanisms that can generate local spiciness anomalies: i) generation through anomalous advection across mean spiciness gradients, and ii) generation through a changing proportion of NH versus SH advection of mean spiciness. However, in the present study our initial interest lies in the impact of remotely generated spiciness anomalies, due to their proposed role in driving tropical Pacific decadal variability and the potential predictability they may provide. Knowing that remotely generated spiciness anomalies propagate along isopycnals within the range $\sigma_{24.5}$-$\sigma_{25.5}$, our results suggest a relatively weak vertical temperature advection signal associated with spiciness anomalies of that range. For the Nino3 region, 23% of the total spiciness effect arises from remotely generated spiciness anomalies. As expected, the impact decreases towards the west with 18% for the Nino3.4 region and only 14% for the elongated equatorial region. This is because of the outcropping region of the $\sigma_{24.5}$-$\sigma_{25.5}$ isopycnal range mostly being confined to the eastern equatorial Pacific (Figure 4.2).

In summary, our results indicate a temporal asymmetry of the impact of remotely generated spiciness anomalies on the tropical Pacific mixed layer heat budget. During El Niño phases, the impact of the subtropical spiciness anomalies seems negligible. However, during La Niña phases, these spiciness anomalies create a weak but recognisable signal which amplifies the discharge of heat. Consequently, during a longer period of increased La Niña events, subtropical spiciness anomalies continually act to enhance a negative anomalous upper ocean heat content over several years. This prolonged negative upper ocean heat content further projects onto sea surface temperature anomalies, which eventually alter atmospheric conditions in the tropical Pacific. Thus, subtropical spiciness anomalies are able to imprint on tropical Pacific decadal variability. While we acknowledge that spiciness anomalies may constitute a minor component of the total equatorial mixed layer heat budget, these anomalies do impact the background state in which ENSO operates, and thus leave open the question as to how these changes may modulate ENSO behaviour and activity.

4.5 Supporting Information

Introduction

The Supplementary material provides additional information about the study. However, the information provided here is not necessary for the understanding of the main results of the study. In the Supplementary, we show the figures that correspond to the sensitivity analysis (Section 3.4 of the main text). We therefore show the same plots as in the main study, however, for the three additional equatorial regions.

Heat budgets

Figure S1 shows the heat budget for each region. We compare the surface fluxes to the net heat advection and show that the net heat advection tends to be the dominant term.

Components of heat advection

In Figure S2-S4, the net heat advection is subdivided into the heat advection through the individual boundary surfaces, for each region, respectively. In all cases, the heat advection through the bottom surface is the dominating component.

Components of vertical heat advection

In Figure S5, we further subdivide the heat advection through the bottom surface into contributions from the mean and anomalous terms. The main message is that the vertical heat advection is dominated by the mean upwelling of anomalous temperatures ($\overline{w}\delta T'$) in the Nino3.4 and narrow Nino3 regions, while in the elongated equatorial box the total vertical advection is contributed to by both the mean upwelling of anomalous temperatures ($\overline{w}\delta T'$) and the anomalous upwelling of mean temperatures ($w'\overline{\delta T}$).

Temperature and spiciness anomalies

Figure S6 compares the temperature anomaly to the spiciness anomaly both averaged across the bottom surface at 75 m depth. The plots indicate that the temperature anomalies become smaller towards the west, while the spiciness anomalies tend to be evenly distributed along the equator. This is equivalent with an increased ratio of spiciness to temperature anomalies towards the west.

Components of $\overline{w}\delta T'$ heat advection

In Figure S7, we assess the contribution of spiciness anomalies to the $\overline{w}\delta T'$ heat advection. A high correlation between the two is evident in all three regions. The spiciness contribution is smaller than the remaining contribution.

Hovmoeller diagrams of spiciness anomalies

In Figure S8-S10, we show the contributions of spiciness anomalies from different isopycnals to the total spiciness signal averaged across the outcropping area at the 75 m level. The plots indicate that the main contributor the the total signal is the top layer of isopycnals ($< \sigma_{24.5}$). The middle ($\sigma_{24.5}$-$\sigma_{25.5}$) and bottom ($> \sigma_{25.5}$) isopycnal layers have their largest signature during La Niña periods.

Contributions of spiciness anomalies to the total $\overline{w}\delta T'(spic)$ heat advection

Figure S11 shows the contributions of the heat advection by spiciness anomalies of the three isopycnal layers to the total heat advection by spiciness anomalies. Again, the major contributor is the top layer, while the middle and bottom layers have their biggest impact during La Niña periods.

Heat budgets for the different regions

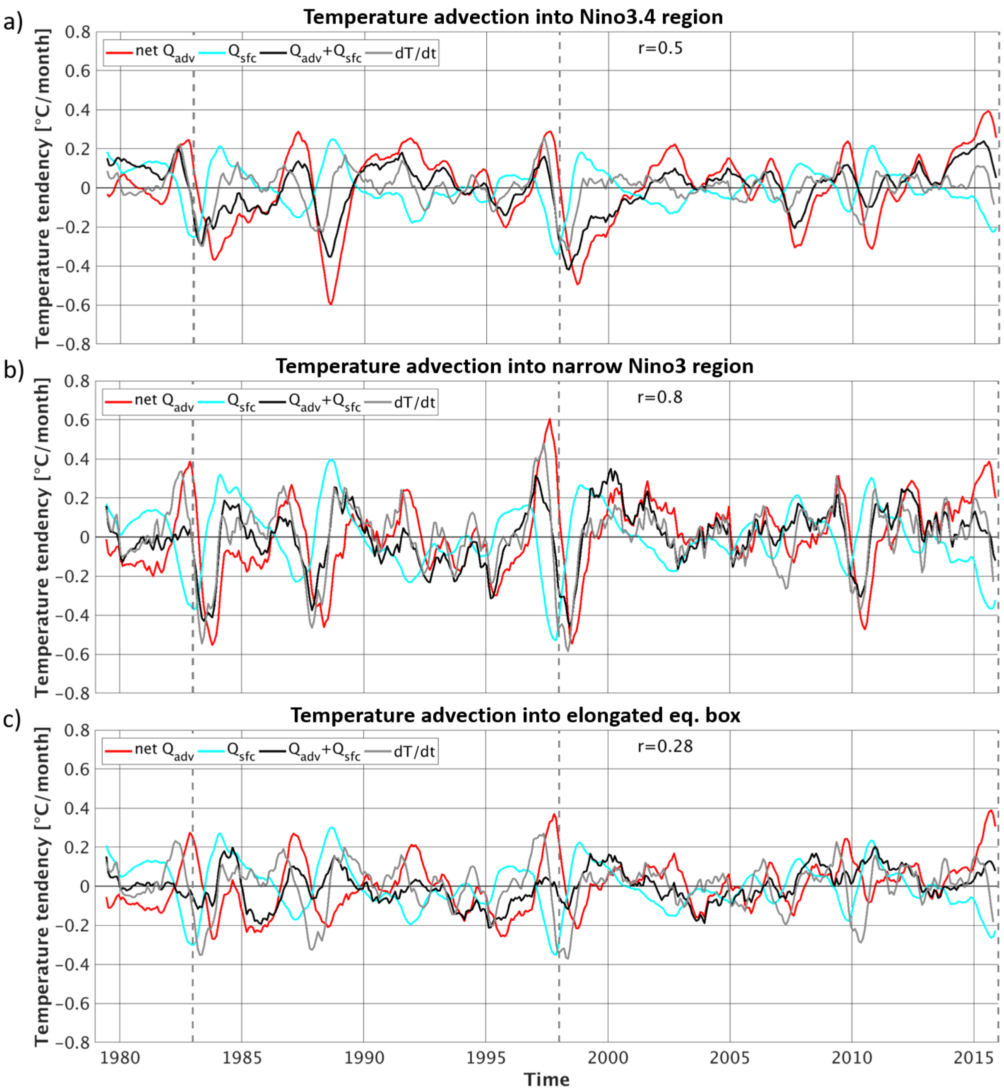

Figure S4.1: Mixed layer heat budget of **a**) the Nino3.4 region, **b**) the narrow Nino3 region, and **c**) the elongated equatorial box. Shown are the temperature tendencies of the box averaged temperature associated with the net surface heat flux (cyan), the net advection (red), and the sum of surface heat flux and advection (black). Also shown is the temperature tendency of the box averaged temperature (grey).

Components of heat advection for the different regions

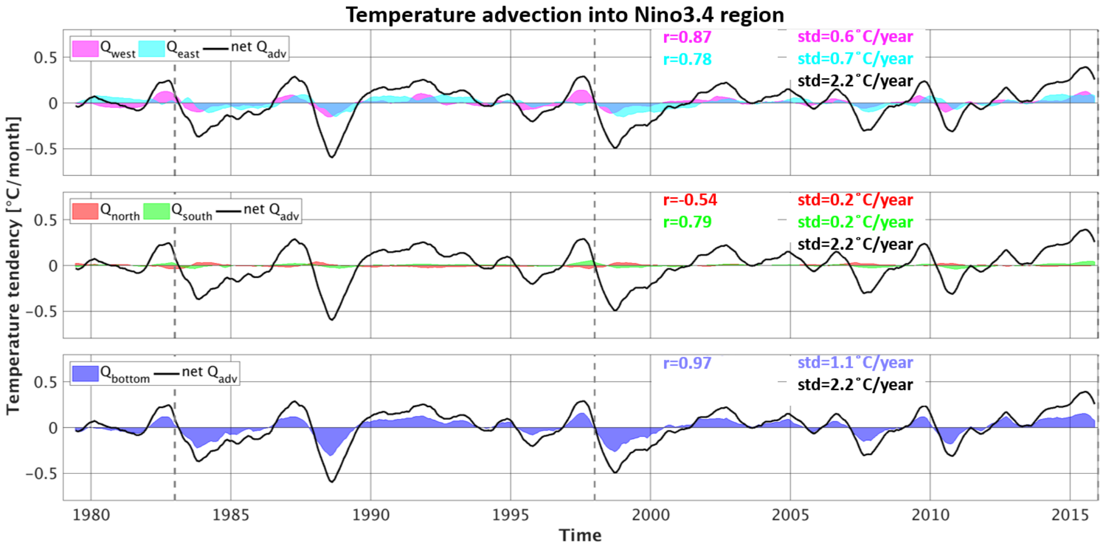

Figure S4.2: Contributions to the heat advection into the mixed layer Nino3.4 region. Shown are the total heat advection (black lines), the contributions through the Western (magenta) and Eastern (cyan) boundaries, the contributions through the Northern (red) and Southern (green) boundaries, and the contribution through the bottom (blue) boundary. The correlation coefficients between the total advection and its individual components as well as the standard deviations are displayed in the plot.

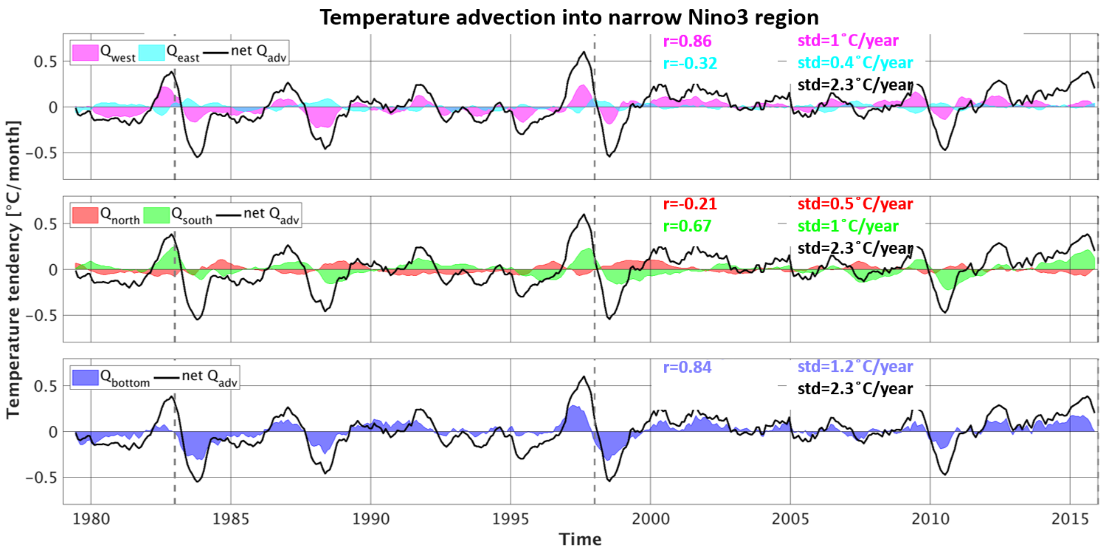

Figure S4.3: Same as Figure S4.4 but for the narrow Nino3 region.

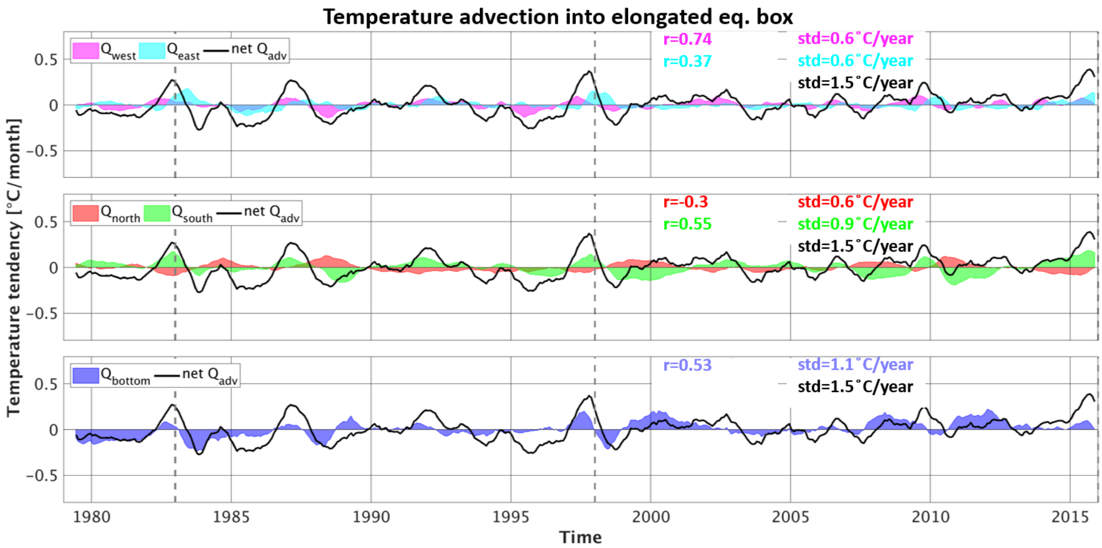

Figure S4.4: Same as Figure S4.4 but for the elongated equatorial region.

Components of vertical heat advection for the different regions

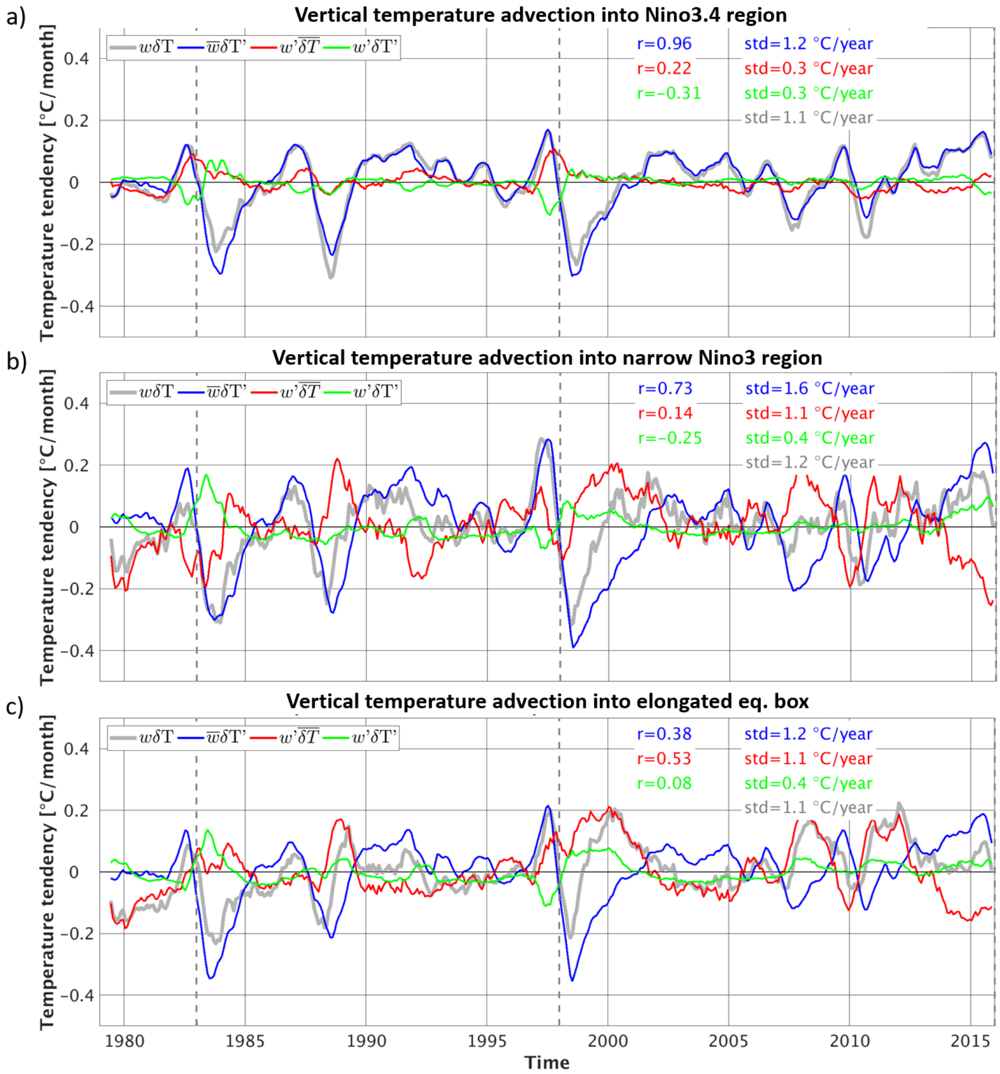

Figure S4.5: Contributions to the vertical heat advection into **a**) the Nino3.4 region, **b**) the narrow Nino3 region, and **c**) the elongated equatorial box. Shown are the total heat advection (grey), the mean advection of anomalous temperature (blue), the anomalous advection of mean temperature (red), and the anomalous advection of anomalous temperature (green). The correlation coefficients between the total vertical advection and its individual components as well as the standard deviations are displayed in the plot.

Temperature and spiciness anomalies for the different regions

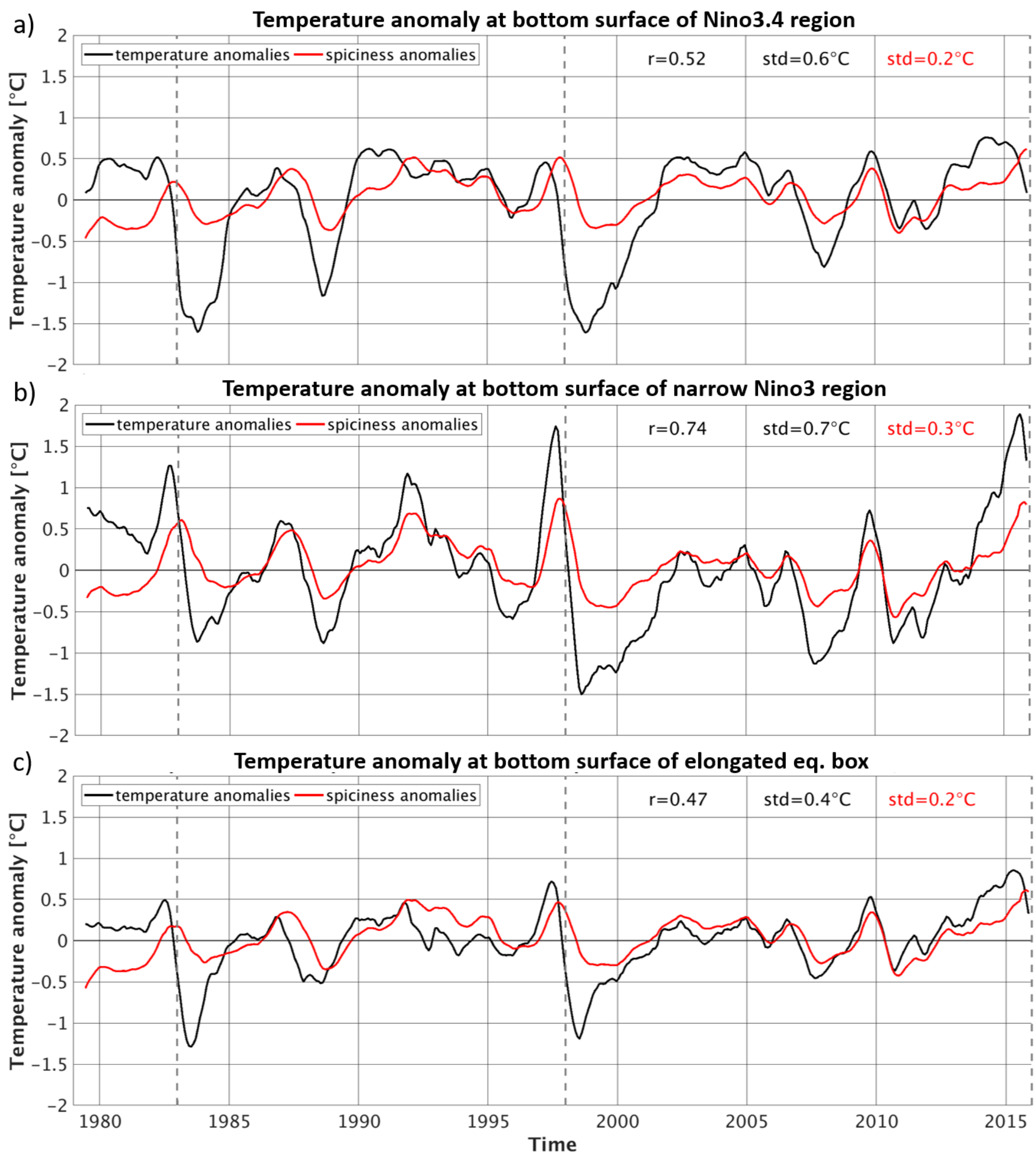

Figure S4.6: Temperature anomalies (black) and spiciness anomalies (red) spatially averaged over the bottom boundary of **a**) the Nino3.4 region, **b**) the narrow Nino3 region, and **c**) the elongated equatorial box at 75 m depth.

Components of $\overline{w}\delta T'$ heat advection for the different regions

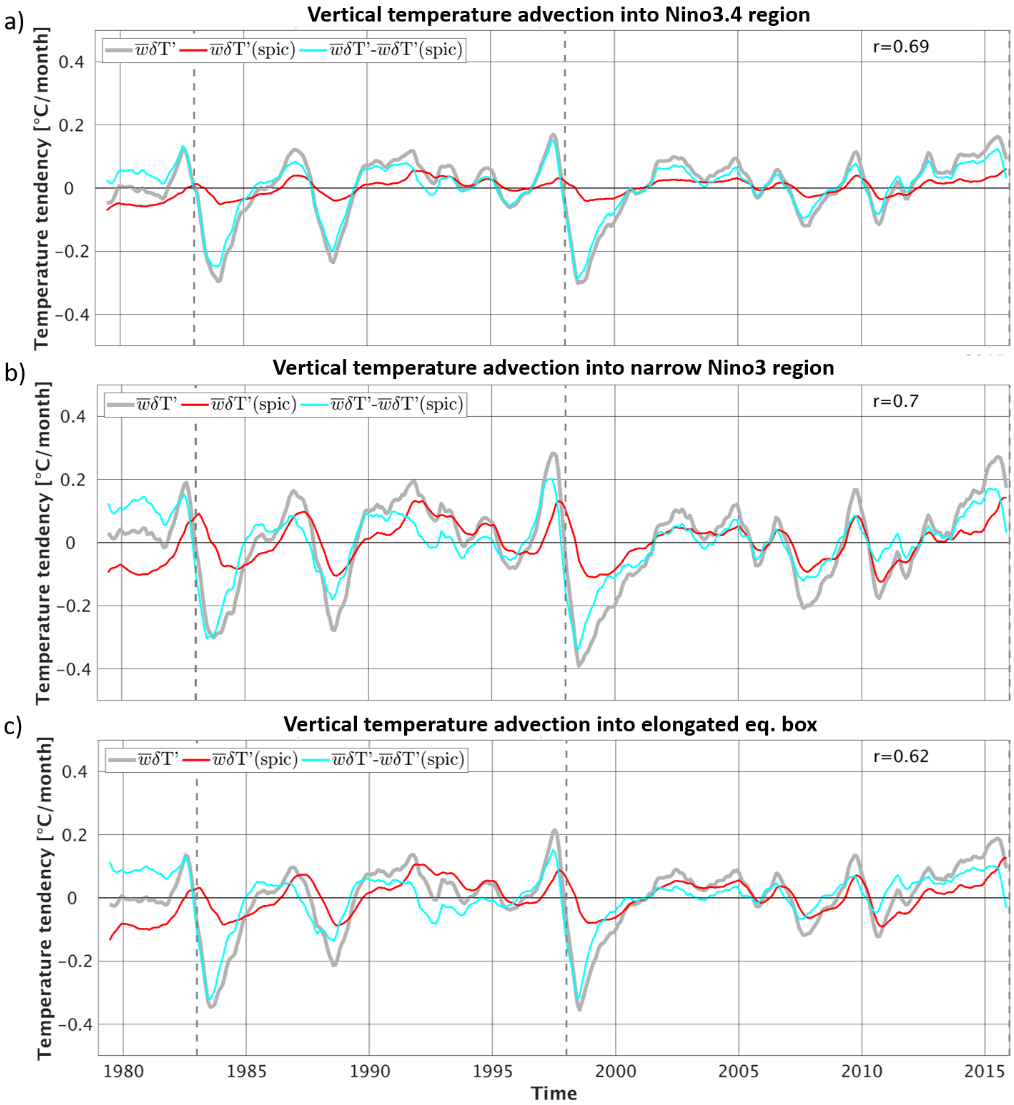

Figure S4.7: Contributions to the total $\overline{w}\delta T'$ heat advection into **a**) the Nino3.4 region, **b**) the narrow Nino3 region, and **c**) the elongated equatorial box. Shown are the total heat advection (grey), the heat advection through spiciness anomalies (red) and the difference between the former two (cyan). The correlation coefficients between the total advection and its spiciness contribution are 0.69, 0.7, and 0.62, respectively.

Hovmoeller diagrams of spiciness anomalies for the different regions

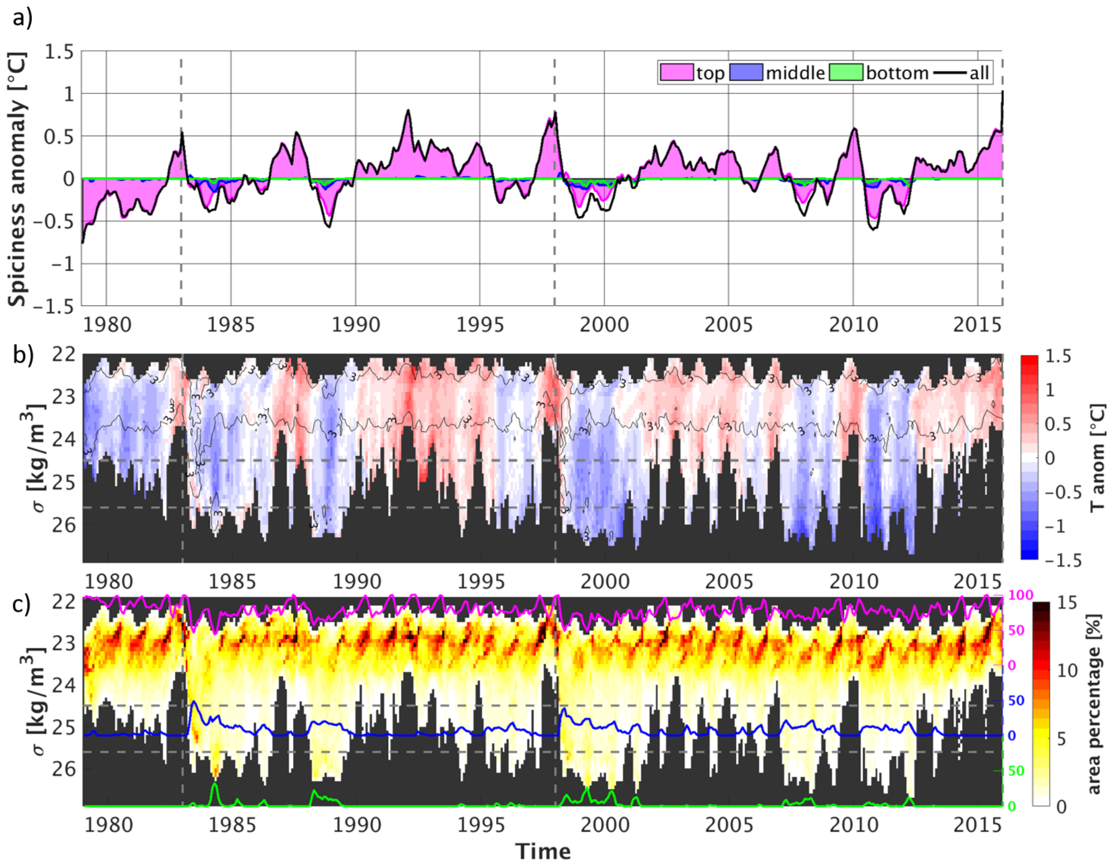

Figure S4.8: Same as Figure 4.8 but for the Nino3.4 region.

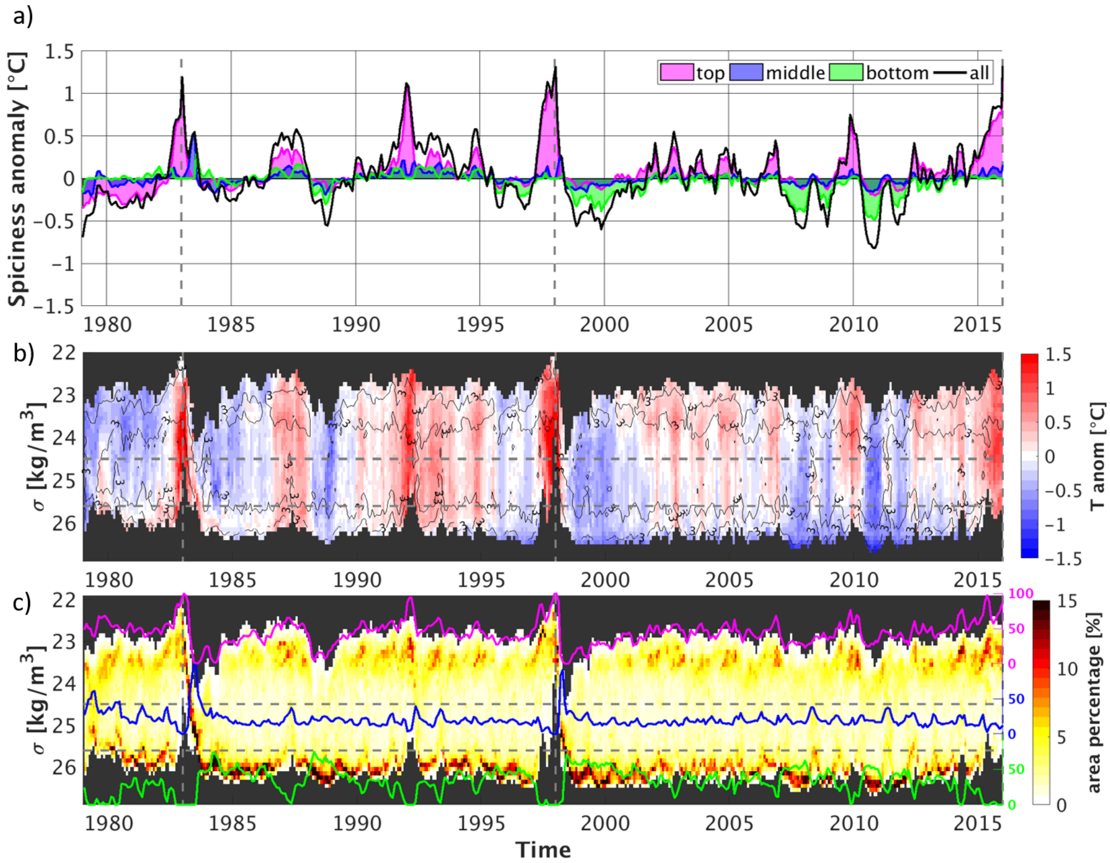

Figure S4.9: Same as Figure 4.8 but for the narrow Nino3 region.

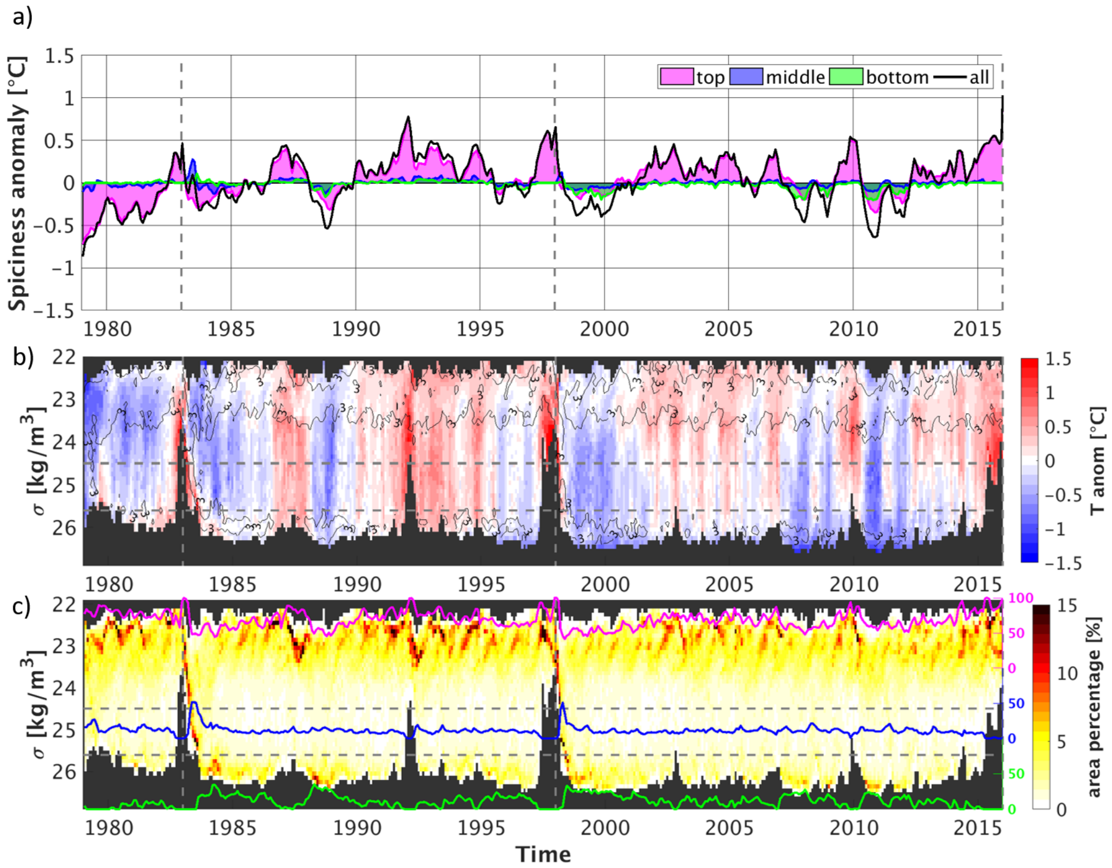

Figure S4.10: Same as Figure 4.8 but for the elongated equatorial region.

Contributions of spiciness anomalies to the total $\overline{w}\delta T'(spic)$ heat advection for the different regions

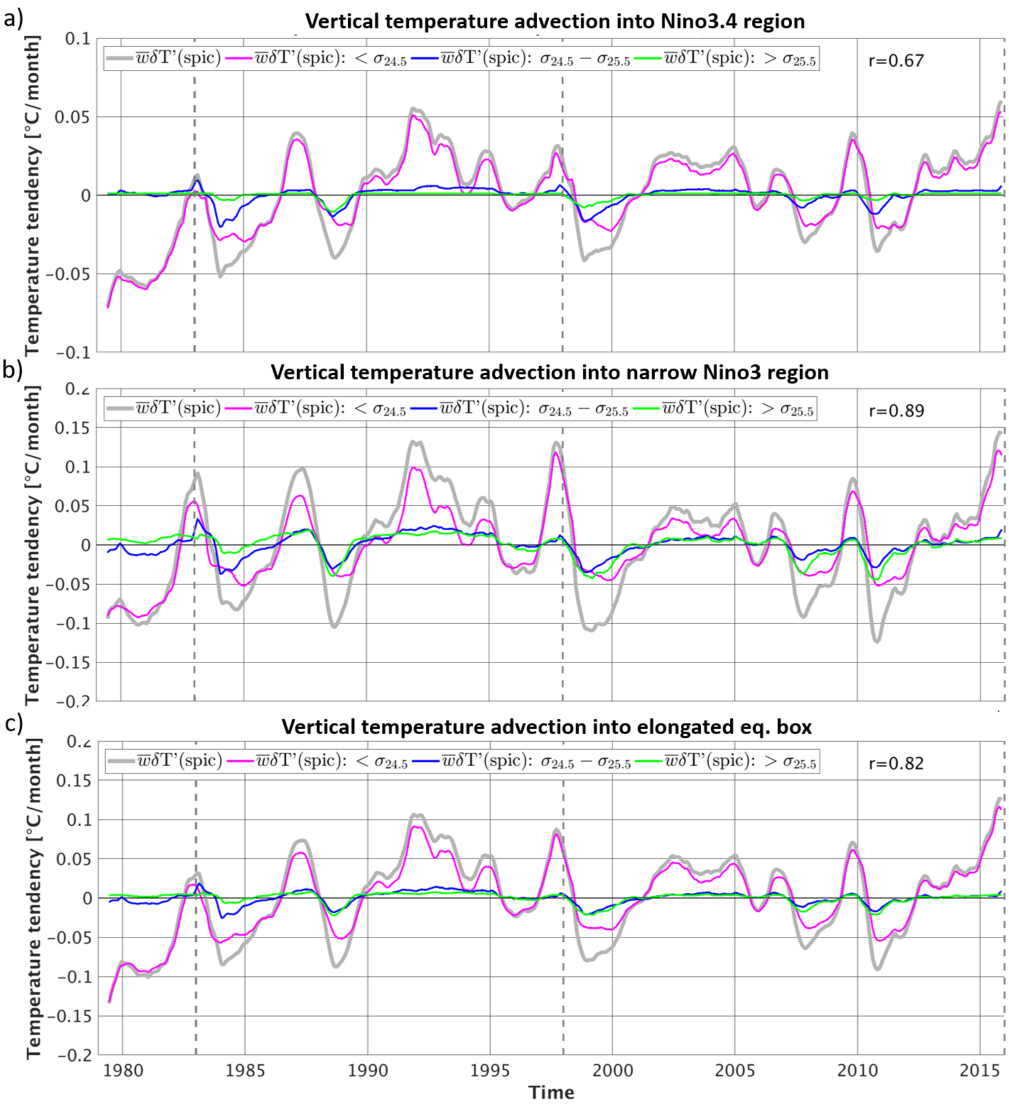

Figure S4.11: Contribution of spiciness anomalies to the total $\overline{w}\delta T'$ heat advection into **a**) the Nino3.4 region, **b**) the narrow Nino3 region, and **c**) the elongated equatorial box. Shown are the total advection through spiciness anomalies (grey) and its contributions by the top (magenta), middle (blue), and bottom (green) isopycnal layers as defined in the text. The correlation coefficients between the total spiciness signal and the contribution by the middle layer of isopycnals are 0.67, 0.89, and 0.82, respectively.

Chapter 5

Discussion and Conclusions

It is commonly agreed that tropical Pacific decadal variability (TPDV) is a product of many processes acting together to generate a low frequency signal that is detectable in various climate variables. These processes can occur both in the tropics locally and remotely in the subtropics and extratropics. While local processes are largely comprised of coupled ocean-atmosphere processes related to ENSO, remote processes include the transportation of a decadal signal into the tropics either via the atmosphere or the ocean. This thesis seeks to advance our knowledge of the oceanic role as a driver of tropical Pacific decadal variability. In the following, we summarise and discuss the findings of each Chapter and include recommendations for future research directions.

5.1 Thesis summary

In Chapter 2 (Zeller et al., 2019), a high-resolution ocean general circulation model (OGCM) was forced by observed winds to investigate the volume transport of the STCs. Applying various subsets of full wind forcing, we could relate the STC variability to the underlying oceanic and atmospheric processes. We find that the STCs are to a large part driven by ENSO related winds (see Section 2.2.3 for the definition of ENSO related winds) on interannual time scales. This suggests a considerable impact of these winds on the tropical climate, given the strong relation between the STC subsurface convergence and equatorial SST (e.g., Izumo 2005; Capotondi et al. 2005). In this study, we further identify three asymmetries between the Northern hemisphere (NH) STC and the Southern hemisphere (SH) STC.

i) The NH STC displays a 26% stronger variability than its SH counterpart on interannual time scales. We show this asymmetry to be equally driven by the two modes of equatorial winds associated with ENSO ($ENSO_{LIN}$ and $ENSO_{NONLIN}$).

ii) The NH STC leads the SH STC by 3 months. Our analysis could trace this lead back to the NH STC surface branch which leads all other STC branches by around 8 months. Further to this, we show that the NH surface branch is mainly forced by the anticyclonic wind stress pattern in the Northeastern tropical Pacific associated with $ENSO_{NONLIN}$. We also show how the time lag between the two STCs affects the role of each STC during El Niño and La Niña events. Specifically, the influence of $ENSO_{NONLIN}$ winds is reflected by a shift of the peak anomalous NH STC changes to 3 months earlier than the SH STC changes which are largely forced by the zonal wind stresses only.

iii) During the recent period (1993-2011), the SH STC exhibits a decadal trend which is twice as strong as the NH STC trend. This is despite the fact that the wind forcing displays quite similar trends in both hemispheres. Our analysis shows that the reason for the reduced NH STC trend is the strong vertical interference occurring at 5°N which is likely induced by the high eddy activity in the form of tropical instability waves (Chen et al. 2015b; Holmes et al. 2018). At 9°N, the reduced STC trend is caused by a reduced increase of the Ekman driven surface branch and by the stronger compensation between interior and western boundary transports. We also demonstrate that as opposed to interannual time scales, sea surface height (SSH) and STC subsurface convergence are not correlated on decadal time scales. This implies that SSH may not be an appropriate proxy for STC transports and therefore decadal changes in tropical climate.

In Chapter 3, we analysed the advection of density compensated temperature anomalies, i.e. spiciness anomalies, with the mean STC transport as a potential contributor to tropical Pacific decadal variability. To this end, we apply a Lagrangian particle simulator with input data from the same OGCM utilised above to track water parcels from the equator backward in time for 10 years. We find that 75% of the water arriving at the equator in the equatorial pycnocline (in the range σ_{22}-σ_{27}) originates from outside the tropics (10°S-10°N), which is in very good agreement with previous findings (e.g., Nie et al. 2019). Further, two thirds of this water, i.e. 50% of the total equatorial water, are sourced from the Southern hemisphere. Consequently, one quarter of the equatorial water comes from the Northern hemisphere, while the remaining quarter is recycled from within the tropics. When monitoring the spiciness anomaly that the water parcels carry, we show that for the warm equatorial spiciness peak in the early 1990s, ~90% of the associated spiciness anomalies originate from the SH. Our results also show that the majority of these SH sourced spiciness anomalies (72%) are propagating via the interior pathways as opposed to via the western boundary pathway. Moreover, spiciness anomalies following the interior pathways in both hemispheres tend to be generated in the region of strongest spiciness variance, which results in strong spiciness anomalies accordingly. Interestingly, when tracking back spiciness anomalies from the negative equatorial peak around the year 2000, the majority of the contributing spiciness anomalies (48%) follow the Northern hemisphere western boundary pathway.

We compared the results for the propagation of water parcels obtained from the different peak experiments against a reference experiment which represents the advection of water parcels during neutral conditions. The comparison shows that the relative importance of the pathways (pathway percentages) for all experiments is within the range of possible percentages derived from 10,000 times randomly subsampling the release dates of the reference experiment. This suggests that the water parcels in all experiments are advected with the same currents, i.e. with the mean circulation. We also tested the sensitivity of our results to the horizontal diffusivity. We find that a change in diffusivity almost exclusively impacts the particles and spiciness anomalies at western boundary but not in the interior. This is assumed to be related to the smaller spatial temperature gradients in the interior as compared to the western boundary which inhibits diffusion even at high diffusivity values.

In Chapter 4, we performed a heat budget analysis of the equatorial Pacific mixed layer using the same OGCM as in the preceding two Chapters. We demonstrated that the advective term of the heat budget equation is dominated by the vertical heat advection through the bottom boundary of the mixed layer which is consistent with previous studies (e.g., Lee et al. 2004; Huang et al. 2012; Boucharel et al. 2015). We then subdivided the vertical heat advection into its mean and anomalous contributions and showed that the total vertical heat advection is dominated by the mean upwelling of anomalous temperature ($\overline{w}\delta T'$). Specifically, during the course of an El Niño event, both the thermocline feedback ($\overline{w}\delta T'$) and the Ekman pumping feedback ($w'\overline{\delta T}$) equally contribute to the build-up phase, while the decay phase is controlled by the thermocline feedback alone. The contribution by the nonlinear advection ($w'T'$) acts as a weak damping to the total vertical heat advection. Our results show that the variance of the vertical heat advection becomes larger in a region confined closer to the equator and further to the east. This is consistent with expectations as the mean and anomalous upwelling become larger towards the equator, while the mean upwelling has its maximum in the eastern equatorial Pacific.

To quantify the contribution of spiciness anomalies to the total vertical heat advection, we further subdivide the anomalous temperatures utilised in the $\overline{w}\delta T'$ mechanism into its spiciness anomaly and remaining part. This analysis reveals that $\sim$30% of the $\overline{w}\delta T'$ heat advection arise from the mean upwelling of spiciness anomalies in the Nino3 region and $\sim$25% in the Nino3.4 region. This number even increases to about 67% when confining the region closer to the equator. This enhanced spiciness influence towards the equator is due to a higher ratio of spiciness versus temperature anomalies closer to the equator. While temperature anomalies clearly decrease towards the western equatorial Pacific, spiciness anomalies remain broadly constant along the equator. We additionally distinguish between locally and remotely generated spiciness anomalies by isolating the $\sigma_{24.5}$-$\sigma_{25.5}$ isopycnal range which was shown to be the carrier of subtropically generated spiciness anomalies (see Chapter 3). The contribution of remotely generated spiciness anomalies to the total vertical heat advection is 23% (std) in the Nino3 region with a decreasing tendency towards the western equatorial Pacific. This decrease is due to the fact that the outcropping region of the $\sigma_{24.5}$-$\sigma_{25.5}$ isopycnal range is mostly confined to the central and eastern equatorial Pacific. Finally, we also detect a time dependence of the importance of spiciness anomalies with spiciness anomalies having a considerably larger impact during La Niña periods when the uplifted thermocline in the eastern equatorial Pacific increases the area of outcropping of the respective isopycnals. This result suggests an increased importance of La Niña periods with regard to the impact of spiciness anomalies on the tropical Pacific decadal variability.

5.2 Key Findings

The key findings of the thesis can be summarised as follows:

- On interannual time scales, the STCs are to a large part driven by winds that are related to ENSO (both linearly and nonlinearly). Given that the STCs provide two mechanisms of inducing decadal variability to the tropical Pacific, ENSO appears to share a prominent portion in changing its own background state.

- On decadal time scales, recent tropical Pacific STC changes and any related SST changes (1992-2011) are dominated by changes in the Southern hemisphere. This is due to a cancellation of the decadal trend in the Northern hemisphere STC branches. It is unclear how representative the trends in the recent period are of the past, but our results suggests that accurate monitoring of the STC strength is required in both hemispheres and raises questions about SSH as a proxy of STC strength.

- Spiciness anomalies can potentially act as an important contributor to large decadal temperature anomalies at the equatorial Pacific. The preferred pathway of remotely generated spiciness anomalies to the equator depends on their sign. While warm spiciness anomalies predominantly propagate via the SH interior, cool spiciness anomalies tend to propagate via the NH western boundary. Keeping in mind that the sample size is very small, we cannot tell if the disparity in the preferred pathways is genuine or just an artefact.

- Remotely generated spiciness anomalies have a small but detectable impact (5%) on the equatorial Pacific mixed layer heat budget. Their impact is particularly discernible during La Niña periods when the isopycnals carrying the spiciness anomalies outcrop in the eastern equatorial Pacific.

5.3 Thesis Overarching Discussion

Seeking to identify the ocean's role transporting and inducing tropical Pacific decadal variability, in this thesis we investigated the meridional oceanic transports that connect the subtropical to the tropical Pacific Ocean. It has to be kept in mind that while various studies have focused on the integrated upper ocean mass exchanges (e.g., Kug et al. 2003; McGregor et al. 2014a) that are used to determine changes in upper ocean warm water volume related to ENSO, the focus of this thesis is the overturning transport of the STCs, which is a fundamentally different process. The STCs are related to the equatorial upwelling and are usually used to examine decadal changes in the tropical Pacific. Traditionally, mechanisms proposed to generate TPDV are either i) confined to the equatorial Pacific region and related to ENSO occurrences, or ii) related to the transport of decadal signals from the subtropics or the extratropics to the equator. Our finding that a large portion of the STC variability is driven by ENSO related winds raises an interesting further addition to TPDV mechanisms by combining the two previously mentioned concepts and arguing that ENSO itself can be responsible for the advection of decadal signals from remote regions.

The hemispheric asymmetries in STC transports that have been revealed in Chapter 2 and the associated wind patterns driving these asymmetries also add new insights to the current state of knowledge about the role of the STCs in changing tropical Pacific climate through the $w'\overline{T}$ mechanism. Particularly in consideration of the large difference in mean pycnocline temperatures between the NH (17°C-22°C) and SH (21°C-24°C), our results suggest that a change in the asymmetric STC transport contribution to the equatorial undercurrent can have a strong impact on tropical Pacific climate.

In part, these new insights support previous findings. E.g., Kug et al. (2003) and McGregor et al. (2014a) who also find stronger integrated upper ocean transport variations. Moreover, the lead-lag relationship between Northern and Southern hemisphere transports has been mentioned by Ishida et al. (2008). Again, in their study the authors consider the upper ocean integral of meridional transports as opposed to STC transports. In terms of the low-frequency STC changes, we ascribe a prominent role to the Southern hemisphere. Interestingly, Luo and Yamagata (2001) also emphasise the contribution of the South Pacific to TPDV, however, based on the mean advection of anomalous temperature.

In part our findings add much needed detail to the results of previous studies. E.g., Ishida et al. (2008) trace the lead-lag relationship back to a lag between the NH WBC and NH interior transports. However, in the present work we distinguish between surface and subsurface interior transports, such that we can attribute the out-of-phase relationship to the NH surface transport which leads the subsurface interior transport. In contrast to Ishida et al. (2008), our results indicate that the western boundary and subsurface transports are anti-correlated both in the Northern and in the Southern hemisphere. Furthermore, our finding that sea surface height (SSH) is not well corresponding to STC transports on decadal time scales questions the use of SSH as an indicator for STC strength as has been done before (e.g., Feng et al. 2010)

We are aware that the definition of the STC branches may slightly affect the results in Chapter 2. However, various tests have shown that our definition, in particular the definition of the Northern hemisphere western boundary current, is the physically most meaningful and provides a good foundation for our analysis.

In regard to the advection of spiciness anomalies (Chapter 3), our results support the studies that propose an increased influence of the interior over the western boundary pathways (Li et al. 2012; Thomas and Fedorov 2017) while they controvert other studies that stress the role of the western boundary pathways (Giese et al. 2002; Yeager and Large 2004). The biggest limitation for this study is the missing diapycnal diffusion. Earlier studies have shown that diapycnal diffusion may have a considerable impact on spiciness anomalies (Johnson 2006).

It also has to be kept in mind that the length of the model simulations only allows us to investigate decadal changes on a limited time period. Because of that, we could only consider one decadal trend in STC transports (Chapter 2) and could identify only 3 decadal peaks in spiciness (Chapter 3). We therefore cannot claim statistical robustness for the decadal results while still being able to reveal various characteristics of STC changes and spiciness advection for the time period analysed.

It is striking that, within the limitations of our study, both the $v'\overline{T}$ mechanism (Chapter 2) and the "spiciness mechanism" (Chapter3) are dominated by the influence of the Southern hemisphere. This may open up new avenues for obtaining improved predictions of tropical Pacific decadal variability.

5.4 Future Research Directions

As stated in the discussion section (section 5.3) of this thesis, the asymmetric changes in decadal STC transports in combination with the large hemispheric difference in mean pycnocline temperatures can generate TPDV by a changing ratio of the NH to SH contribution to the equatorial waters. A future study could quantify the impact of these changes in STC strength on TPDV by examining the associated meridional heat transports by the STCs.

Numerous studies have concluded that the $\overline{v}T'$ mechanism from the North Pacific to the equator is not an effective means of inducing TPDV (e.g., Schneider et al. 1999b; Hazeleger et al. 2001b). However, subsequent studies have shown that in the Southern hemisphere this mechanism is a valid contributor to TPDV (e.g., Luo and Yamagata 2001; Giese et al. 2002). Knowing about the distinctive mechanism of spiciness generation as opposed to the generation of subducted temperature anomalies, it would be interesting to look at the relative importance of spiciness anomalies for the Southern hemispheric $\overline{v}T'$ transport.

This could be done by applying a coupled ocean-atmosphere general circulation model which would allow for the generation of surface temperature anomalies in the subtropics that are then subducted. The subducted temperature anomalies would then have to be quantitatively compared to the spiciness anomalies. A coupled ocean-atmosphere model would also allow for feedbacks to the equatorial emergence of spiciness anomalies. This inclusion would help to further explore the impact of spiciness anomalies on TPDV and would be a valuable review study to the former work by Schneider (2004) who used a low resolution coupled model.

Applying an ocean only model, a way of further investigating the role of oceanic subtropical to tropical exchanges is to implement "virtual walls" at the Northern and Southern borders of the tropical Pacific. In these "wall regions", temperature and salinity could be set to climatological values. Thus, by comparing the output of such simulations to a control simulation, the importance of subtropical oceanic signals can be determined. A further idea to this is that the temperature and salinity in the "wall regions" could be set to some perturbed value as this would allow for a more direct assessment of the spiciness anomalies generating Pacific decadal variability.

We have shown that for the positive spiciness peak the SH interior pathway was the dominant contributor while for the negative spiciness peak it was the NH western boundary pathway. It remains an open question what makes one source region and pathway more relevant than others at different times. In this regard it would be very insightful to re-perform the Lagrangian particle simulations with diapycnal diffusion applied. It is also unclear whether this short term assessment is relevant on the long term. As we are currently entering a positive phase of the PDO, it would be enlightening to repeat the analysis once we have a clear spiciness peak at the equator, to see if and how the pathways of the associated spiciness anomalies differ.

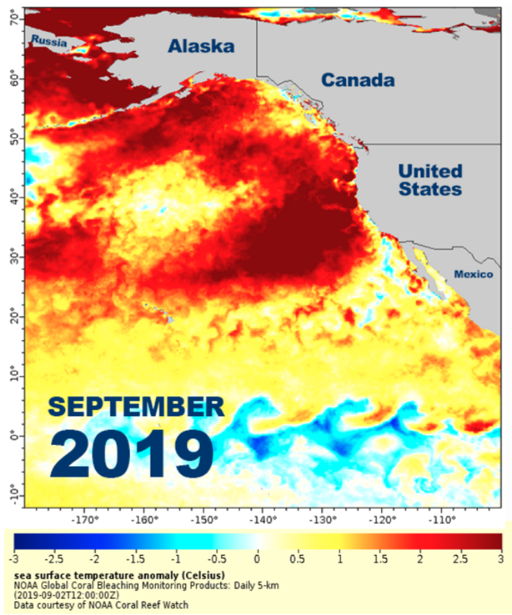

Figure 5.1: Snapshot of North Pacific sea surface temperature anomaly (°C) on 02 Sep 2019. Data courtesy of NOAA Coral Reef Watch.

Just now, in September 2019, a massive heat anomaly has developed in the Northeastern extratropical Pacific (Figure 5.1) which is exactly the region of strongest spiciness variance as shown in Chapter 3. While it is unclear yet how deep this heat anomaly goes it will be intriguing to investigate the potentially associated spiciness generation and its advection to the equator and impact on TPDV. These questions remain in the scope of future research.

References

Alexander, M. (2010). Extratropical air-sea interaction, sea surface temperature variability, and the pacific decadal oscillation. *Geophysical Monograph Series*, 189:123–148.

Alexander, M., Bladé, I., Newman, M., Lanzante, J., Lau, N.-C., and Scott, J. (2002). The atmospheric bridge: The influence of ENSO teleconnections on air-sea interaction over the global oceans. *Journal of Climate*, 15(16):2205–2231.

Alexander, M., Deser, C., and Timlin, M. (1999). The reemergence of SST anomalies in the North Pacific Ocean. *Journal of Climate*, 12(8 PART 1):2419–2433.

Alexander, M., Matrosova, L., Penland, C., Scott, J., and Chang, P. (2008). Forecasting Pacific SSTs: Linear inverse model predictions of the PDO. *Journal of Climate*, 21(2):385–402.

Alory, G. and Delcroix, T. (2002). Interannual sea level changes and associated mass transports in the tropical Pacific from TOPEX/Poseidon data and linear model results (1964–1999). *Journal of Geophysical Research: Oceans*, 107(C10):17–1–17–22.

Barnett, T., Pierce, D., Latif, M., Dommenget, D., and Saravanan, R. (1999). Interdecadal interactions between the tropics and midlatitudes in the Pacific basin. *Geophysical Research Letters*, 26(5):615–618.

Blanke, B. and Raynaud, S. (1997). Kinematics of the pacific equatorial undercurrent: An eulerian and lagrangian approach from gcm results. *Journal of Physical Oceanography*, 27(6):1038–1053.

Bond, N., Overland, J., Spillane, M., and Stabeno, P. (2003). Recent shifts in the state of the North Pacific. *Geophysical Research Letters*, 30(23):CLM 1–1 – CLM 1–4.

Bosc, C. and Delcroix, T. (2008). Observed equatorial Rossby waves and ENSO-related warm water volume changes in the equatorial Pacific Ocean. *Journal of Geophysical Research: Oceans*, 113(6).

Boucharel, J., Timmermann, A., Santoso, A., England, M., Jin, F.-F., and Balmaseda, M. (2015). A surface layer variance heat budget for ENSO. *Geophysical Research Letters*, 42(9):3529–3537.

Butt, J. and Lindstrom, E. (1994). Currents off the east coast of New Ireland, Papua New Guinea, and their relevance to regional undercurrents in the western equatorial Pacific Ocean. *Journal of Geophysical Research*, 99(C6):12 503–12 514.

Capotondi, A., Alexander, M., Deser, C., and McPhaden, M. (2005). Anatomy and decadal evolution of the Pacific Subtropical-Tropical Cells (STCs). *Journal of Climate*, 18(18):3739–3758.

Chen, H.-C., Sui, C.-H., Tseng, Y.-H., and Huang, B. (2015a). An analysis of the linkage of pacific subtropical cells with the recharge-discharge processes in ENSO evolution. *Journal of Climate*, 28(9):3786–3805.

Chen, X., Qiu, B., Chen, S., Qi, Y., and Du, Y. (2015b). Seasonal eddy kinetic energy modulations along the North Equatorial Countercurrent in the western Pacific. *Journal of Geophysical Research: Oceans*, 120(9):6351–6362.

Cheng, W., McPhaden, M., Zhang, D., and Metzger, E. (2007). Recent changes in the Pacific subtropical cells inferred from an eddy-resolving ocean circulation model. *Journal of Physical Oceanography*, 37(5):1340–1356.

Chiang, J. and Sobel, A. (2002). Tropical tropospheric temperature variations caused by ENSO and their influence on the remote tropical climate. *Journal of Climate*, 15(18):2616–2631.

Chikamoto, Y., Kimoto, M., Watanabe, M., Ishii, M., and Mochizuki, T. (2012). Relationship between the Pacific and Atlantic stepwise climate change during the 1990s. *Geophysical Research Letters*, 39(21).

Chikamoto, Y., Mochizuki, T., Timmermann, A., Kimoto, M., and Watanabe, M. (2016). Potential tropical Atlantic impacts on Pacific decadal climate trends. *Geophysical Research Letters*, 43(13):7143–7151.

Collins, M., An, S.-I., Cai, W., Ganachaud, A., Guilyardi, E., Jin, F.-F., Jochum, M., Lengaigne, M., Power, S., Timmermann, A., Vecchi, G., and Wittenberg, A. (2010). The impact of global warming on the tropical Pacific Ocean and El Nino. *Nature Geoscience*, 3(6):391–397.

Davis, R., Kessler, W., and Sherman, J. (2012). Gliders measure western boundary current transport from the south pacific to the equator. *Journal of Physical Oceanography*, 42(11):2001–2013.

Dee, D. and Uppala, S. (2009). Variational bias correction of satellite radiance data in the ERA-Interim reanalysis. *Quarterly Journal of the Royal Meteorological Society*, 135(644):1830–1841.

Delworth, T., Rosati, A., Anderson, W., Adcroft, A., Balaji, V., Benson, R., Dixon, K., Griffies, S., Lee, H.-C., Pacanowski, R., Vecchi, G., Wittenberg, A., Zeng, F., and Zhang, R. (2012). Simulated climate and climate change in the GFDL CM2.5 high-resolution coupled climate model. *Journal of Climate*, 25(8):2755–2781.

Deser, C., Phillips, A., and Hurrell, J. (2004). Pacific interdecadal climate variability: Linkages between the tropics and the North Pacific during boreal winter since 1900. *Journal of Climate*, 17(16):3109–3124.

Deser, C., Simpson, I., McKinnon, K., and Phillips, A. (2017). The Northern Hemisphere extratropical atmospheric circulation response to ENSO: How well do we know it and how do we evaluate models accordingly? *Journal of Climate*, 30(13):5059–5082.

Di Lorenzo, E., Liguori, G., Schneider, N., Furtado, J., Anderson, B., and Alexander, M. (2015). ENSO and meridional modes: A null hypothesis for Pacific climate variability. *Geophysical Research Letters*, 42(21):9440–9448.

Enfield, D. and Allen, J. (1980). On the Structure and Dynamics of Monthly Mean Sea Level Anomalies along the Pacific Coast of North and South America. *Journal of Physical Oceanography*.

England, M., Mcgregor, S., Spence, P., Meehl, G., Timmermann, A., Cai, W., Gupta, A., Mcphaden, M., Purich, A., and Santoso, A. (2014). Recent intensification of wind-driven circulation in the Pacific and the ongoing warming hiatus. *Nature Climate Change*, 4(3):222–227.

Farneti, R., Dwivedi, S., Kucharski, F., Molteni, F., and Griffies, S. (2014a). On Pacific subtropical cell variability over the second half of the twentieth century. *Journal of Climate*, 27(18):7102–7112.

Farneti, R., Molteni, F., and Kucharski, F. (2014b). Pacific interdecadal variability driven by tropical-extratropical interactions. *Climate Dynamics*, 42(11-12):3337–3355.

Fedorov, A. and Philander, S. (2000). Is El Nino changing? *Sience*, 288(80).

Fedorov, A. and Philander, S. (2001). A stability analysis of tropical ocean-atmosphere interactions: Bridging measurements and theory for El Niño. *Journal of Climate*, 14(14):3086–3101.

Feng, M., McPhaden, M., and Lee, T. (2010). Decadal variability of the Pacific subtropical cells and their influence on the southeast Indian Ocean. *Geophysical Research Letters*, 37(9).

Folland, C., Renwick, J., Salinger, M., and Mullan, A. (2002). Relative influences of the Interdecadal Pacific Oscillation and ENSO on the South Pacific Convergence Zone. *Geophysical Research Letters*, 29(13):21–1 – 21–4.

Freund, M., Henley, B., Karoly, D., McGregor, H., Abram, N., and Dommenget, D. (2019). Higher frequency of Central Pacific El Niño events in recent decades relative to past centuries. *Nature Geoscience*, 12(6):450–455.

Giese, B., Urizar, S., and Fučkar, N. (2002). Southern hemisphere origins of the 1976 climate shift. *Geophysical Research Letters*, 29(2):1–1.

Gordon, A., Susanto, R., and Ffield, A. (1999). Throughflow within Makassar Strait. *Geophysical Research Letters*, 26(21):3325–3328.

Grimm, A. (2003). The El Niño impact on the summer monsoon in Brazil: Regional processes versus remote influences. *Journal of Climate*, 16(2):263–280.

Gu, D. and Philander, S. (1997). Interdecadal climate fluctuations that depend on exchanges between the tropics and extratropics. *Science*, 275(5301):805–807.

Hanawa, K. and Sugimoto, S. (2004). 'Reemergence' areas of winter sea surface temperature anomalies in the world's oceans. *Geophysical Research Letters*, 31(10):L10303 1–4.

Hare, S. and Mantua, N. (2000). Empirical evidence for north pacific regime shifts in 1977 and 1989. *Progress in Oceanography*, 47(2-4):103–145.

Hazeleger, W., De Vries, P., and Van Oldenborgh, G. (2001a). Do tropical cells ventilate the Indo-Pacific equatorial thermocline. *Geophysical Research Letters*, 28(9):1763–1766.

Hazeleger, W., Seager, R., Cane, M., and Naik, N. (2004). How can tropical Pacific Ocean heat transport vary? *Journal of Physical Oceanography*, 34(1):320–333.

Hazeleger, W., Visbeck, M., Cane, M., Karspeck, A., and Naik, N. (2001b). Decadal upper ocean temperature variability in the tropical Pacific. *Journal of Geophysical Research: Oceans*, 106(C5):8971–8988.

Henley, B. (2017). Pacific decadal climate variability: Indices, patterns and tropical-extratropical interactions. *Global and Planetary Change*, 155:42–55.

Henley, B., Gergis, J., Karoly, D., Power, S., Kennedy, J., and Folland, C. (2015). A Tripole Index for the Interdecadal Pacific Oscillation. *Climate Dynamics*, 45(11-12):3077–3090.

Holmes, R., McGregor, S., Santoso, A., and England, M. (2018). Contribution of tropical instability waves to ENSO irregularity. *Climate Dynamics*.

Hong, L., Zhang, L., Chen, Z., and Wu, L. (2014). Linkage between the Pacific Decadal Oscillation and the low frequency variability of the Pacific Subtropical Cell. *Journal of Geophysical Research: Oceans*, 119(6):3464–3477.

Horel, J. and Wallace, J. (1981). Planetary-scale atmospheric phenomena associated with the Southern Oscillation. *Monthly Weather Review*, 109(4):813–829.

Huang, B., Xue, Y., Wang, H., Wang, W., and Kumar, A. (2012). Mixed layer heat budget of the El Niño in NCEP climate forecast system. *Climate Dynamics*, 39(1-2):365–381.

Ineson, S. and Scaife, A. (2009). The role of the stratosphere in the European climate response to El Nino. *Nature Geoscience*, 2(1):32–36.

Ishida, A., Kashino, Y., Hosoda, S., and Ando, K. (2008). North-south asymmetry of warm water volume transport related with El Niño variability. *Geophysical Research Letters*, 35(18).

Izumo, T. (2005). The equatorial undercurrent, meridional overturning circulation, and their roles in mass and heat exchanges during El Niño events in the tropical Pacific ocean. *Ocean Dynamics*, 55(2):110–123.

Izumo, T., Lengaigne, M., Vialard, J., Suresh, I., and Planton, Y. (2019). On the physical interpretation of the lead relation between warm water volume and the el niño southern oscillation. *Climate Dynamics*, 52(5-6):2923–2942.

Izumo, T., Picaut, J., and Blanke, B. (2002). Tropical pathways, equatorial undercurrent variability and the 1998 La Niña. *Geophysical Research Letters*, 29(22):37–1.

Jin, F.-F. (1997). An equatorial ocean recharge paradigm for ENSO. Part I: Conceptual model. *Journal of the Atmospheric Sciences*, 54(7):811–829.

Johnson, G. (2001). The Pacific Ocean subtropical cell surface limb. *Geophysical Research Letters*, 28(9):1771–1774.

Johnson, G. (2006). Generation and initial evolution of a mode water θ-S anomaly. *Journal of Physical Oceanography*, 36(4):739–751.

Johnson, G. and McPhaden, M. (1999). Interior pycnocline flow the subtropical to the Equatorial Pacific Ocean. *Journal of Physical Oceanography*, 29(12):3073–3089.

Kleeman, R., McCreary Jr., J., and Klinger, B. (1999). A mechanism for generating ENSO decadal variability. *Geophysical Research Letters*, 26(12):1743–1746.

Klinger, B., McCreary Jr, J., and Kleeman, R. (2002). The relationship between oscillating subtropical wind stress and equatorial temperature. *Journal of Physical Oceanography*, 32(5):1507–1521.

Kosaka, Y. and Xie, S.-P. (2013). Recent global-warming hiatus tied to equatorial Pacific surface cooling. *Nature*, 501(7467):403–407.

Kosaka, Y. and Xie, S.-P. (2016). The tropical Pacific as a key pacemaker of the variable rates of global warming. *Nature Geoscience*, 9(9):669–673.

Kug, J.-S., Kang, I.-S., and An, S.-I. (2003). Symmetric and antisymmetric mass exchanges between the equatorial and off-equatorial Pacific associated with ENSO. *Journal of Geophysical Research C: Oceans*, 108(8):40–1.

Kwon, Y.-O., Deser, C., and Cassou, C. (2011). Coupled atmosphere-mixed layer ocean response to ocean heat flux convergence along the Kuroshio Current Extension. *Climate Dynamics*, 36(11-12):2295–2312.

Lange, M. and Sebille, E. (2017). Parcels v0.9: Prototyping a Lagrangian ocean analysis framework for the petascale age. *Geoscientific Model Development*, 10(11):4175–4186.

Large, W. and Yeager, S. (2009). The global climatology of an interannually varying air - Sea flux data set. *Climate Dynamics*, 33(2-3):341–364.

Latif, M. and Barnett, T. (1995). Interactions of the tropical oceans. *Journal of Climate*, 8(4):952–964.

Lee, T. and Fukumori, I. (2003). Interannual-to-decadal variations of tropical-subtropical exchange in the Pacific Ocean: Boundary versus interior pycnocline transports. *Journal of Climate*, 16(24):4022–4042.

Lee, T., Fukumori, I., and Tang, B. (2004). Temperature advection: Internal versus external processes. *Journal of Physical Oceanography*, 34(8):1936–1944.

Lee, T. and McPhaden, M. (2008). Decadal phase change in large-scale sea level and winds in the Indo-Pacific region at the end of the 20th century. *Geophysical Research Letters*, 35(1).

Lengaigne, M., Boulanger, J.-P., Menkes, C., and Spencer, H. (2006). Influence of the seasonal cycle on the termination of el niño events in a coupled general circulation model. *Journal of Climate*, 19(9):1850–1868.

L'Heureux, M. and Thompson, D. (2006). Observed relationships between the El-Niño-Southern oscillation and the extratropical zonal-mean circulation. *Journal of Climate*, 19(1):276–287.

Li, Y., Wang, F., and Sun, Y. (2012). Low-frequency spiciness variations in the tropical Pacific Ocean observed during 2003-2012. *Geophysical Research Letters*, 39(23).

Liu, Z., Philander, S., and Pacanowski, R. (1994). A GCM study of tropical-subtropical upper-ocean water exchange. *Journal of Physical Oceanography*, 24(12):2606–2623.

Lohmann, K. and Latif, M. (2005). Tropical Pacific decadal variability and the subtropical-tropical cells. *Journal of Climate*, 18(23):5163–5178.

Lu, P. and McCreary Jr, J. (1995). Influence of the ITCZ on the flow of thermocline water from the subtropical to the equatorial Pacific Ocean. *Journal of Physical Oceanography*, 25(12):3076–3088.

Luo, J.-J. and Yamagata, T. (2001). Long-term El Niño-Southern Oscillation (ENSO)-like variation with special emphasis on the South Pacific. *Journal of Geophysical Research: Oceans*, 106(C10):22211–22227.

Lübbecke, J., Böning, C., and Biastoch, A. (2008). Variability in the subtropical-tropical cells and its effect on near-surface temperature of the equatorial Pacific: A model study. *Ocean Science*, 4(1):73–88.

Mantua, N., Hare, S., Zhang, Y., Wallace, J., and Francis, R. (1997). A Pacific Interdecadal Climate Oscillation with Impacts on Salmon Production. *Bulletin of the American Meteorological Society*, 78(6):1069–1079.

McCreary Jr, J. and Lu, P. (1994). Interaction between the subtropical and equatorial ocean circulations: the subtropical cell. *Journal of Physical Oceanography*, 24(2):466–497.

McGregor, S., Gupta, A., and England, M. (2012a). Constraining wind stress products with sea surface height observations and implications for Pacific Ocean sea level trend attribution. *Journal of Climate*, 25(23):8164–9176.

McGregor, S., Spence, P., Schwarzkopf, F., England, M., Santoso, A., Kessler, W., Timmermann, A., and Böning, C. (2014a). ENSO-driven interhemispheric Pacific mass transports. *Journal of Geophysical Research C: Oceans*, 119(9):6221–6237.

McGregor, S., Stuecker, M., Kajtar, J., England, M., and Collins, M. (2018). Model tropical Atlantic biases underpin diminished Pacific decadal variability. *Nature Climate Change*.

McGregor, S., Timmermann, A., Schneider, N., Stuecker, M., and England, M. (2012b). The effect of the south pacific convergence zone on the termination of el niño events and the meridional asymmetry of ENSO. *Journal of Climate*, 25(16):5566–5586.

McGregor, S., Timmermann, A., Stuecker, M., England, M., Merrifield, M., Jin, F.-F., and Chikamoto, Y. (2014b). Recent Walker circulation strengthening and Pacific cooling amplified by Atlantic warming. *Nature Climate Change*, 4(10):888–892.

McPhaden, M. (2002). Mixed layer temperature balance on intraseasonal timescales in the equatorial Pacific Ocean. *Journal of Climate*, 15(18):2632–2647.

McPhaden, M., Zebiak, S., and Glantz, M. (2006). ENSO as an integrating concept in earth science. *Science*, 314(5806):1740–1745.

McPhaden, M. and Zhang, D. (2002). Slowdown of the meridional overturning circulation in the upper Pacific Ocean. *Nature*, 415(6872):603–608.

McPhaden, M. and Zhang, D. (2004). Pacific Ocean circulation rebounds. *Geophysical Research Letters*, 31(18):L18301 1–4.

Meehl, G. and Teng, H. (2007). Multi-model changes in El Niño teleconnections over North America in a future warmer climate. *Climate Dynamics*, 29(7-8):779–790.

Meinen, C. and McPhaden, M. (2000). Observations of warm water volume changes in the equatorial Pacific and their relationship to El Nino and La Nina. *Journal of Climate*, 13(20):3551–3559.

Meinen, C. and McPhaden, M. (2001). Interannual variability in warm water volume transports in the equatorial Pacific during 1993-99. *Journal of Physical Oceanography*, 31(5):1324–1345.

Meinen, C., McPhaden, M., and Johnson, G. (2001). Vertical velocities and transports in the equatorial pacific during 1993-99. *Journal of Physical Oceanography*, 31(11):3230–3248.

Minobe, S. (1997). A 50-70 year climatic oscillation over the North Pacific and North America. *Geophysical Research Letters*, 24(6):683–686.

Montes, I., Colas, F., Capet, X., and Schneider, W. (2010). On the pathways of the equatorial subsurface currents in the eastern equatorial Pacific and their contributions to the Peru-Chile Undercurrent. *Journal of Geophysical Research: Oceans*, 115(9).

Munk, W. (1981). Internal waves and small scale processes. *Evolution of Physical Oceanography, B. A. Warren and C. Wunsch, Eds., MIT Press, 264–291.*

Nakamura, H. and Kazmin, A. (2003). Decadal changes in the North Pacific oceanic frontal zones as revealed in ship and satellite observations. *Journal of Geophysical Research C: Oceans*, 108(3):23–1.

Neske, S. and McGregor, S. (2018). Understanding the Warm Water Volume Precursor of ENSO Events and its Interdecadal Variation. *Geophysical Research Letters*, 45(3):1577–1585.

Newman, M. (2007). Interannual to decadal predictability of tropical and North Pacific sea surface temperatures. *Journal of Climate*, 20(11):2333–2356.

Newman, M. (2013). An empirical benchmark for decadal forecasts of global surface temperature anomalies. *Journal of Climate*, 26(14):5260–5269.

Newman, M., Alexander, M., Ault, T., Cobb, K., Deser, C., Di Lorenzo, E., Mantua, N., Miller, A., Minobe, S., Nakamura, H., Schneider, N., Vimont, D., Phillips, A., Scott, J., and Smith, C. (2016). The Pacific decadal oscillation, revisited. *Journal of Climate*, 29(12):4399–4427.

Newman, M., Shin, S.-I., and Alexander, M. (2011). Natural variation in ENSO flavors. *Geophysical Research Letters*, 38(14).

Nie, X., Gao, S., Wang, F., Chi, J., and Qu, T. (2019). Origins and Pathways of the Pacific Equatorial Undercurrent Identified by a Simulated Adjoint Tracer. *Journal of Geophysical Research: Oceans*, 124(4):2331–2347.

Nonaka, M., Xie, S.-P., and McCreary, J. (2002). Decadal variations in the subtropical cells and equatorial pacific SST. *Geophysical Research Letters*, 29(7):20–1.

Okubo, A. (1971). Oceanic diffusion diagrams. *Deep-Sea Research and Oceanographic Abstracts*, 18(8):789–802.

Parker, D., Folland, C., Scaife, A., Knight, J., Colman, A., Baines, P., and Dong, B. (2007). Decadal to multidecadal variability and the climate change background. *Journal of Geophysical Research Atmospheres*, 112(18).

Pierce, D. (2001). Distinguishing coupled ocean-atmosphere interactions from background noise in the North Pacific. *Progress in Oceanography*, 49(1-4):331–352.

Pierce, D., Barnett, T., and Latif, M. (2000). Connections between the Pacific Ocean Tropics and midlatitudes on decadal timescales. *Journal of Climate*, 13(6):1173–1194.

Power, S., Casey, T., Folland, C., Colman, A., and Mehta, V. (1999). Inter-decadal modulation of the impact of ENSO on Australia. *Climate Dynamics*, 15(5):319–324.

Qiu, B. (2003). Kuroshio extension variability and forcing of the Pacific decadal oscillations: Responses and potential feedback. *Journal of Physical Oceanography*, 33(12):2465–2482.

Reynolds, R., Rayner, N., Smith, T., Stokes, D., and Wang, W. (2002). An improved in situ and satellite sst analysis for climate. *Journal of Climate*, 15(13):1609–1625.

Rodgers, K., Friederichs, P., and Latif, M. (2004). Tropical Pacific decadal variability and its relation to decadal modulations of ENSO. *Journal of Climate*, 17(19):3761–3774.

Ruehs, S., Zhurbas, V., Koszalka, I., Durgadoo, J., and Biastoch, A. (2018). Eddy diffusivity estimates from Lagrangian trajectories simulated with ocean models and surface drifter data-A case study for the greater Agulhas system. *Journal of Physical Oceanography*, 48(1):175–196.

Ruprich-Robert, Y., Msadek, R., Castruccio, F., Yeager, S., Delworth, T., and Danabasoglu, G. (2017). Assessing the climate impacts of the observed atlantic multidecadal variability using the GFDL CM2.1 and NCAR CESM1 global coupled models. *Journal of Climate*, 30(8):2785–2810.

Schneider, N. (2000). A decadal spiciness mode in the tropics. *Geophysical Research Letters*, 27(2):257–260.

Schneider, N. (2004). The response of tropical climate to the equatorial emergence of spiciness anomalies. *Journal of Climate*, 17(5):1083–1095.

Schneider, N. and Cornuelle, B. (2005). The forcing of the Pacific Decadal Oscillation. *Journal of Climate*, 18(21):4355–4373.

Schneider, N., Miller, A., Alexander, M., and Deser, C. (1999a). Subduction of decadal North Pacific temperature anomalies: Observations and dynamics. *Journal of Physical Oceanography*, 29(5):1056–1070.

Schneider, N., Venzke, S., Miller, A., Pierce, D., Barnett, T., Deser, C., and Latif, M. (1999b). Pacific thermocline bridge revisited. *Geophysical Research Letters*, 26(9):1329–1332.

Schott, F., McCreary, J.P., J., and Johnson, G. (2004). Shallow overturning circulations of the tropical-subtropical oceans. *Geophysical Monograph Series*, 147:261–304.

Schott, F., Stramma, L., Wang, W., Giese, B., and Zantopp, R. (2008). Pacific Subtropical Cell variability in the SODA 2.0.2/3 assimilation. *Geophysical Research Letters*, 35(10).

Schott, F., Wang, W., and Stammer, D. (2007). Variability of Pacific subtropical cells in the 50-year ECCO assimilation. *Geophysical Research Letters*, 34(5).

Solomon, A., McCreary Jr., J., Kleeman, R., and Klinger, B. (2003). Interannual and decadal variability in an intermediate coupled model of the Pacific region. *Journal of Climate*, 16(3):383–405.

Spence, P., Griffies, S., England, M., Hogg, A., Saenko, O., and Jourdain, N. (2014). Rapid subsurface warming and circulation changes of Antarctic coastal waters by poleward shifting winds. *Geophysical Research Letters*, 41(13):4601–4610.

Stevenson, S., Baylor, B., Jochum, M., Neale, R., Deser, C., and Meehl, G. (2012). Will there be a significant change to El Niño in the twenty-first century? *Journal of Climate*, 25(6):2129–2145.

Stuecker, M., Timmermann, A., Jin, F.-F., McGregor, S., and Ren, H.-L. (2013). A combination mode of the annual cycle and the El Niño/Southern Oscillation. *Nature Geoscience*, 6(7):540–544.

Thomas, M. and Fedorov, A. (2017). The eastern subtropical pacific origin of the equatorial cold bias in climate models: A Lagrangian perspective. *Journal of Climate*, 30(15):5885–5900.

Vecchi, G. and Wittenberg, A. (2010). El Nino and our future climate: Where do we stand? *Wiley Interdisciplinary Review Climate Change*, 1:260–270.

Vialard, J., Menkes, C., Boulanger, J.-P., Delecluse, P., Guilyardi, E., McPhaden, M., and Madec, G. (2001). A model study of oceanic mechanisms affecting equatorial pacific sea surface temperature during the 1997-98 El Niño. *Journal of Physical Oceanography*, 31(7):1649–1675.

Vimont, D. (2005). The contribution of the interannual ENSO cycle to the spatial pattern of decadal ENSO-like variability. *Journal of Climate*, 18(12):2080–2092.

Widlansky, M., Timmermann, A., McGregor, S., Stuecker, M., and Cai, W. (2014). An Interhemispheric tropical sea level seesaw due to el niño taimasa. *Journal of Climate*, 27(3):1070–1081.

Wijffels, S., Firing, E., and Toole, J. (1995). The mean structure and variability of the Mindanao Current at 8°N. *Journal of Geophysical Research*, 100(C9):18,421–18,435.

Wittenberg, A., Rosati, A., Delworth, T., Vecchi, G., and Zeng, F. (2014). ENSO modulation: Is it decadally predictable? *Journal of Climate*, 27(7):2667–2681.

Xie, S.-P. (1999). A dynamic ocean-atmosphere model of the tropical Atlantic decadal variability. *Journal of Climate*, 12(1):64–70.

Yang, F., Kumar, A., and Wang, W. (2001). Seasonal dependence of surface wind stress variability on sst and precipitation over the tropical pacific. *Geophysical Research Letters*, 28(16):3171–3174.

Yeager, S. and Large, W. (2004). Late-winter generation of spiciness on subducted isopycnals. *Journal of Physical Oceanography*, 34(7):1528–1547.

Yeager, S. and Large, W. (2007). Observational evidence of winter spice injection. *Journal of Physical Oceanography*, 37(12):2895–2919.

Yu, J.-Y. and Kim, S. (2013). Identifying the types of major El Niño events since 1870. *International Journal of Climatology*, 33(8):2105–2112.

Zeller, M., McGregor, S., Capotondi, A., and van Sebille, E. (subm.). Subtropical to tropical pathways of Pacific Ocean spiciness. *Climate Dynamics*.

Zeller, M., McGregor, S., and Spence, P. (2019). Hemispheric asymmetry of the Pacific shallow meridional overturning circulation. *Journal of Geophysical Research: Oceans*.

Zhang, X., Sheng, J., and Shabbar, A. (1998). Modes of interannual and interdecadal variability of Pacific SST. *Journal of Climate*, 11(10):2556–2569.

Zhang, Y., Wallace, J., and Battisti, D. (1997). ENSO-like interdecadal variability: 1900-93. *Journal of Climate*, 10(5):1004–1020.

Zhao, M., Hendon, H., Alves, O., Liu, G., and Wang, G. (2016). Weakened Eastern Pacific El Niño predictability in the early Twenty-First Century. *Journal of Climate*, 29(18):6805–6822.

Zilberman, N., Roemmich, D., and Gille, S. (2013). The mean and the time variability of the shallow meridional overturning circulation in the tropical south pacific ocean. *Journal of Climate*, 26(12):4069–4087.